NUMERICAL MODELLING OF GROUND MOTIONS IN ESKİŞEHİR BASIN

by
Lütfü İhsan Akpunar
B.S., Civil Engineering, Sakarya University, 2016

Submitted to the Kandilli Observatory and
Earthquake Research Institute in
partial fulfillment of
the requirements for the degree of
Master of Science

Graduate Program in Earthquake Engineering
Boğaziçi University
2022

ACKNOWLEDGEMENTS

First of all, I would like to express my sincere gratitude to my supervisor Assoc. Prof. Dr. Gülüm Tanırcan, whose insight and knowledge into the subject matter steered me through this research, for their consistent support, patience and guidance during this research. She continuously provided encouragement and was always willing to assist as much as possible despite the difficulties in life. I am also thankful to Prof. Dr. Oguz Özel and Prof. Dr. Eşref Yalçınkaya for sharing outcomes of the TUBITAK-1001 project and also expressing their thoughts and valuable experiences.

I would also like to thank my family, without whom I would not have been able to continue my education and to complete the master's degree successfully, for unconditional support in my life.

Furthermore, I appreciate the Turkish Petroleum Foundation (TPV) for funding me with scholarships.

And last but not least, I thank to Hilal Yıldız, who has supported me and put up with my stresses in my master's education.

ABSTRACT

NUMERICAL MODELLING OF GROUND MOTIONS IN ESKİŞEHİR BASIN

Eskişehir basin is located at the boundary of central and western Anatolia tectonic regions. Between two active faults it extends in EW direction with two open ends. So far deep velocity structure of the basin has not been well constrained however, average shear wave velocity for the top 30 m and sedimentary thickness estimations are available at various locations of the basin (e.g.,Tün et al. (2016); Yamanaka et al. (2018); Özel et al. (2020)). Number of strong motion recordings is rather limited due low seismicity of the region. The largest magnitude event that has ever been recorded within 150 km is the 2011 Simav Earthquake (Mw 5.9). Eskişehir city, with a population close to a million people, has been expanding towards to this sedimentary basin. Long period ground motion is the concern of large scale structures that will be built at this region. Here we first present observed features of strong ground motions of this event recorded in the Eskişehir basin.

Firstly, we observed that ground motion from the 19.05.2020 Mw 5.9 earthquake is governed by Rayleigh waves at periods longer than 0.5 s. Retrograde motion is visible almost at all basin-recordings. Among recorded waveforms, PGA and PGV of a basin-edge station (#2610 AFAD station) are formed by Rayleigh waves at periods 1 s. The longest significant duration of recordings is as high as 53 sec. Recorded spectral acceleration for 5% damping at spectal periods longer than 1 s is much higher than the one predicted by region specific ground motion prediction models.

In the second phase, we showed formation of an experimental basin geometry utilizing linear interpolation of predominant frequencies at 95 measurement points. Dimensions of the model are 43 km \ 27 km \ 15 km. Basin layer continues across the

entire model in EW direction, but bordered by northern and southern hills to mimic the geographical environment. Maximum depth is about 600 m. In the last phase we investigated the 3D wave propagation of small magnitude events, 17.01.2015 Mw 4.3 and 18.09.2015 Mw 3.7, occurred at northwestern part of the region and center of the basin, and compared with observed recordings for a possible validation of the velocity model. The computer code utilized in simulation relies on a finite difference modelling using staggered grids with nonuniform spacing.

Ground motion simulation of the Mw 4.3 event reveals that the current velocity model overestimates the velocities in the eastern part of the basin in the NS direction, where E-W direction synthetics are generally smaller than the observed ones. On the other hand, synthetic velocities agree with observed ones at basin-center stations in the west. These findings suggest that more careful definitions of basin boundaries are necessary for the future models. Comparison of 1D and 3D simulation results also suggest that a 3D velocity model may produce longer and -more realistic- duration ground motions.

The final step is to perform a blind simulation for the 20 February 1956 Mw 6.5 earthquake. The source was modeled by considering the ambiguities in the source parameters. The previous research was compiled to deal with unknown information about the mechanism and location of this event for consensus. We have compared the simulation outcomes with GMPEs models. The numerical simulation results yielded higher outcomes than estimated spectral ordinates by GMMs.

ÖZET

ESKİŞEHİR HAVZASINDA YER HAREKETİNİN NÜMERİK MODELLENMESİ

Eskişehir havzası orta ve batı Anadolu tektoniği sınırlarında yer almaktadır. İki aktif fayın arasında, iki ucu açık doğu-batı doğrultusunda uzanmaktadır. Şimdiye kadar havzanın hız yapısı ortaya konulmamış ancak, havzanın faklı bölgelerinde ilk 30 m derinlik için ortalama kayma dalgası hızı ve sediman kalınlığı tahminleri mevcuttur. (Örneğin, Tün vd., (2016); Yamanaka vd., (2018); Özel vd., (2020)). Bölgenin düşük deprem aktivitesi nedeniyle kuvvetli yer hareketi kayıtları oldukça kısıtlıdır. Simav depremi Mw 5.9 150 km mesafe içinde kaydedilmiş en büyük büyüklüğe sahip depremdir. Yaklaşık 1 milyon nüfusa sahip Eskişehir kenti bu sedimanter havzaya doğru genişlemektedir. Uzun periyotlu yer hareketi, bu bölgede inşa edilecek büyük ölçekli yapıları ilgilendirmektedir. Öncelikle, Eskişehir'de gözlemlenmiş kuvvetli yer hareketlerinin özellikleri incelendi.

İlk olarak, 19.05.2020 Mw 5.9 büyülüğündeki deprem hareketinin, 0.5 s periyodlarından daha uzun Rayleigh dalgaları tarafından kontrol edildiğini gözlemledik. Ters yönlü (Eliptik) hareket neredeyse tüm basen kayıtçılarında görünmektedir. Kaydedilen dalga formları arasında, bir havza kenarı istasyonunun (2610) PGA ve PGV'si, 1 saniyelik periyotlarda Rayleigh dalgaları tarafından oluşturulmuştur. Kayıtların en uzun significant duration'ı 53 saniye kadar yüksektir. 1 s den daha uzun periyotlardaki %5 sönüm için kaydedilen spektral ivme, bölgeye özgü yer hareketi tahmin modelleri tarafından beklenenden çok daha yüksektir.

İkinci aşamada ise, 95 ölçüm noktalarında hakim frekansın doğrusal interpole edilerek deneysel havza geometrisinin biçimini gösterdik. Modelin boyutları 43 km \ 27 km \ 15 km'dir. Basen tabakası, tüm model boyunca EW yönünde devam ediyor,

ancak coğrafi çevreye uydurmak için kuzey ve güney tepeleri sınırlandırılmıştır. Maksimum derinlik yaklaşık 600 m'dir. Son aşamada, bölgenin kuzeybatı kısmında ve havza merkezinde meydana gelmiş küçük büyüklükteki depreminlerin (17.01.2015 Mw 4.3 and 18.09.2015 Mw 3.7) 3B dalga yayılımını inceledik ve olası hız modelinin doğrulanması için gözlemlenmiş kayıtlarla karşılaştırdık. Simulasyonda kullanılan bilgisayar kodu, düzgün olmayan aralıklı kademeli ızgaralar kullanan sonlu fark modellemesine dayanmaktadır.

Yer hareketi Mw 4.3 simülasyonu, mevcut hız modelinin havzanın doğu kısmındaki kuzey-güney yönündeki hızları olduğundan fazla tahmin ettiğini, burada D-B yönlü sentetiklerin genellikle gözlemlenenlerden daha küçük olduğunu ortaya koymaktadır. Sentetik hızlar ise batıda havzanın merkez istasyonlarında gözlenen hızlarla uyumludur. Bu bulgular, gelecekteki modeller için havza sınırlarının daha dikkatli tanımlanmasının gerekli olduğunu göstermektedir. 1B ve 3B simülasyon sonuçlarının karşılaştırılması, 3B hız modelinin daha uzun ve daha gerçekçi yer hareketi süresini üretebileceğini de göstermektedir.

Son adım olarak, 20 Şubat 1956 Mw 6.5 depremi için tahmini bir simülasyonu gerçekleştirilmiştir. Kaynak, tüm belirsizlikler göz önüne alınarak modellenmiştir. Önceki çalışmalar, depremin fay mekanizması ve lokasyonu hakındaki belirsizlikleri ortadan kaldırmak için derlenmiştir. Simülasyon sonuçlarını, yer hareketi tahmin denklemleri ile karşılaştırdık. Nümerik simülasyon sonuçları, GMM'ler tarafından tahmin edilen spektral deperlerden daha yüksek sonuçlar vermiştir.

TABLE OF CONTENTS

LIST OF FIGURES

LIST OF TABLES

LIST OF SYMBOLS

V_S	S-wave velocity
V_P	P-wave velocity
V_{S30}	Shear wave velocities at 30 m below the top of the soil layer
Q	Quality factor
b	Buoyancy
u	Displacement
v	Velocity
$obs(t)$	Observed ground motion
$syn(t)$	Synthetic ground motion
f	Body force
f_{max}	Maximum frequency
Δt	Time step
ρ	Density
τ	Shear stress
ν,λ	Lame' coefficients
∂	Differential operator

LIST OF ACRONYMS/ABBREVIATIONS

2D	Two dimensional
3D	Three dimensional
AFAD	The disaster and emergency management presidency
CAV	Cumulative absolute velocity
Ds	Significant duration
EFZ	Eskişehir fault zone
EW	East west direction
GCMT	Global centroid moment tensor project
GDT	Group delay time
GMIM	Ground motion intensity measure
GMM	Ground motion model
GMPEs	Ground motion prediction equations
HVSR	Horizontal to vertical spectral ratio
I_A	Arias intensity
ISC	International seismological center
KOERI	Kandilli observatory and research institute
MAM	Microtremor array method
MASW	Multichannel analysis of surface waves
NS	North south direction
NW-SE	North west-south east
PGA	The peak ground acceleration
PGV	The peak ground velocity
PSA	Pseudo spectral acceleration
SHIP	Seismic investigation in Puget Sound
SPAC	Spatial autocorrelation method
TUBITAK	The scientific and technological research council of Turkey

1. INTRODUCTION

Urbanization in valleys exposes a significantly high seismic risk in earthquake-prone regions. Extensive structural damage in Mexico City during the 1985 Michoacan earthquake and in San Francisco during the 1989 Loma Prieta earthquake are just two past examples portraying how disastrous deep sedimentary basins can be on structures and human beings. It has been well known that sedimentary basins amplify ground motion waves at long periods and extend the duration of the earthquakes. The repetitive loading may bring about heavy damage to high-rise buildings or structures with a long predominant period because of long-period seismic motion with a long duration originating from the deep basin structure.

Numerical simulations including the effects of 2- and/or 3-Dimensional underground structure on seismic wave propagation are very helpful to portray the expected long period ground motion of the region. These effects cannot be fully predicted with Ground Motion Prediction Equations (GMPEs) developed for other regions. In order to achieve this goal, a detailed substructure model is essential to accurately model the ground motion. Geological and geophysical information and measurements play an important role in determining the substructure models. The most effective method to determine the accuracy of velocity and geometry of sediment-filled basins is to compare synthetic and recorded ground motion with simulations. Such simulations are particularly important in terms of producing representative earthquake recordings for regions where earthquake hazard is high but seismic activity is low. Eskisehir city in Turkey, which is the case study of this thesis, is a specific example to these regions. The city is the home to nearly 1 million people and location for many long period structures due to rapid urbanization. The city is located at the boundary of central and western Anatolia tectonic regions. Between two active faults Eskişehir Basin extends in EW direction with two open ends. The city has been expanding towards this sedimentary basin. So far deep velocity structure of the basin has not been well constrained however, average shallow subsurface velocity structure and basing depth estimations are available at various locations. (Tün et al., 2016; Yamanaka et al., 2018; Özel et al., 2020). The number of strong motion recordings is rather limited due low seismicity of the region. The largest magnitude event that has ever been recorded within 150 km is the 2011 Simav Earthquake (Mw 5.9). The earthquake of February 20, 1956 (Ms6.4) was the largest event in the city's vicinity in the instrumental period between 1900 and 2022. The city is under threat of earthquakes that will be sourced from the North Anatolian Fault Zone. Eskisehir suffered from the 1999 Mw 7.4 Kocaeli earthquake even though the epicenter is more than 100 km away from the city (Özmen, 2000). In this thesis study, recorded ground motions in the Eskişehir region have been investigated to seek the signature of the effects of long-period earthquake motion. Then, geophysical information at the region has been gathered, basin geometry has been determined with this available information. Then appropriateness of the geometry and velocity structure have been tested by simulating small magnitude events in the region.

Scope of the thesis:

- Investigation of observed features of strong ground motions of the 2011 Simav Earthquake (Mw 5.9) recorded in the Eskişehir basin.
- Construction of a basin geometry with available geophysical measurements.
- Long period simulation of the small magnitude local events utilizing a) a generic 1-D horizontal velocity structure and b) horizontal velocity structure with basin added on top.
- Long Period Simulation of the historical 20.02.1956 Eskisehir Earthquake Mw 6.5.

This study is the first step toward the hybrid frequency simulation of the ground motion at this region. Here it is not intended to refine the basin model, instead, to test the adequacy of the initial basin model calculated with the available data.

2. LITERATURE SURVEY

It has been well known that sedimentary basins amplify ground motion at long periods and extend the duration of the earthquakes. The repetitive loading may bring about heavy damage to high-rise buildings or buildings with a long predominant period because of long-period seismic motion with a long duration originating from the deep basin structure. The effects of basin structure on seismic waves are the subject of abundant research particularly after the 1964 Niigata earthquake (M 7.5) and the 1983 Central Japan Sea earthquake (M 7.7), since prolonged and long-period surface waves caused extensive damage to large oil tanks, followed by fires (Kudo and Sakaue (1984)).

Hatayama et al. (1995) showed that the Osaka basin in Japan, which is filled with soft sediments, forms long-period Love waves. Similarly, in the 2003 Tokachi-Oki earthquake, large oil tanks in the city of Tomakomai were heavily damaged despite being 250 km away from the epicenter (Hatayama et al. (1995); Koketsu et al. (2005); Koketsu and Miyake (2008)).

Earthquakes may cause severely environmental damage despite the long distance. For instance, during the 1985 Michoacan (Mw 8.1) Mexico earthquake, surface waves lasted as long as 10 minutes and had a long period of 2-3 seconds, although the epicenter was 400 km away. The event caused the death of 20,000 people (Anderson et al., 1986).

Pitarka et al. (2004) have also qualified the accuracy of the 3D velocity model of the Puget Sound region using 28 February 2001 Nisqually earthquake M 6.8 by the goodness of fit factor proposed by Arben Pitarka. This 3D velocity structure model relies on the geophysical exploration acquired from other studies and Seismic Investigation in Puget Sound (SHIPS). For this purpose, forty stations were available to compare synthetics and observed data. They found that the deep basin structure has a major effect on the propagation of seismic waves with long periods, especially those greater than 3 seconds.

Hartzell et al. (2006) investigated strong ground motions in Santa Clara Valley, California by utilizing the 3-dimensional velocity structure of the basin. They partially validated the velocity structure through the simulation of small magnitude local events and the 1989 M7.1 Loma Prieta earthquake.

Long period ground motion simulations with 3-D velocity structure have also been performed in various settlements in Turkey. Among them Goto and Sawada (2004) compared the synthetic and recorded strong motions of the 1999 Kocaeli Earthquake in order to validate the three-dimensional basin model of Adapazarı. Tanircan (2012) integrated the three-dimensional numerical velocity model of the Eastern Marmara Region into the finite difference simulation technique. Success of the velocity model for the Istanbul region was investigated with strong motion recordings in Istanbul. The shallow portion of the velocity model was modified with the available surface velocity structure information, and low frequency ground motions were calculated.

Moreover, there are many other studies stressing out the behavior of the basin models. For instance, Iyisan and Khanbabazadeh (2013) show that the inclination angle of shallow basin edges has great effects on soil amplification. They suggested that the spectral amplification of the low-sloped bedrock was relatively higher than the high-inclined bedrock at the basin edges. Although the results of the analysis showed that the maximum magnification is in short periods, the period of maximum magnification becomes longer as you move away from the basin edges.

Maufroy et al. (2015) performed numerical simulations of 3-D Mygdonian basin in Greece with 6 different methods including the one (Pitarka, 1999) utilized in this Master of Science thesis. They compared synthetic versus observed waveforms through the adopted goodness of fit factor. The results were discussed considering the differences between the numerical methods.

Pitarka et al. (2015) investigated the amplitudes of long-period surface waves that will affect critical buildings with 2-10 s resonance periods in the Arabian Gulf. Their simulation confirmed that shallow earthquakes and sedimentary basin geometry are responsible for large amplitude and long-duration surface waves.

In a parametric study for Duzce, Turkey (Hasal et al., 2018) 2-D and 1D dynamic analyses of the basin were modeled. Differences between spectral acceleration values obtained by 1D and 2D modeling were portrayed and a predictive equation was suggested between the spectral acceleration ratios (aggravation factor) and basin edge geometry.

During the 2020 Samos earthquake (Mw 7), structures in the city of Izmir, approximately 70 km away from the epicenter, were severely damaged. Unexpectedly high spectral accelerations between 0.5-1.5 s spectral periods are attributed to the 1-D local resonance together with locally generated surface waves due to Bayraklı-Bornova basin/basin edge structures (Makra et al., 2021; Gülerce et al., 2022).

Di Michele et al. (2022) simulate the 2009 April 6 L'Aquila earthquake with predicted source parameters. They have succeeded in the agreement between the simulations and recordings. They also suggested that this can be applied to the past and future events to make the deduction for seismic risk assessment.

One of the leading causes of long-period motion is surface waves generated by the basin, Rayleigh, and Love waves. Another reason for generating long-period motion is that the seismic motion with a long period diminishes more slowly with distance. Not only attenuation of the low-frequency more slowly with distance, but also surface waves triggered by the basin have induced long-period ground motion with long duration. Apart from these, the motion's frequency content is associated with the earthquake's magnitude. Meza-Fajardo et al. (2021) attributed the dominant frequency to source characteristics and propagation paths. They have also mentioned that the 2011 Tohoku megathrust earthquake, Mw 9.0, dominates the frequency below 0.1 Hz, but the small earthquakes, Chuetsu and Chuetsu, Oki, are in the frequency range of 0.1-0.2 Hz.

There are many similar studies aimed at understanding the behavior of earthquake ground motion in sediment-filled basins. The high-performance parallel computer made the 3-D physics-based simulation possible. Furthermore, the researchers model that future seismic events most likely occur. Even if there is unknown information about this event, they attempt to forecast motion by considering more realistic scenarios. This type of simulation is referred to as blind prediction.

3. A CASE STUDY OF ESKİŞEHİR REGION

3.1. Tectonics

Eskişehir Fault Zone (EFZ), extending from İnegöl to Cihanbeyli, is one of the primary neo-tectonic structures of NW Turkey (Ocakoğlu, 2007). It is located at the boundary of central and western Anatolia tectonic regions (Barka et al. (1997); Koçyiğit and Özacar (2003)). According to the Active Fault Map of Turkey (Emre et al., 2018), four fault segments (#140) as seen in Figure 3.1 are considered as Eskişehir Fault. The segments extend in an approximately NW-SE direction. Dominant motion is a right-lateral strike-slip with a normal dip-slip component. The northern border is drawn with the left lateral strike-slip Taycılar Fault (#144). Both faults can produce Mw 6.5-6.7 earthquakes (Emre et al., 2018). Between Eskişehir and Taycılar faults, Eskişehir basin extends with two open ends. So far the velocity structure of the basin is not well constrained. However, V_{S30} estimations and sedimentary thickness estimates are available at various locations of the basin (Tün et al., 2016; Yamanaka et al., 2018; Özel et al., 2020). Even though EFZ is regarded as a secondary structure (substructure) or internal fault zone, it plays a prominent role in the internal deformation of the Anatolian plate. The observation of EFZ seismic activities is essential for assessing the seismic hazard in the vicinity of Eskişehir.

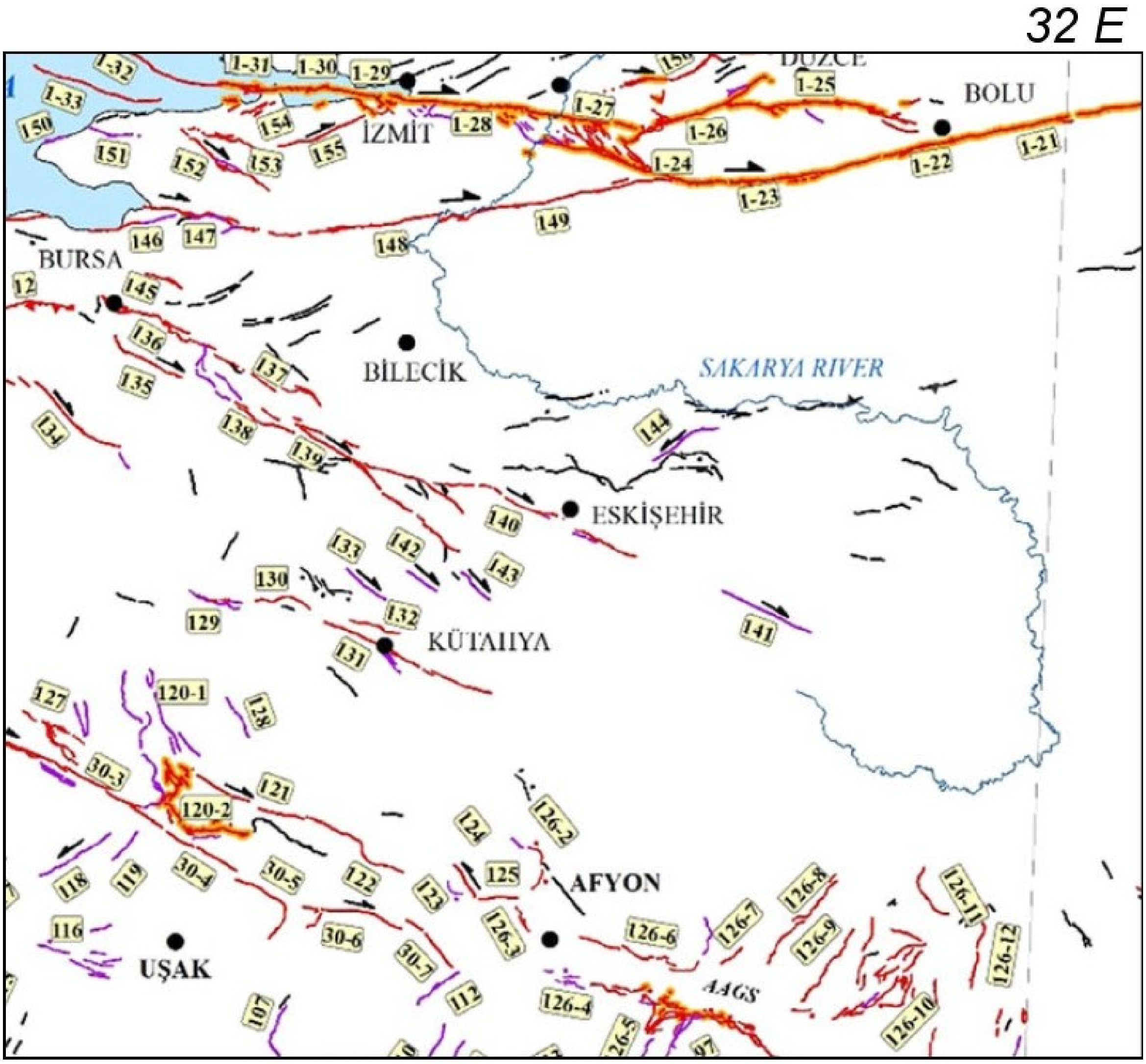

Figure 3.1. Active faults at the vicinity of Eskişehir (adopted from Emre et al., 2018.)

3.2. Seismicity

Eskişehir is situated in northwest Turkey. This city is threatened by seismic activities of the North Anatolian fault zone, Eskişehir fault zone, and Kutahya fault zone (Şaroğlu et al., 1987). Among these fault zones, EFZ is crucial in evaluating the seismic hazard of Eskişehir.

The number of earthquakes with Mw $\geq$ 3.5 in Eskişehir between 1900 and 2022 is more than 40. The distribution of the earthquakes larger than Mw 3.5 occurred in the vicinity of the city during an instrumental period between 1900-2022 is shown in

Figure 3.2. The depth of those events is less than to 20 km. The seismogenic thickness of the Eskişehir Fault Zone is reported as 16-18 km (Emre et al., 2018). Hence all events can be considered as shallow crustal earthquakes.

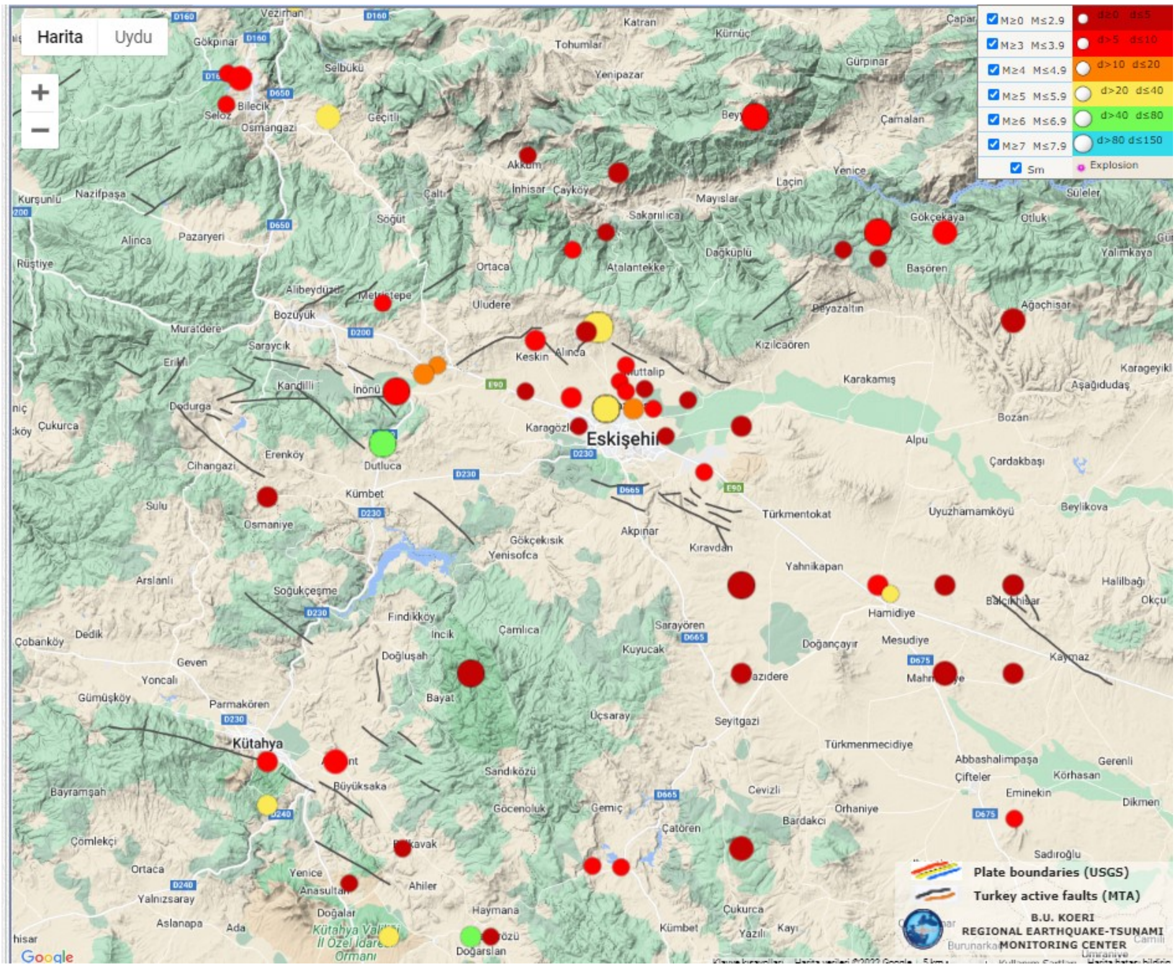

Figure 3.2. Illustration of the seismic events greater than Mw ≥ 3.5 that occurred between 1900 and 2022 in Turkey (from http://www.koeri.boun.edu.tr).

Eskişehir is subjected to a considerable seismic hazard due to the Eskişehir fault zone. Probabilistic seismic hazard maps of Turkey (https://www.turkiye.gov.tr/afad-turkiye-deprem-tehlike-haritalari) in terms of Peak Ground Acceleration (PGA) at the design basis level (return period of 475 years) show as high as 0.3 g in this region. The earthquake of February 20, 1956 (Ms 6.4) along the EFZ was the largest event in the city's vicinity in the instrumental period between 1900 and 2022. The researchers have controversial issues with the location and the source mechanism of this seismic event.

Canıtez and Üçer (1967) proposed that the earthquake had a right-lateral strike-slip mechanism with a normal component.

On the other hand, McKenzie (1972) indicated that the focal mechanism of this seismic event is the normal faulting with a slight right-lateral component. The latest study on the event was performed by Seyitoğlu et al. (2015). They found the epicenter of the event between the Çukurhisar and Sultandere regions, and their geological and seismological findings support focal mechanism solutions proposed by Canıtez and Üçer (1967). The maximum intensity of this event is VIII at the epicentral area (Öcal, 1959). It caused heavy to medium damage to nearly 3000 buildings (Öcal, 1959). The majority of the damage concentrated on the NW of Eskişehir, very close to Çukurhisar village. Stochastic finite fault simulation of the Ms 6.4 Eskişehir event by Tanircan et al. (2020) indicated that the largest estimated PGA on the surface projection of the fault plane (R_{jb}=0 km) is as high as 0.36 g, whereas Spectral acceleration at 0.2 s and 1 s (SA02 and SA1) are 1.0 g and 0.27 g respectively.

3.3. Geophysical Investigation on Eskişehir Basin

There have been extensive geophysical investigations in the Eskişehir region. Among them, Tün et al. (2016) conducted single station microtremor measurements at 318 points in Figure 3.3, array measurements of microtremor at nine locations in Table 3.1 and seismic reflection at six sites inside the Eskişehir basin. They found that bedrock depth is close to 1 km in the northeastern part of the basin. The average shear wave velocity is 1300 m/s down to bedrock. Microtremor array measurement (MAM) Points obtained from (Tün et al., 2016), as shown in Table 3.1.

Table 3.1. Microtremor array measurement points (obtained from Tün et al. (2016)).

No	**Data**	**Lat.**	**Long.**	**Elev. (m)**	**Geology**	**AV$_{S30}$ (m/s)**	**NEHRP site class**	**Ave. Ampl. (0.2-10 Hz)**	**f$_r$ (Hz)**
1	MAM* SPAC*02	39.81725	30.4245	823	New Alluvium	261	D	5.0	0.67
2	MAM SPAC03	39.79755	30.4395	813	New Alluvium	354	D	5.8	0.38
3	MAM SPAC04	39.7685	30.4635	793	New Alluvium	353	D	6.0	1.20
4	MAM SPAC06	39.82032	30.5284	787	New Alluvium	135	E	7.1	0.46
5	MAM SPAC07	39.78832	30.504	796	New Alluvium	250	D	3.7	0.54
6	MAM SPAC09	39.83773	30.5684	785	New Alluvium	204	D	4.8	0.47
7	MAM SPAC11	39.77945	30.5476	787	New Alluvium	175	E	8.9	0.87
8	MAM SPAC12	39.75474	30.5805	792	New Alluvium	311	D	4.1	1.25
9	MAM SPAC13	39.80706	30.6307	781	New Alluvium	203	D	5.9	0.38

∗Microtremor Array Method (MAM),∗ Spatial Autocorrelation Method (SPAC)

They have also evaluated the relationships between the bedrock depth and the fundamental frequency using the Horizontal to Vertical Spectral Ratio (HVSR) method proposed by Nakamura (1989). To construct the Eskişehir basin structure, a total number of 318 single-station microtremor measurements have been carried out. Moreover, they have determined the sediment thickness by utilizing MAM data (nine sites), borehole data (three sites), reflection surveys (eight sites) as well as shallow drilling data (10 sites) in Figure 3.4. The equation 3.1 which is given below, reflects the bedrock-depth relationship.

$$h = 136 f_r^{-1.36} \tag{3.1}$$

where, h is the bedrock depth (m) and f_r is the predominant frequency (Hz).

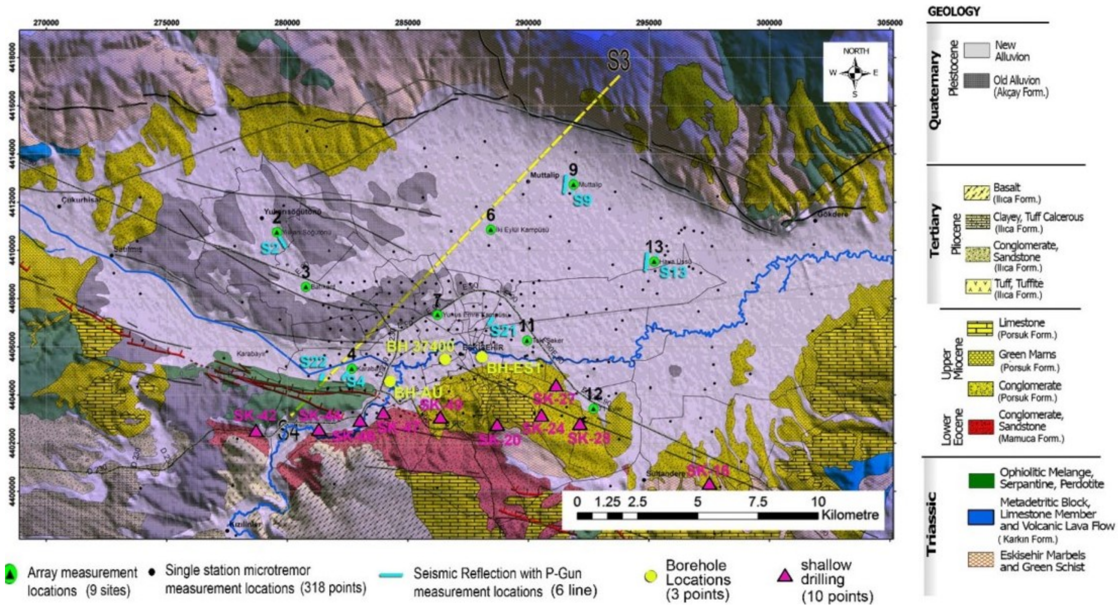

Figure 3.3. Illustration of the investigated sites, microtremor array measurement, borehole, seismic reflection and shallow drilling sites on geological map (obtained from Tün et al., 2016).

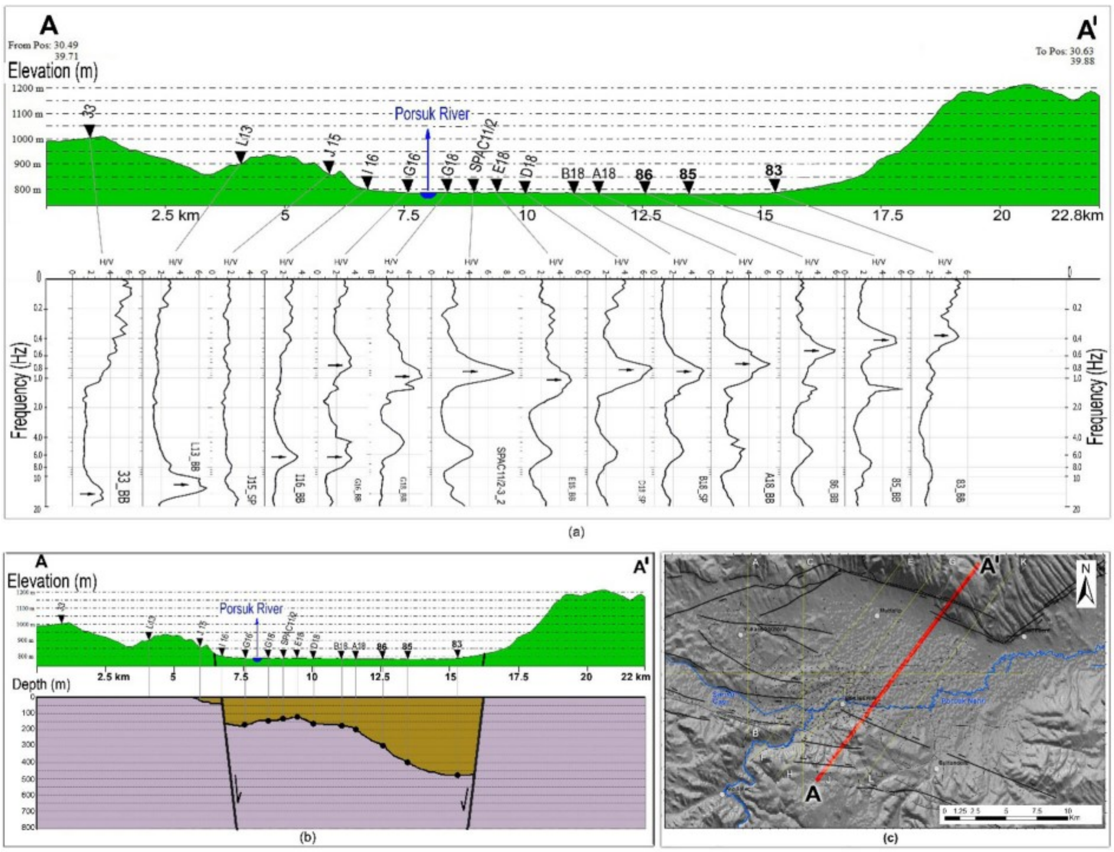

Figure 3.4. The cross-section of A-A' profile using depth-resonance frequency relationships at the Eskişehir basin (obtained from Tün et al., 2016).

Yamanaka et al. (2018) carried out the 1D S-wave velocity profile of shallow and deep soil layers beneath the seismic stations in Eskişehir Province, Turkey. For this purpose, microtremor array explorations were performed at eight AFAD stations (2601, 2602, 2603, 2604, 2606, 2607, 2608, and 2609) to construct the 1D S-wave velocity structure model. They found that stations in the basin are of low-velocity layers. In the center of the basin, an S waves velocity of 2 km/s corresponds to a depth of 1 km. On the other hand, it accounts for a depth of 0.3 km at the edge of the basin.

Additionally, they examined the effects of the shallow and deep layers on the amplification factors at 15 seismic stations. They found that shallow soil layers amplify strong ground motion at higher than 3 Hz (e.g.,2602 and 2613 AFAD stations), whereas the deep soil layers are responsible for the amplification lower than 1 Hz (e.g.,2614 and 2616 AFAD stations). They also implemented the Intrinsic Attenuation study for the region by inverting site amplification factors from S-waves in recording to Q-values of the sediments and S-waves velocities. Q-values for deep and shallow sedimentary layers are given in Equation 3.2 (Yamanaka et al., 2018).

$$\begin{aligned} Q^{\text{shallow}} &= (3.9 \pm 3.5) f^{0.88 \pm 0.33} f_0 = 11.7 \pm 4.2 \quad V_s \leq 700 \text{ m/s} \\ Q^{\text{deep}} &= (137 \pm 85.6) f^{0.88 \pm 0.27} f_0 = 14.0 \pm 4.5 \quad V_s > 700 \text{ m/s} \end{aligned} \tag{3.2}$$

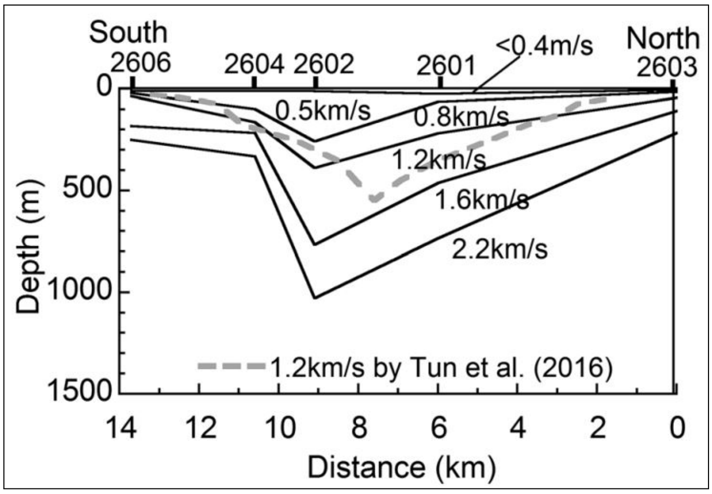

Figure 3.5. Cross-section of S-waves velocity structure in the north-south direction. The dashed line shows the S- waves velocity of 1.2 km/s in accordance with the depth by Tün et al. (2016) (obtained from Yamanaka et al., 2018).

Within the scope of the Scientific and Technological Research Council of Turkey (TUBITAK) Project-116Y524 'Investigation of Modeling of Geological Structures for Prediction of Strong Ground Motion Caused by Crustal Earthquakes' (hereafter TUBITAK-116Y524 by Özel et al. (2020)), the site characteristics are investigated through the single station and array microtremor measurements, spatial auto-correlation Method (SPAC), multichannel analysis of surface waves (MASW), interferometry, micro-gravity, and Receiver Function Methods. S-wave shallow velocity structures are obtained. The predominant frequency of sites inside the basin varies between 0.3-0.6 Hz. The sediment thickness reaches to the maximum value (600 m) along 5 NS trending profiles. V_{S30} distributions were used in high-frequency strong motion simulations.

Single station and array microtremor measurements were conducted at 88 points in 5 NS trending 5 lines in Figure 3.6. The distances between the lines change from 6 to 9 km. The space among the points is almost 200 m. The fundamental frequencies of the sites were attained by means of the HVSR.

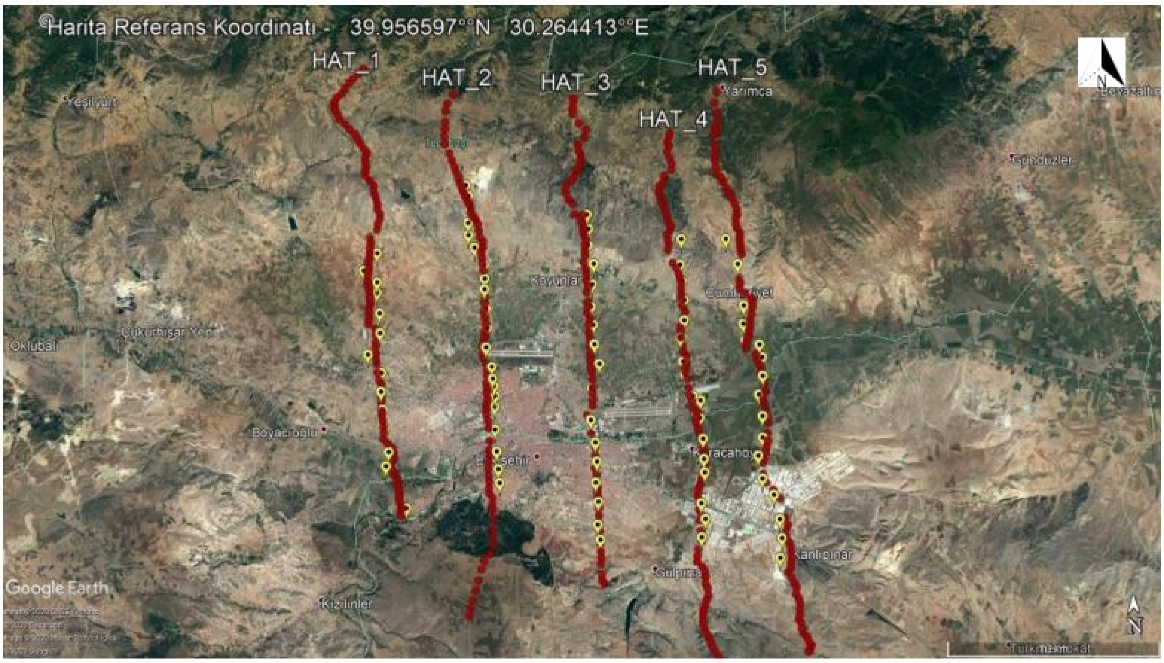

Figure 3.6. The location of the microtremor array measurements (5 lines) towards the north-south direction. The yellow signs display microtremor array measurements, the red symbols show gravity measurements (obtained from TUBITAK Project-116Y524 by Özel et al, 2020).

In TUBITAK-116Y524 project, a relationship between the bedrock depth and predominant frequency by Özalaybey et al. (2011) was utilized to establish the geometry of the basin at the NS boundary of the basin fundamental frequencies are above 1 Hz while it is as low as 0.3 Hz at the center of the basin. The low predominant frequency means the thick bedrock depth. Thus, the resonance frequency of 0.3 Hz roughly corresponds to sediment thickness of 651 m by using Özalaybey et al. (2011) relationships.

Single station microtremor measurements were implemented in the seismic stations (2601, 2602, 2604, 2606, 2610, 2613, and 2614). Those stations at Eskişehir basin were employed in 2017 and governed by The Disaster and Emergency Management Presidency (AFAD) and Anadolu University. In addition to these, 8 sites had been investigated in terms of microtremor exploration (e.g. Muttalip, Durusilya, Çukurhisar, Uludere,Alınca, Keskin, Kavacık and Hasanbeyli).

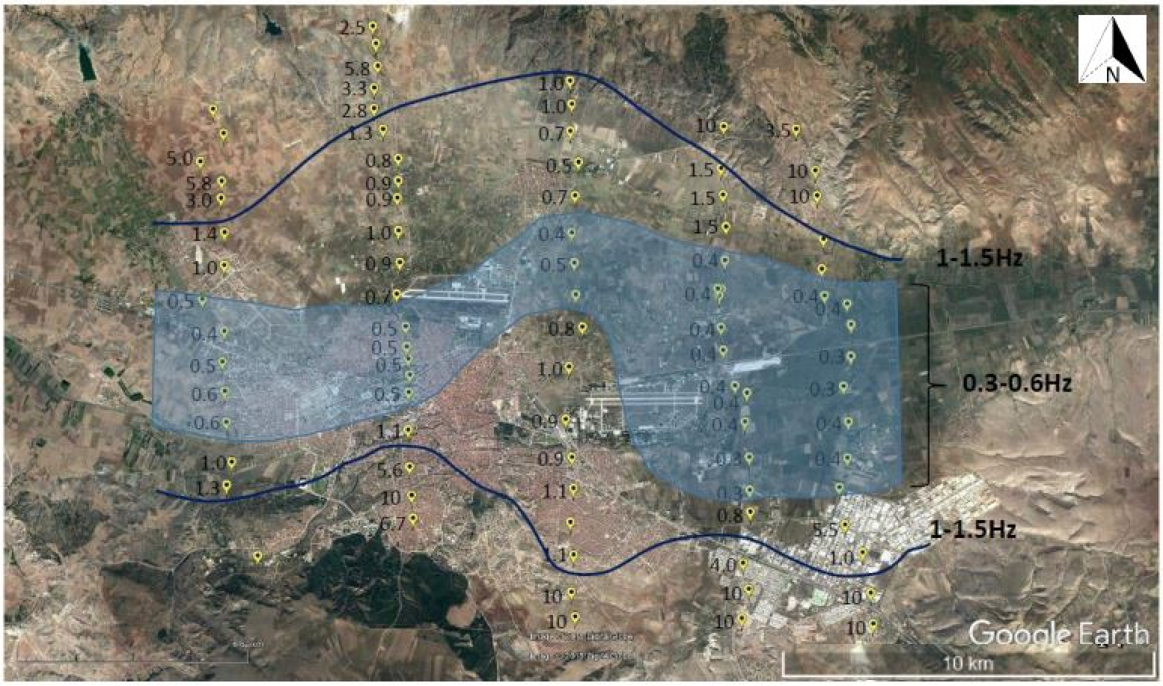

Figure 3.7. The distribution of resonance frequency on the Eskişehir basin. Shaded field indicate the frequency range of 0.3 to 0.6 Hz. The Blue line display the frequency range of 1 to 1.5 Hz (obtained from TUBITAK Project-116Y524).

3.4. Construction of Velocity Structure Model for Eskişehir Basin

Geophysical information and geotechnical exploration play a crucial role in modeling velocity structure. The basin structure has been better understood with the help of the geophysical experiments, which are conducted within the scope of the TUBITAK-116Y524 Project and other surveys in the region.

In this study, in order to construct the basin geometry, MAM results at 77 points, single station MAM results at nine sites from TUBITAK-116Y524, and MAM SPAC results at nine sites from Tün et al. (2016) are utilized. The total number of MAM points is 95.

The boundaries of the studied field extend from latitudes of 39.66°N to 39.92°N and longitudes of 30.30°E to 30.80°E to cover the whole area, including the epicenter of the earthquakes. The coordinate of the origin point was considered as latitude 39.66°N, longitude 30.30°E. The plan of the MAM and Single station MAM were relatively plotted in MATLAB by converting the geographic coordinate to Cartesian coordinates (3D) (MATLAB, 2021). Additionally, the first and fifth lines were extended to the west and east boundaries, respectively. We assume the thickness of the first and fifth sedimentary layers is similar to that of the west and east boundaries.

Our velocity model has covered a volume of 43 km \ 27 km \ 15 km, X, Y, and Z respectively. The sedimentary thickness of bedrock depth was determined via the aforementioned relationship published by Tün et al. (2016). Thus, the 3D view of the basin bedrock was created by interpolating all single stations and MAMs with their depths by MATLAB (2021). In addition, a cross-section of five lines was created, where MAMs are performed densely from south to north. 3D basin structure and cross-section of lines are shown in Figures 3.9-3.15. The profiles have an increasing trend towards the east part in depth to the basin basement. The maximum depth to the basement attains about 700 m in the fifth line, which is the eastmost line. Besides, the maximum sedimentary layer depths in a north-south direction can be encountered in the basin's center.

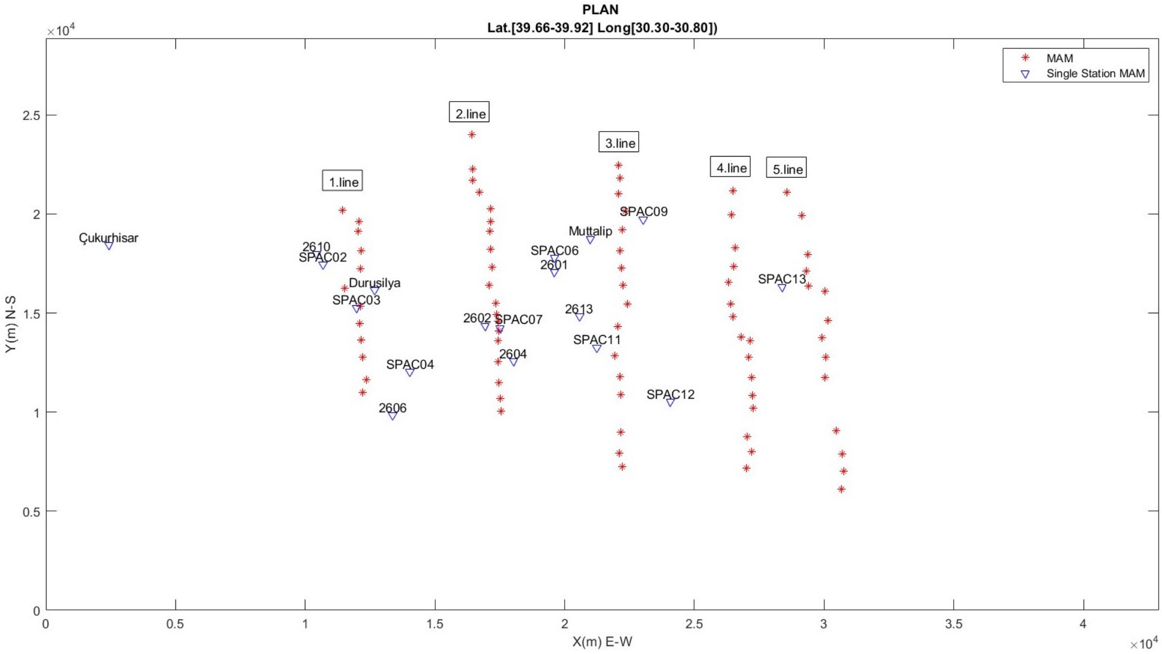

Figure 3.8. Top of view of the MAM and single stations.

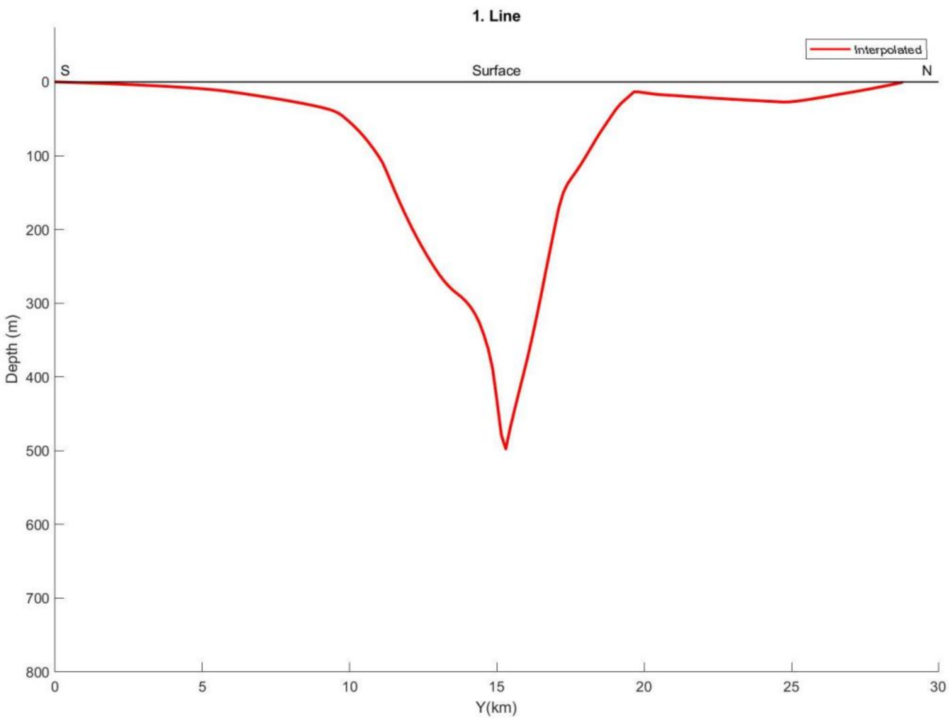

Figure 3.9. Cross-section of 1. line via interpolated data.

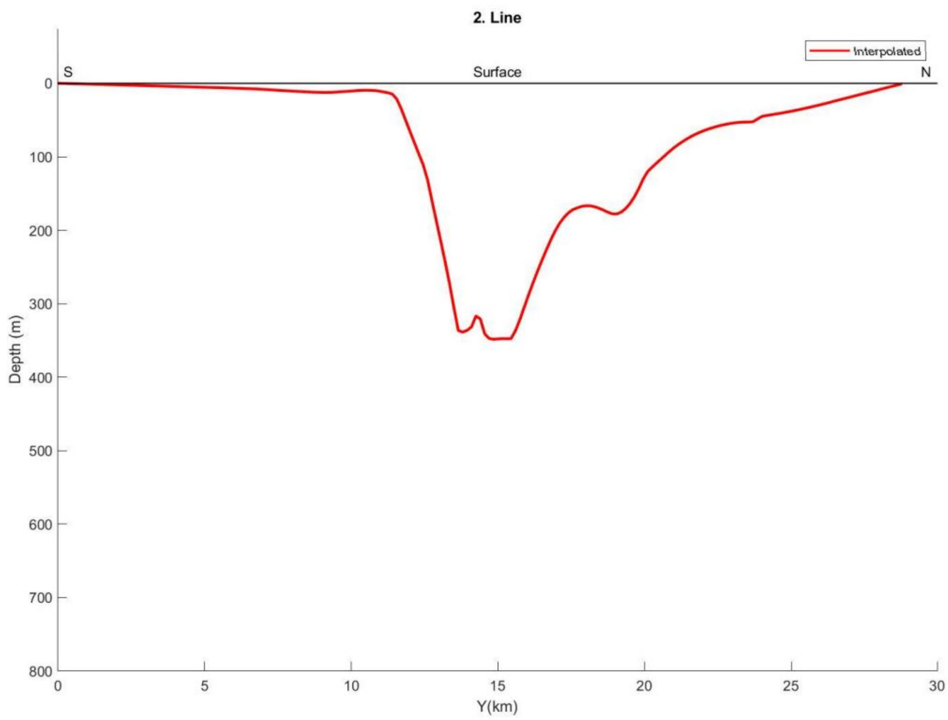

Figure 3.10. Cross-section of 2. line via interpolated data.

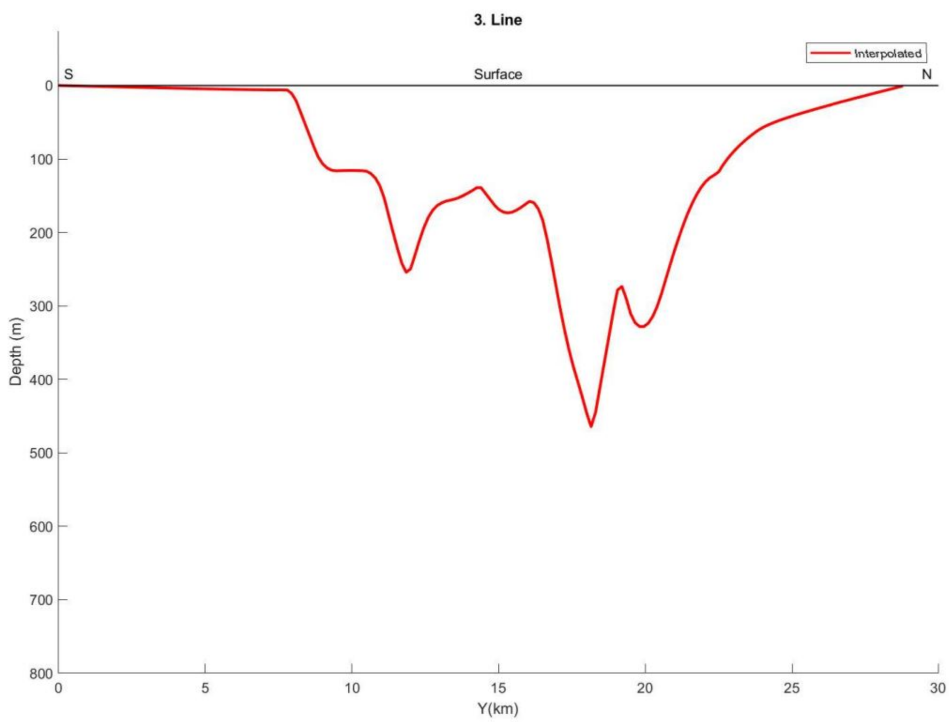

Figure 3.11. Cross-section of 3. line via interpolated data.

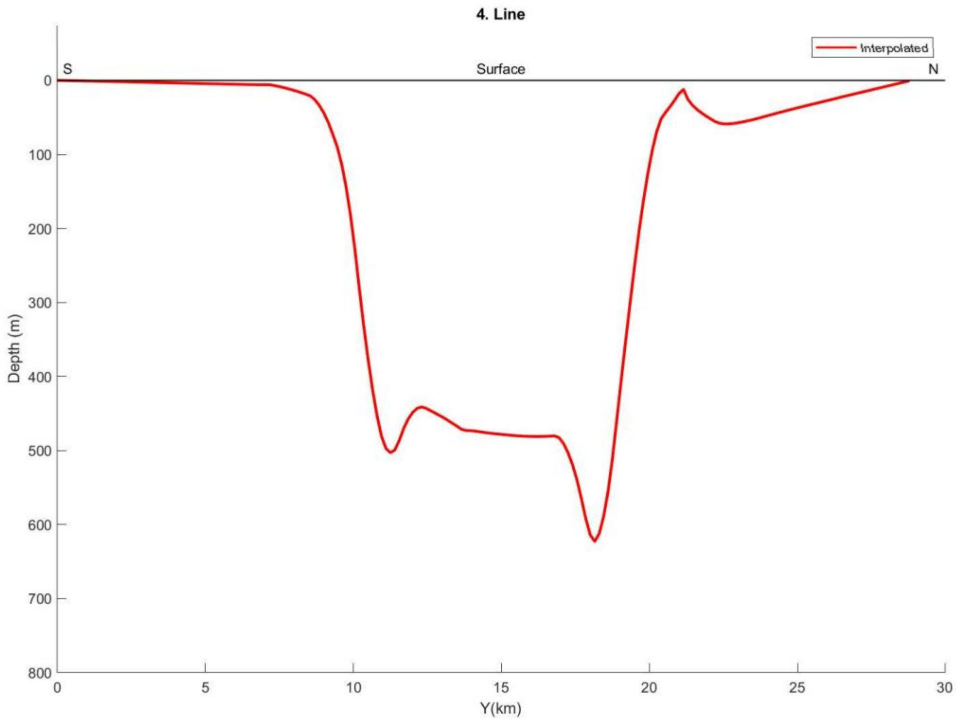

Figure 3.12. Cross-section of 4. line via interpolated data.

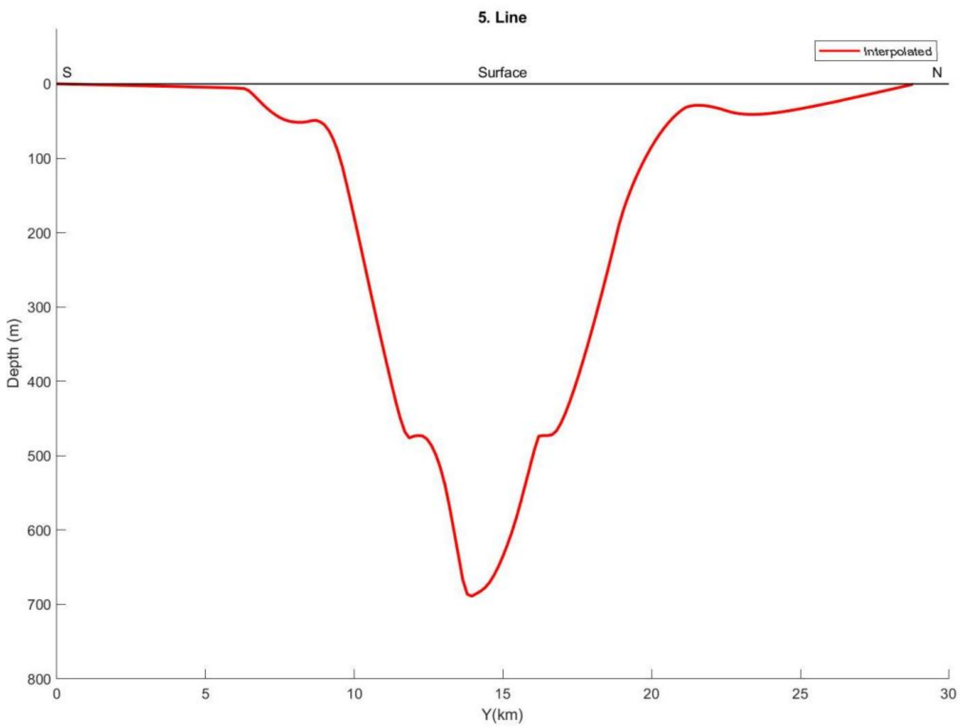

Figure 3.13. Cross-section of 5. line via interpolated data.

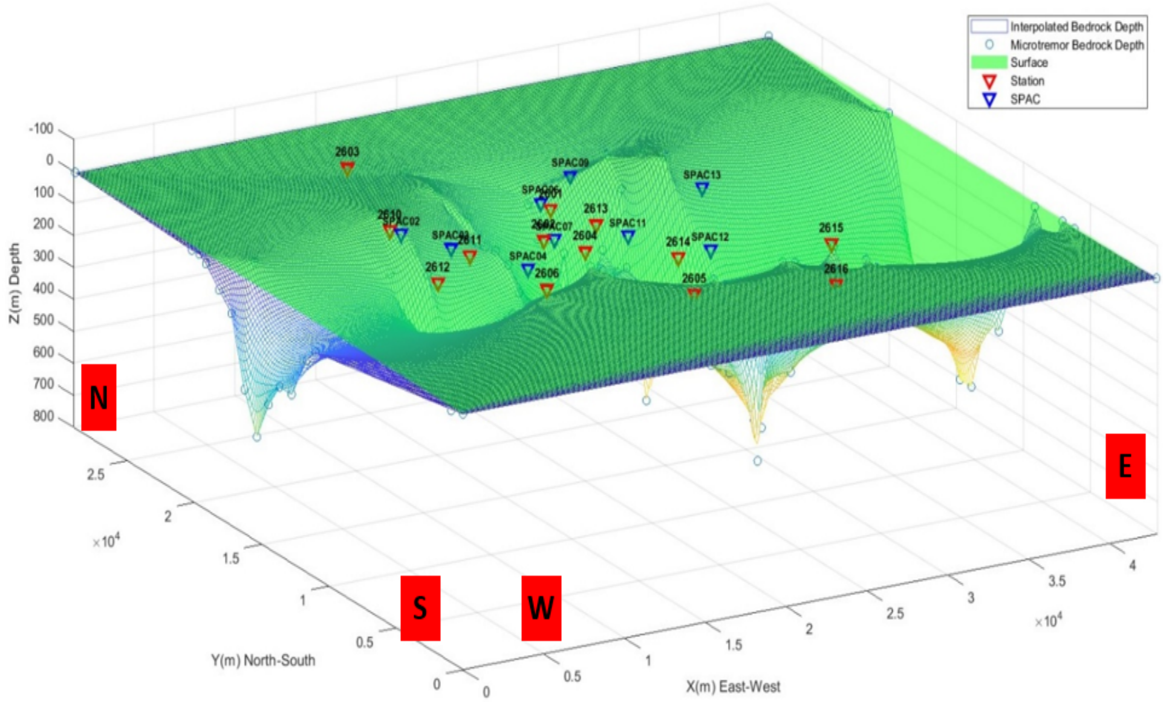

Figure 3.14. 3D appearance of the basin from west to east.

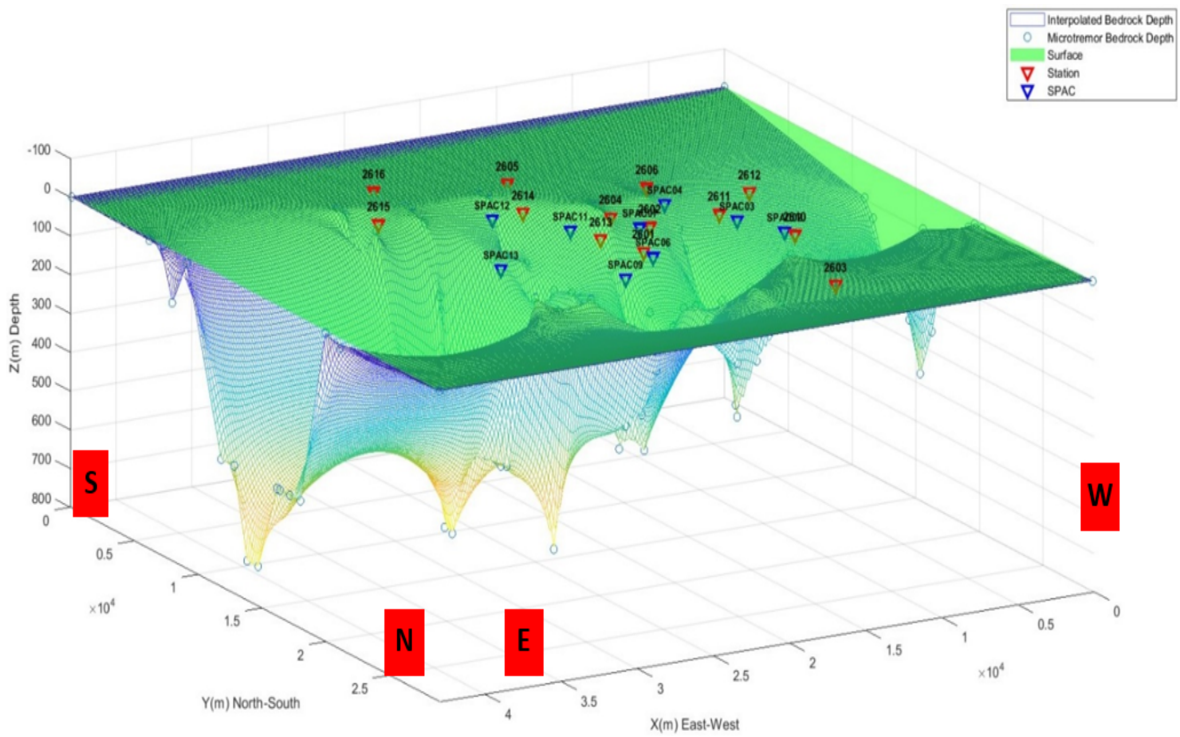

Figure 3.15. 3D appearance of the basin from east to west.

Other parameters to construct velocity structure are S-wave velocity (Vs), P-wave velocity (Vp), and density (ρ) used in our model acquired from Mindevalli and Mitchell (1989). Mindevalli and Mitchell (1989) evaluated Turkey's velocity structure for two regions using seismic surface waves. A one-dimensional crustal velocity structure model for Turkey suggested by Mindevalli and Mitchell (1989) was adopted. Mindevalli and Mitchell velocity model parameters are described in Table 3.2.

Table 3.2. Model Parameters of the underground structure (model based on Mindevalli and Mitchell (1989)).

Depth (m)	**V$_P$ (m/s)**	**V$_S$ (m/s)**	**Density (kg/m^3)**	**Q$_P$**	**Q$_S$**
0	4690	2710	2430	200	100
1000	4780	2760	2450	200	100
2000	4940	2850	2490	400	200
3000	5150	2970	2530	400	200
4000	5380	3110	2580	500	250
5000	5640	3250	2630	500	250
7000	5870	3390	2670	600	300
9000	6060	3500	2720	600	300
11000	6170	3560	2750	800	400
13000	6230	3600	2770	800	400
15000	6250	3610	2780	800	400
20000	6330	3650	2800	800	400
25000	6550	3780	2860	800	400
30000	6860	3960	2940	1000	500
35000	7200	4150	3040	1000	500

Another parameter utilized in the velocity model is the anelastic attenuation, referred to as the quality factor (Q). Two factors have led to the attenuation of seismic waves; dispersion and dissipation or absorption. The dissipation or absorption effect stems from the different attenuations of frequency content; the high-frequency content is more decayed than low frequecy. Dispersion arises from a wave with a high frequency travels faster than a wave with a low frequency. It is usually also regarded as independent frequency, increasing with density and depth. The high value of Q means small attenuation and vice versa. The Graves method by (Graves, 1996) is used in the finite difference method, which considers Q the same for both P and S waves.

The velocity model used in simulation comprises two types; the Mindavelli model without basin and Mindavelli model with basin. We replaced the first flat layer with the basin layer, providing territorial variations remain constant. It is a better way to understand the effects of basin geometry on the earthquake-induced motion. The demonstration of the velocity structure model is visually given in Figure 3.16; the model parameters used in the velocity model are indicated in Table 3.3.

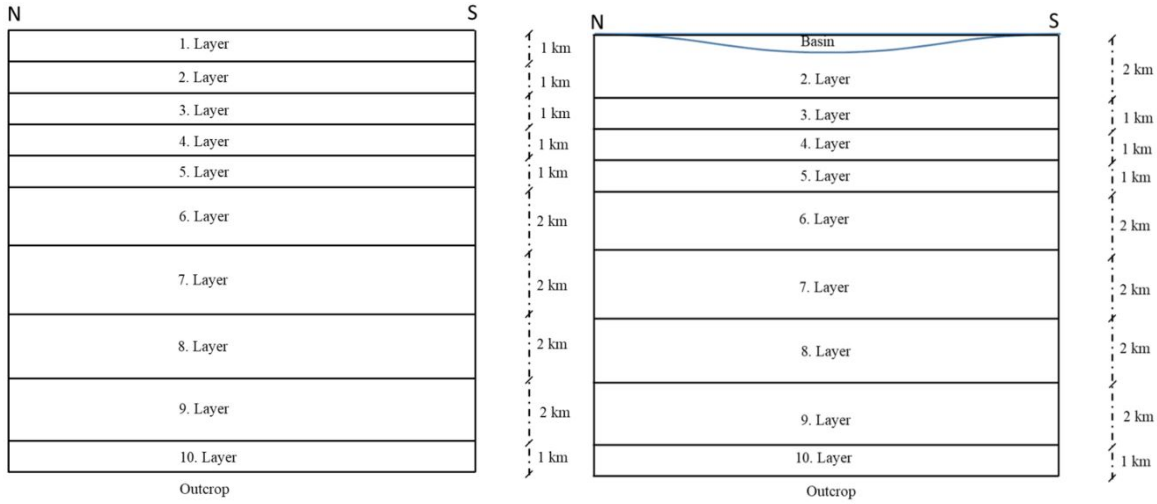

(a) (b)

Figure 3.16. Illustration of velocity structure model for Eskişehir used in simulation. (a) shows Midevalli model for Turkey with horizontally flat layers, (b) displays modified Midevalli model by adding basin structure on top.

Table 3.3. Velocity structure model based on Mindevalli and Mitchell (1989).

Layer	**V$_P$ (km/s)**	**V$_S$ (km/s)**	**Density(g/cm^3)**	**Q**
1 (Basin)	2.70	1.30	2.10	200
2	4.90	2.80	2.50	400
3	5.10	2.90	2.50	500
4	5.40	3.10	2.60	500
5	5.60	3.20	2.60	600
6	5.80	3.40	2.70	600
7	6.00	3.50	2.70	600
8	6.20	3.50	2.70	800
9	6.20	3.60	2.70	800
10	6.20	3.60	2.80	800
Outcrop	6.30	3.60	2.80	800

4. INVESTIGATION OF STRONG GROUND MOTIONS (STATIONS AND RECORDINGS)

4.1. Strong Ground Motion stations and recordings

At Eskişehir Province there have been twenty strong ground motion stations operated by AFAD. Location and V_{S30} of the stations are shown in Figure 4.1 and listed in Table 4.2 but not, 2609, 2017, 2618, 2619 and 2620 stations. Among them 5 of those stations (2601, 2602, 2604, 2611 and 2613) are located at the center of the basin and 7 (2603, 2605, 2606, 2610, 2614, 2615 and 2616) of them at the edge of the basin (Yamanaka et al., 2018).

The number of earthquakes that took place around Eskişehir is few, owing to the low seismicity of this region. The details of seismic events greater than Mw 3.5 are given in Table 4.1. In this study, two of them were used for the validation of the substructure models.

Table 4.1. Earthquakes occurred vicinity of Eskişehir.

Magnitude (Mw)	Date/Time	Location		Source	Str(°)/Dip(°)/Rake(°)	Depth (km)	Seismic Moment (Mo, dyne*cm)	Recording stations
		Lat.(°)	long.(°)					
3.7	18.09.2015/22:30:28	39.81	30.45	KOERI	277/32/-65	7	4.28E+21	2601, 2602, 2604, 2606, 2610, 2611, 2614, 2615
4.1	24.07.2020/02:19:15	39.8478	30.4398	AFAD	289/65/-111	10.84	—	2602, 2605, 2606, 2612, 2613, 2615
4.3	17.01.2015 /00:42:34.00	40.09	30.53	ISC	273/82/-86	10	3.04E+22	2601, 2602, 2606, 2610, 2611, 2612, 2613, 2614, 2615, 2616

In the following chapter strong ground motion recordings of the 2011 Simav event are investigated. The location of seismic station recorded this event are shown in Figure 4.1.

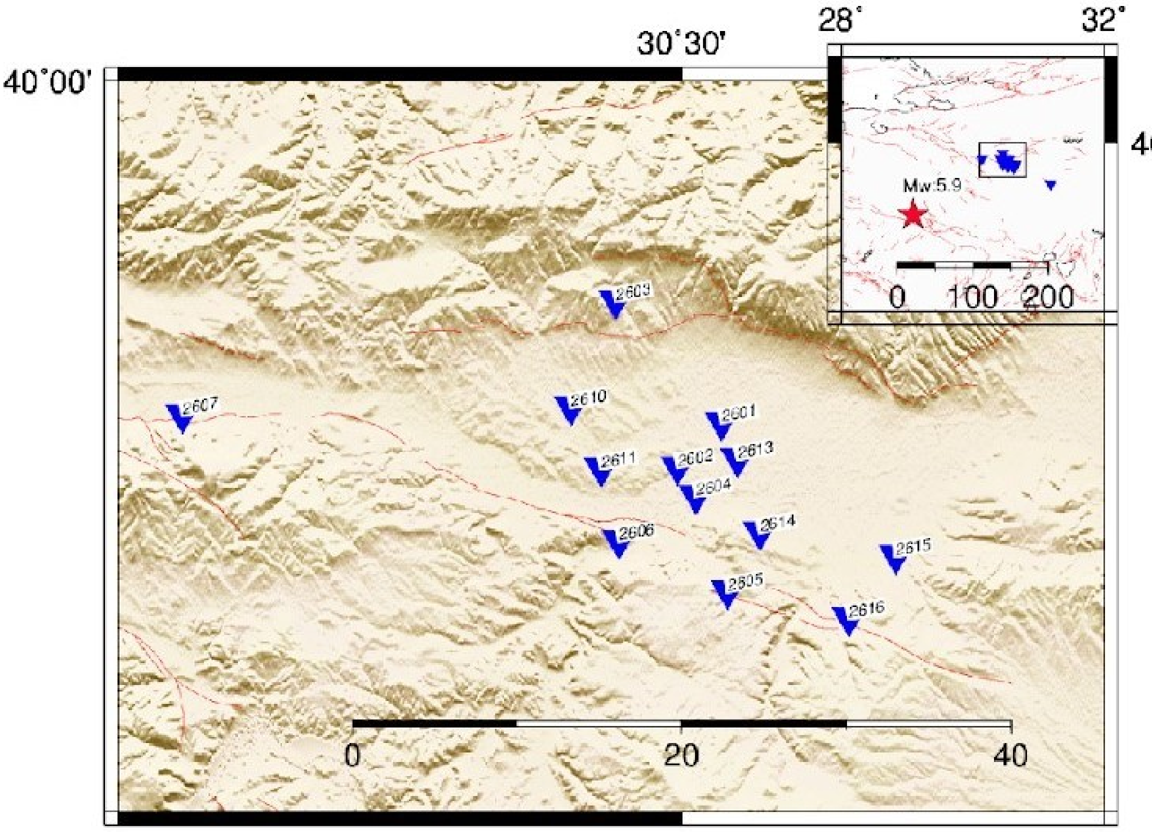

Figure 4.1. Distribution of the stations at Eskişehir. Red lines are active faults in the region (https://www.mta.gov.tr), red star shows the epicenter of the 2011 Simav Earthquake.

Table 4.2. Information of strong ground motion stations at Eskişehir.

Station	**Longitude**	**Latitude**	**V^*_{S30} (m/s)**
2601	30.528	39.814	237
2602	30.497	39.789	328
2603	30.453	39.880	631
2604	30.510	39.773	298
2605	30.533	39.133	439**
2606	30.456	39.749	348
2607	30.146	39.817	265
2608	31.183	39.520	481
2610	30.422	39.822	243
2611	30.443	39.788	275

Table 4.2. Information of strong ground motion stations at Eskişehir. (cont.)

Station	**Longitude**	**Latitude**	**V*$_{S30}$ (m/s)**
2612	39.767	30.405	441
2613	30.540	39.794	281
2614	30.556	39.753	516
2615	30.652	39.740	307
2616	30.619	39.706	471

∗obtained from Yamanaka et al. (2018),∗∗ acquired from USGS.

4.2. The 2011 Simav Earthquake Mw 5.9

A strong earthquake occurred on May, 2011 in Simav district of Kütahya province in Western Turkey. Simav is located on graben structure, which is encompassed by active faults. Moment magnitude of the earthquake is announced as Mw 5.9 by GCMT (Global Centroid Moment Tensor Project). The 2011 Simav earthquake was well recorded by thirteen strong motion stations located in and around Eskişehir which is almost 140 km away from epicenter. Max PGA (13.3 cm/s^2) was recorded at 2606 station 139 km away from the epicenter The maximum peak ground velocity (PGV) (1.5 cm/s), on the other hand, recorded by 2610 , edge of basin. The max. PGA and PGV was investigated in the center and edge part of the basin.

Another noticeable point is that PGV value at 2610 has arrived after S-waves arrival time at 0.62 s period (1.61 Hz), as shown in Figure 4.5.

Location and source geometry information of the event are acquired from GCMT.

Table 4.3. Moment tensor solution of Simav earthquake 19.05.2011 Mw 5.9 from the GCMT (https://www.globalcmt.org).

Date-Time (UTC)	Location		Mw	Depth (km)	Mo (dyne*cm)	Strike (°)	Dip (°)	Rake (°)
	Lat.	Long.						
19.05.2011-20:15	39.080°	29.110°	5.9	12.1	8.75E+25	286	46	-85

In addition to these, pseudo spectral acceleration (PSA) with 5% damped for the elastic single degree of freedom system is acquired from recordings at different periods, namely 1 s, 2 s, and 3 s. PSA belonging to the center and margin basin have a higher value, especially the basin center, except for 2601 (e.g. 2602-2611).

Table 4.4. PSA and distance parameters.

Station	**Long. (°)**	**Lat. (°)**	**V_{S30} (m/s)**	**Location**	**R_{epi} (km)**	**R_{hyp} (km)**	**R_{jb} (km)**	**PGV (cm/s)**	**PGA (cm/s^2)**	**PSA 1s (cm/s^2)**	**PSA 2s (cm/s^2)**	**PSA 3s (cm/s^2)**
2601	30.528	39.814	237	Center	145.41	145.92	139.80	0.54	6.94	7.81	1.05	0.65
2602	30.497	39.789	328	Center	141.74	142.26	136.11	0.92	7.04	12.56	10.07	2.98
2603	30.453	39.880	630	Edge	144.04	144.55	138.60	0.61	7.01	3.31	1.94	1.23
2604	30.510	39.773	296	Center	141.79	142.31	136.13	0.98	9.90	16.53	4.07	1.73
2606	30.456	39.749	348	Edge	139.39	139.91	133.70	0.92	13.30	7.82	3.07	1.53
2607	30.146	39.817	267	Outside	118.90	119.51	113.70	0.88	7.30	8.96	3.42	2.98
2608	31.183	39.520	480	Outside	185.76	186.16	179.69	0.17	1.55	1.38	0.69	0.52
2610	30.422	39.822	289	Edge	138.18	138.71	132.66	1.50	11.18	18.42	5.39	2.30
2611	30.443	39.788	275	Center	137.70	138.24	132.12	1.33	10.29	12.26	8.43	5.47
2613	30.540	39.794	281	Center	145.11	145.61	139.46	1.14	9.89	11.60	7.11	2.13
2614	30.556	39.753	516	Edge	144.15	144.65	138.42	0.60	4.25	6.74	3.99	1.55
2615	30.652	39.740	307	Edge	150.81	151.30	145.02	1.32	7.97	16.73	7.00	3.74
2616	30.619	39.706	471	Edge	146.61	147.11	140.79	0.51	4.83	5.15	1.87	1.17

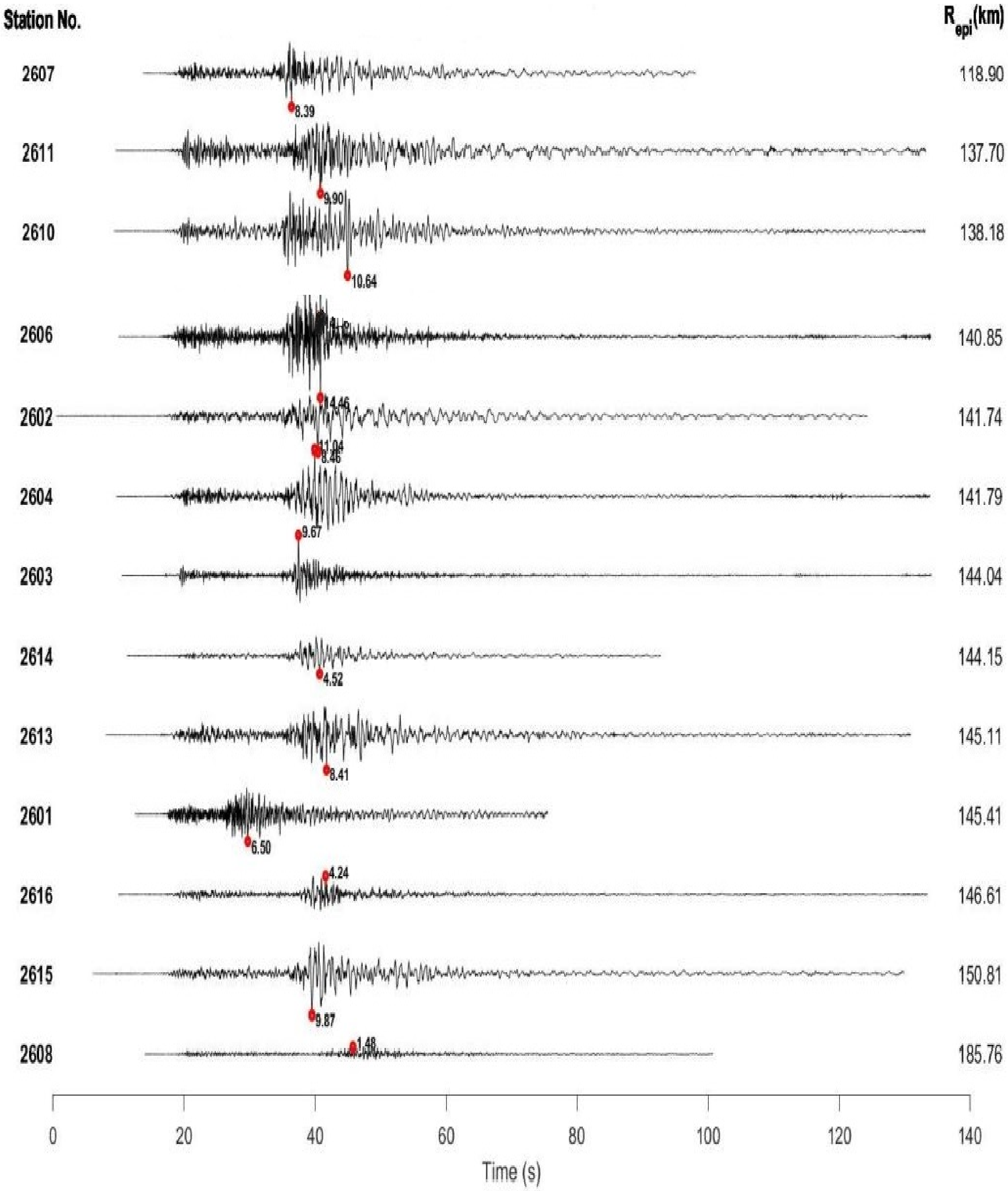

Figure 4.2. Accelerograms of the 2011 Simav earthquake at Eskişehir stations, raw EW components.

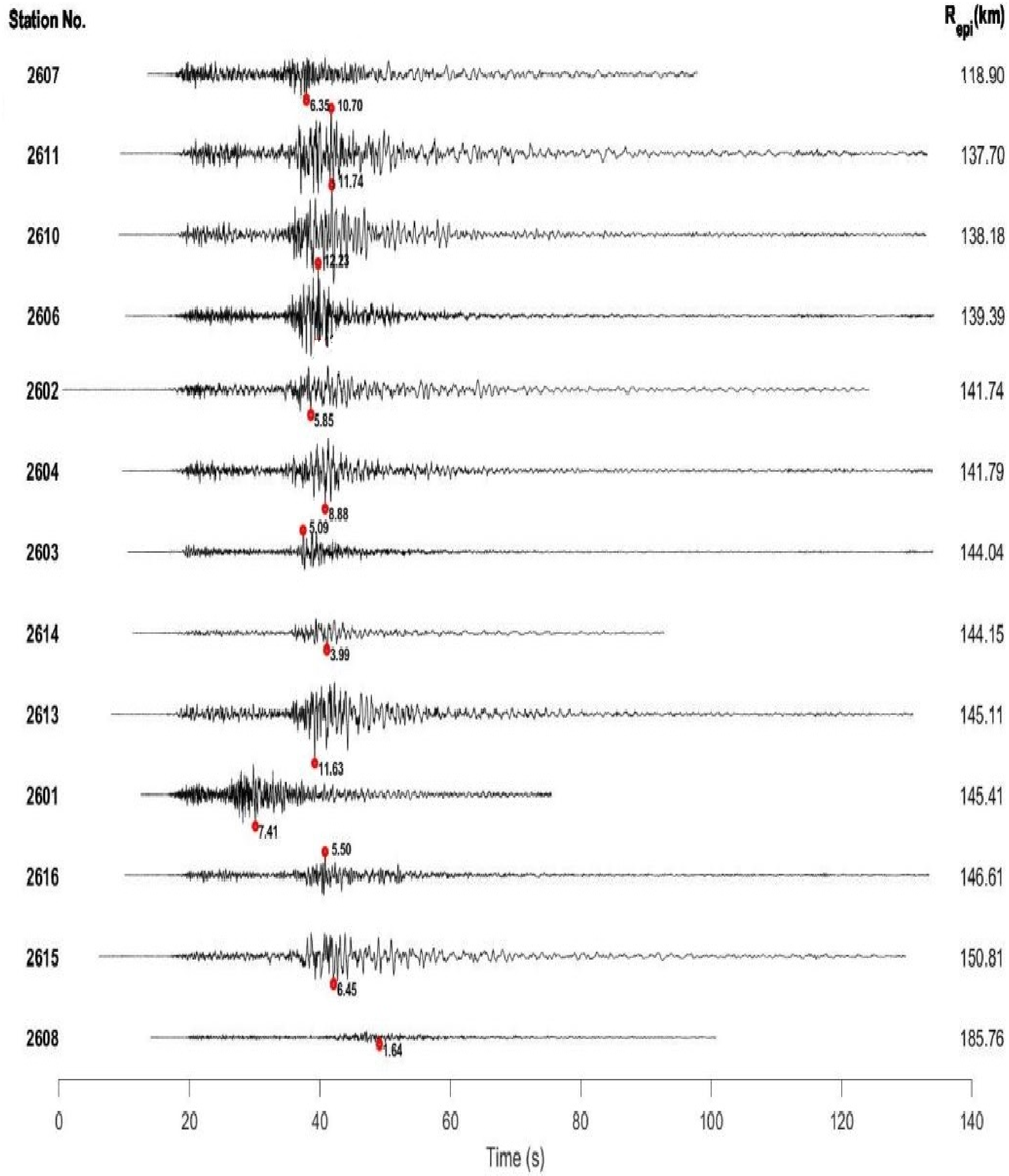

Figure 4.3. Accelerograms of the 2011 Simav earthquake at Eskişehir stations, raw NS components.

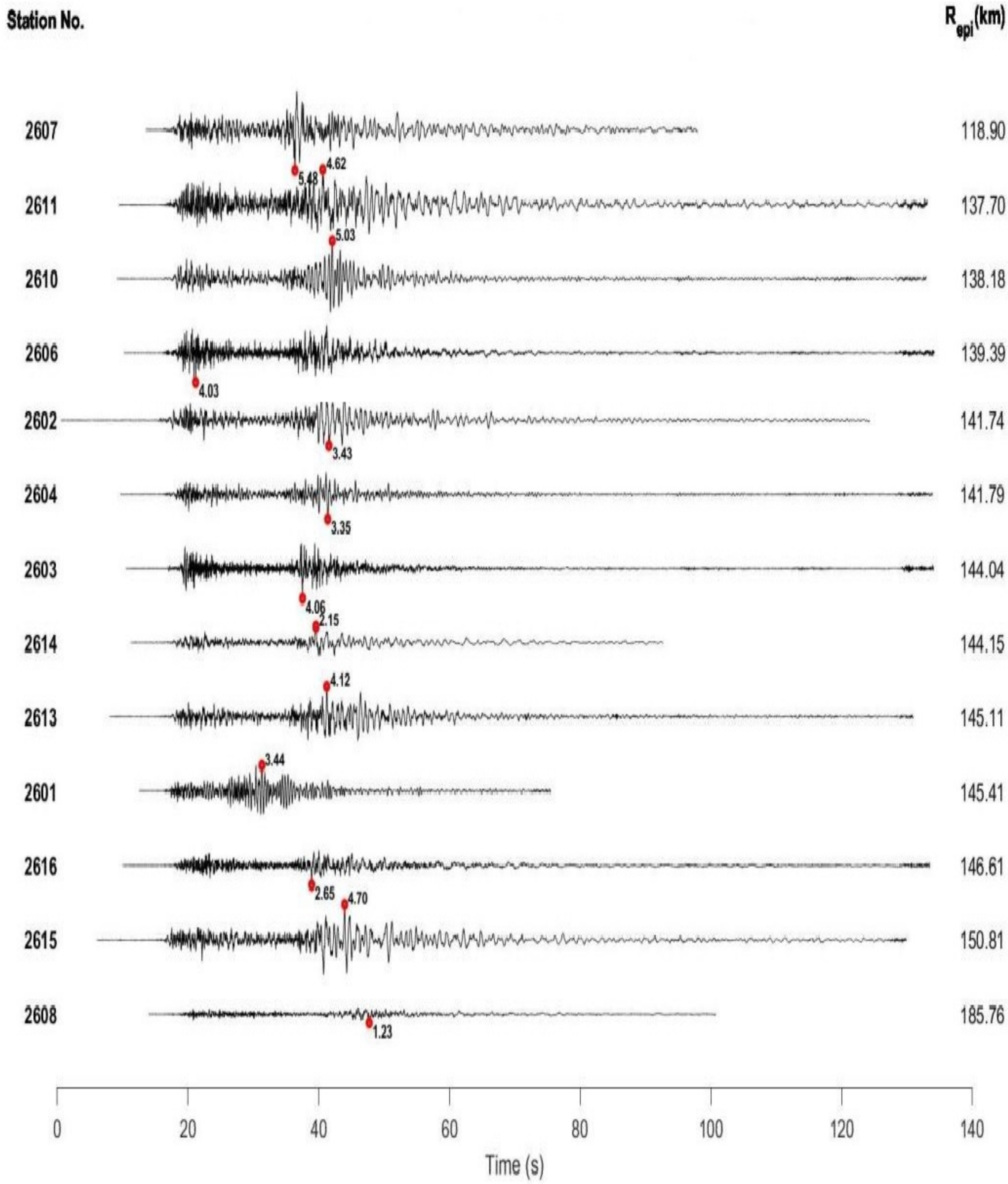

Figure 4.4. Accelerograms of the 2011 Simav earthquake at Eskişehir stations, raw UD components.

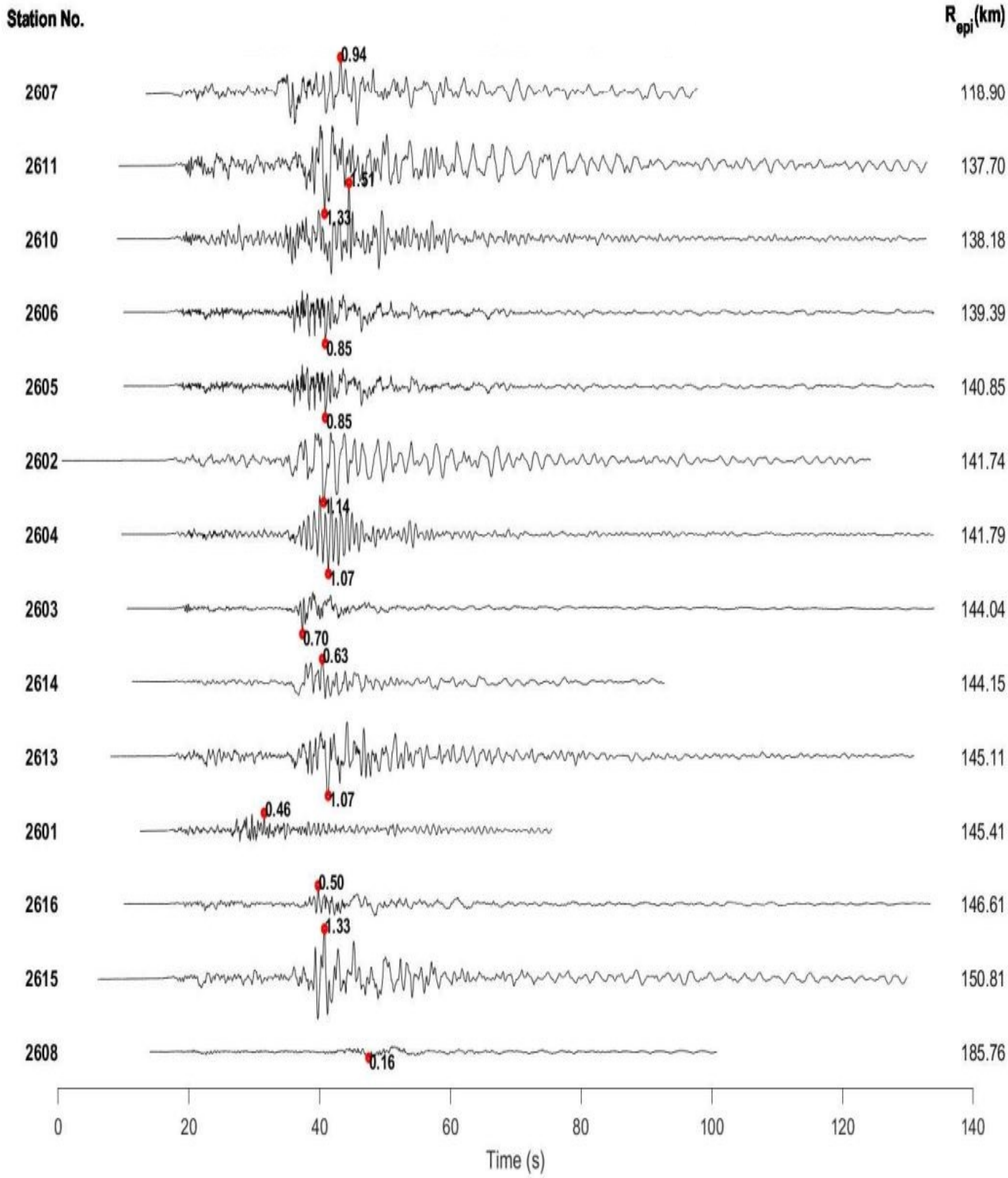

Figure 4.5. Velocity time series of Simav Earthquake at Eskişehir stations, raw EW components.

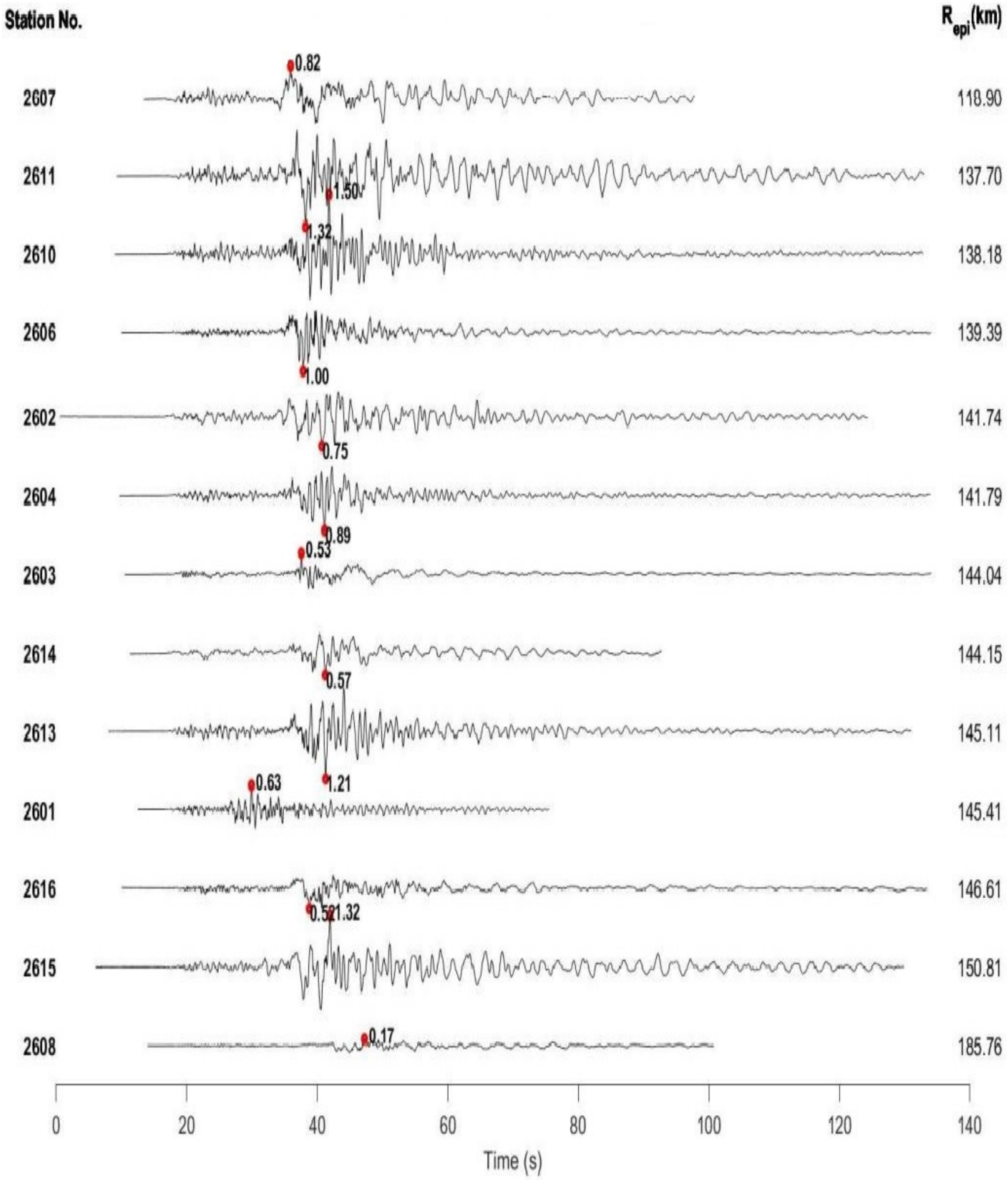

Figure 4.6. Velocity time series of Simav Earthquake at Eskişehir stations, raw NS components.

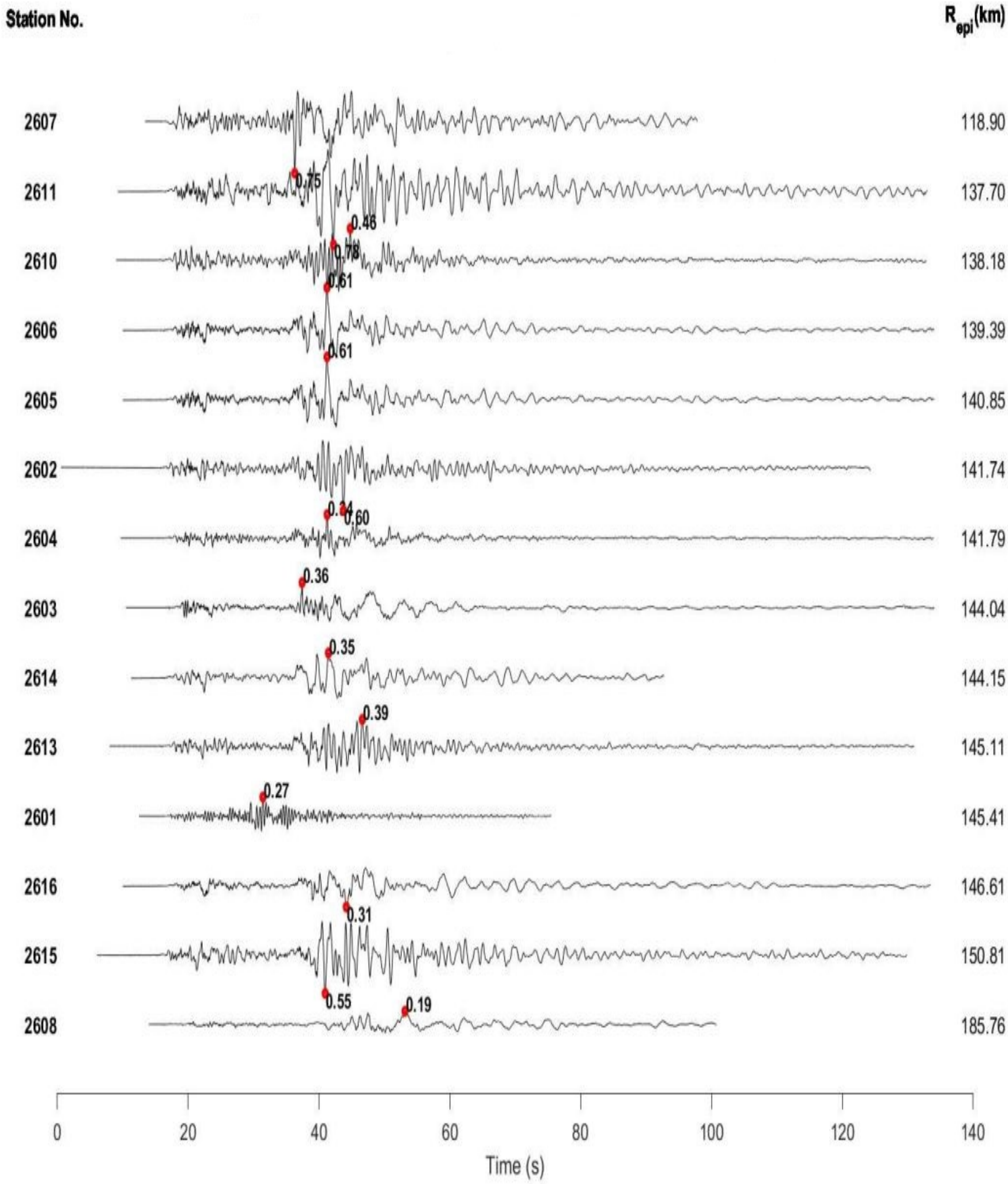

Figure 4.7. Velocity time series of Simav Earthquake at Eskişehir stations, raw UD components.

4.2.1. Significant Duration

The characteristics of the ground motions consist of the frequency content, amplitude and duration. The recorded data varies from one to one with respect to these parameters such as peak ground motion values (acceleration, velocity, and displacement), the frequency content of the ground motion, and intensity measures. The discrepancy among seismic motions may originate from many criteria, namely magnitude, source to site distance, focal mechanism, local site condition, and directivity effects. These measures play a prominent role in the evaluation of the existing facilities and the design of new systems (Bozorgnia and Bertero (2004)).

One of the most important parameters indicating potentially the level of the damage to the environment is the duration. There are many definitions of the duration, namely Bracketed duration (Db), Uniform duration (Du), Significant Duration (Ds), and Effective Strong Motion Duration (De). The significant duration is the time interval between the points at which 5% and 95% of total energy or 5% and 75% of total energy (Trifunac and Brady (1975); Dobry et al. (1978)). Accumulation of energy in the accelerogram is represented by the Arias intensity (Arias, Arturo (n.d.)). The Arias intensity is the integral of the square of the acceleration time history as follows.

$$I_{ax} = \frac{\pi}{2g} \int_0^{T_d} a_x^2(t)dt \tag{4.1}$$

where, I_{ax} is the Arias intensity along the x axis, $a_x(t)$ the acceleration time history along the x-axis, T_d is the total duration of the seismic motion and g is the gravity.

In the scope of this study, the Ds of the Simav earthquake 2011 Mw 5.9 was examined for stations located at Eskişehir. Those are given in Table 4.5. We have also compared observed duration with estimated values by predictive model suggest by Sandıkkaya and Akkar (2017). They have developed the predictive GMIMs by using a set of data from the boarder European region for shallow active crustal regions. The predictive models are capable of predicting the geometric mean of $\mathrm{SD}_{5-75\%}$, $\mathrm{SD}_{5-95\%}$, cumulative absolute velocity (CAV) and I_A. The models have limited the magnitude between $4 \leq Mw \leq 8$, the distance up to 200 km and 150 m/s $\leq V_{S30} \leq$ 1200 m/s.

Table 4.5. Significant duration of the 2011 Mw 5.9 Simav earthquake recordings.

Station	**Longitude**	**Latitude**	**R_{jb} (km)**	**V_{S30} (m/s)**	**D 5-75% (s)**		**D 5-95% (s)**	
					N-S	**E-W**	**N-S**	**E-W**
2601	30.528	39.814	139.80	237	12.87	13.34	27.70	33.57
2602	30.497	39.789	136.11	328	22.88	14.49	46.16	37.06
2603	30.453	39.880	138.60	630	20.11	19.15	31.90	30.31
2604	30.510	39.773	136.13	296	19.34	14.00	36.31	24.05
2606	30.456	39.749	133.70	348	13.94	17.01	24.94	29.43
2607	30.146	39.817	113.70	267	27.85	21.47	48.36	40.81
2608	31.183	39.520	179.69	480	27.76	29.86	47.37	44.98
2610	30.422	39.822	132.66	289	17.26	19.52	30.65	32.61
2611	30.443	39.788	132.12	275	22.76	27.69	53.77	53.18
2613	30.540	39.794	139.46	281	17.56	22.40	32.42	40.94
2614	30.556	39.753	138.42	516	13.20	7.57	31.49	21.79
2615	30.652	39.740	145.02	307	15.35	13.20	40.02	31.28
2616	30.619	39.706	140.79	471	23.13	20.73	40.23	38.31

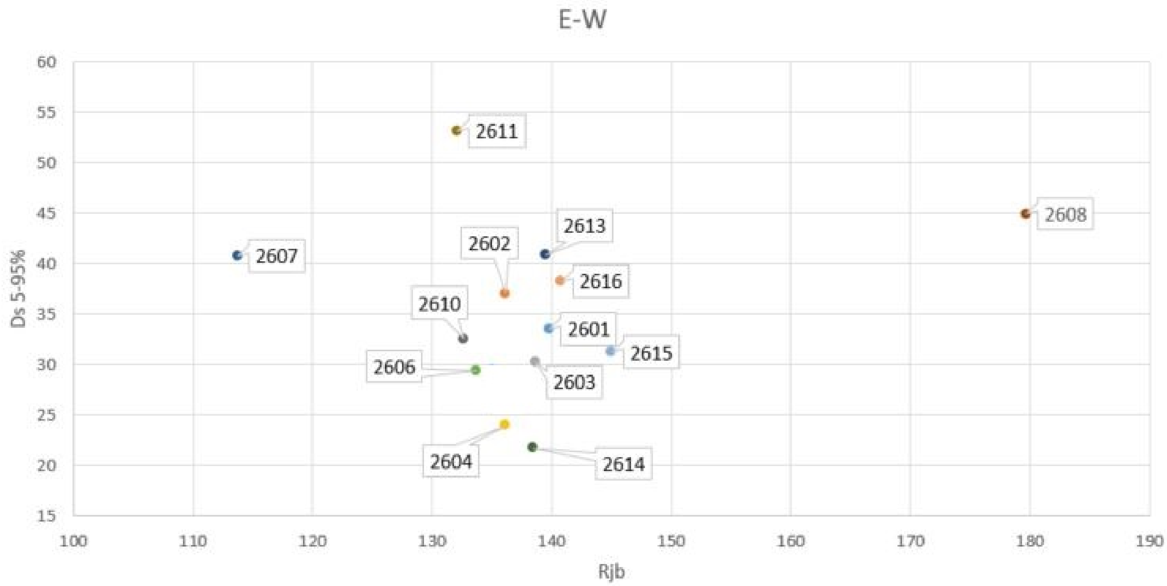

Figure 4.8. Significant duration (5-95%) of Simav earthquake Mw 5.9, EW component.

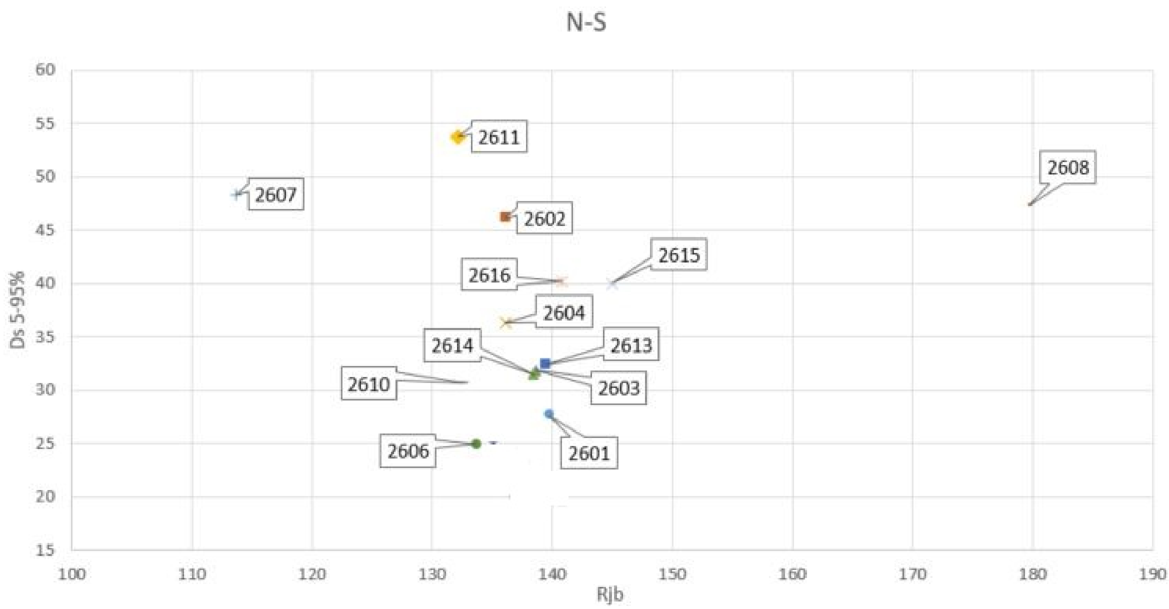

Figure 4.9. Significant duration (5-95%) of Simav earthquake Mw 5.9, NS component.

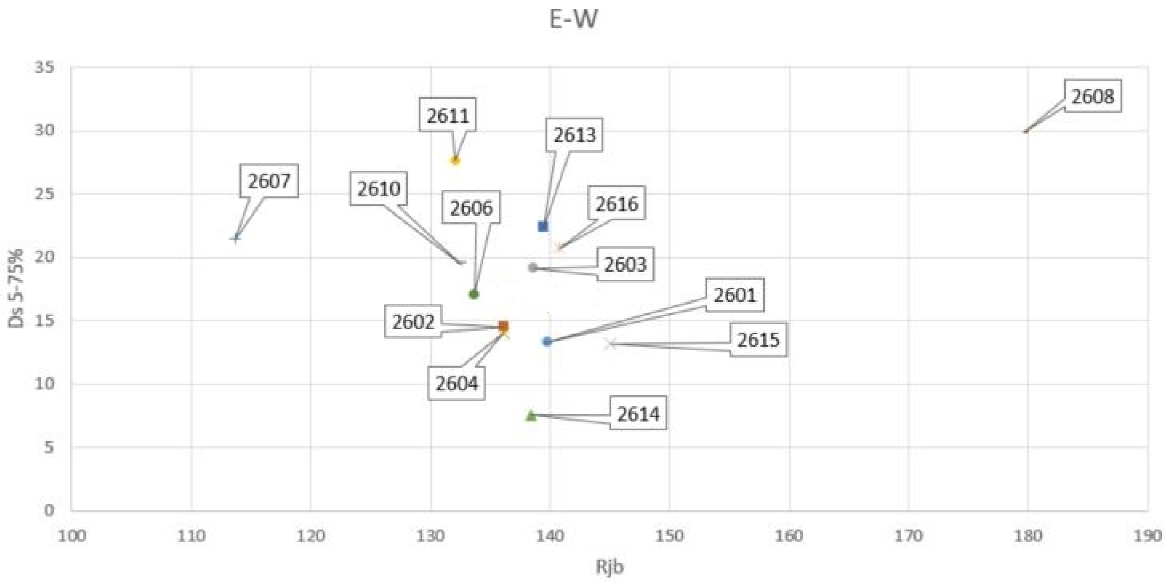

Figure 4.10. Significant duration (5-75%) of Simav earthquake Mw 5.9, EW component.

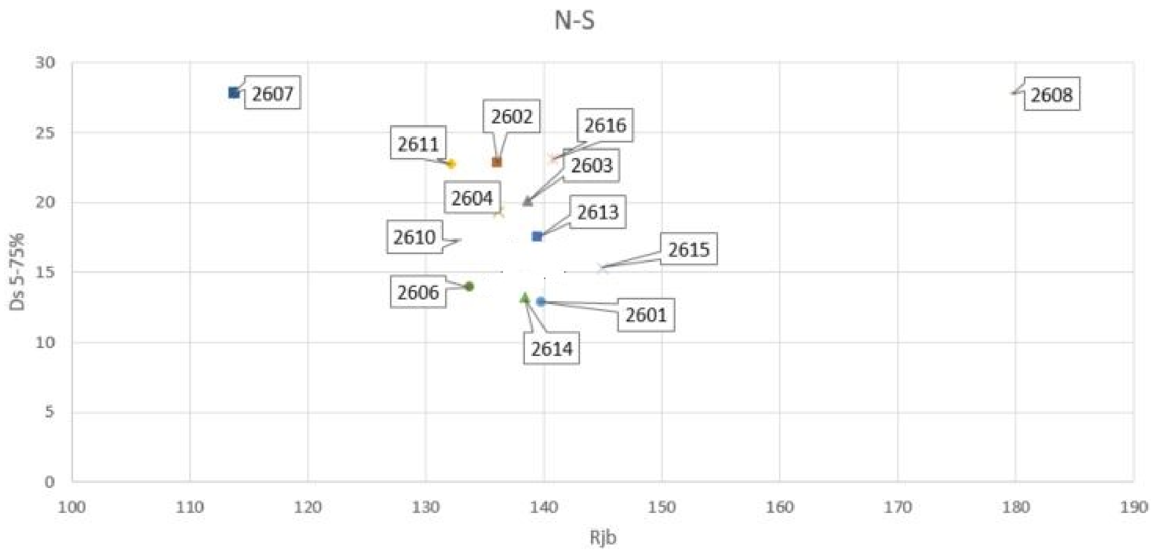

Figure 4.11. Significant duration (5-75%) of Simav earthquake Mw 5.9, NS component.

The significant durations (5-75% and 5-95%) with R_{jb}, which is the shortest distance from a site to the surface projection of the rupture plan, distances varying from 130 to 150 km have been shown in Figure 4.8-4.11 corresponding to the duration range of 21.8 to 53 s. Especially, 2611 and 2602 have a high significant duration despite the long distance. The longest significant duration recorded by the 2611 station is 53 s compared to the other stations in two horizontal directions. Generally, the center of basin stations, namely 2602, 2613, and 2615 get the longer duration.

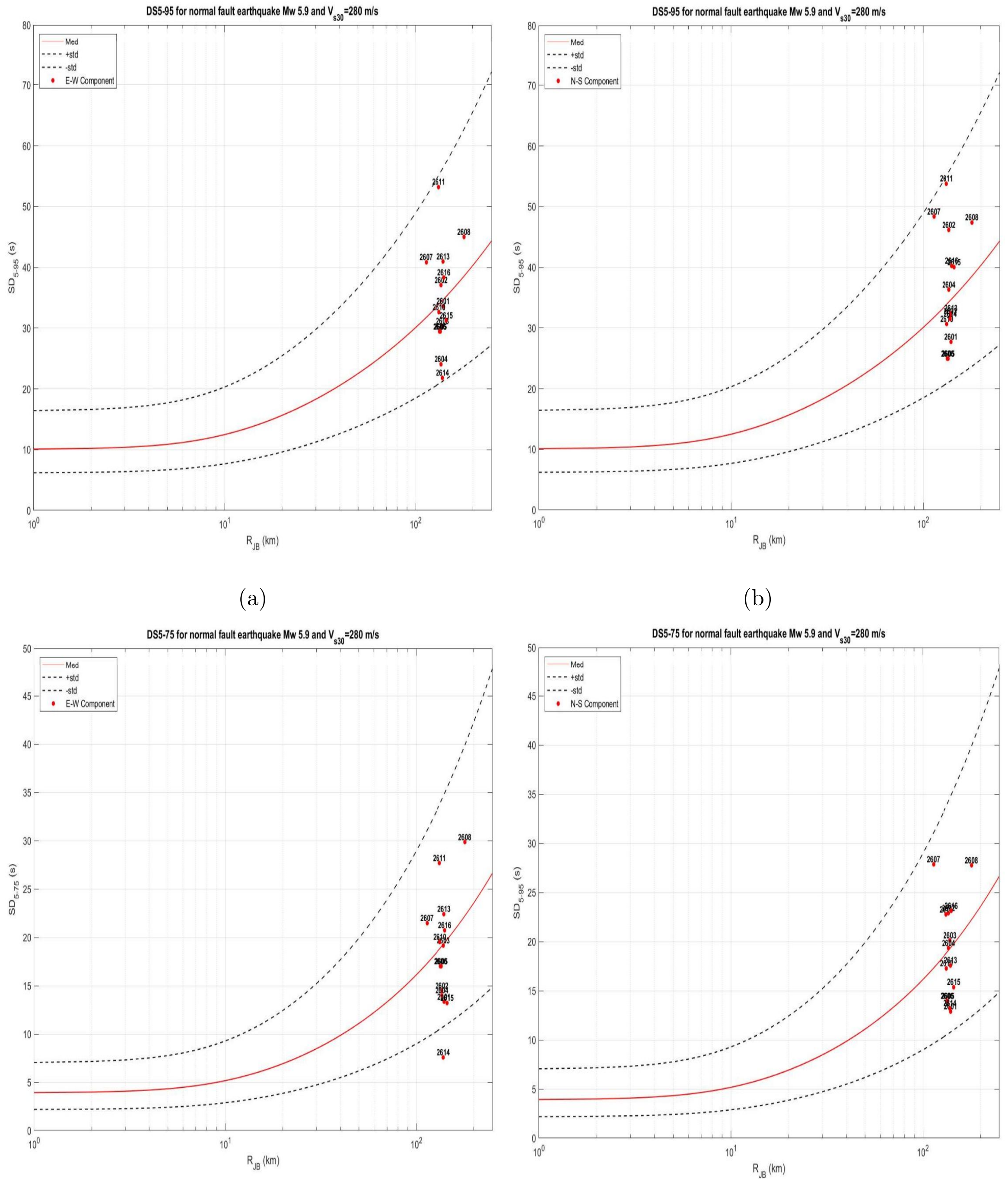

(a) (b)

(c) (d)

Figure 4.12. Comparison of Ds of Simav earthquake Mw 5.9 with GMIM model improved by Sandıkkaya and Akkar (2017) for horizontal components. (a) and (b) show the Ds (5-95%) for normal fault earthquake Mw 5.9 and V_{S30} = 280 m/s. (c) and (d) indicate the the Ds (5-75%) for normal fault earthquake Mw 5.9 and V_{S30} = 280 m/s.

The comparison was performed by using V_{S30} 280 m/s and normal fault earthquake Mw 5.9. Why the reason for selecting the V_{S30} 280 m/s is to represent the local site effect of the basin. We considered the basin center's average shear wave velocity up to 30 m. Results demonstrate that the observed motion duration at the distinct site is usually within the median + or - standard deviation, as shown Figure 4.12.

4.2.2. Comparison with Ground Motion Prediction Equations (GMPEs)

Ground motion prediction equations(GMPEs) predict the ground motion intensity measures (e.g., PGA, PGV, and Sa at distinct periods, etc.) at a certain location by taking the source, path and local site condition effects into account. The general form of GMPEs is the natural logarithm function which stems from the earthquake source theory Joyner and Boore (1981), also widely used by developers.

$$\mathrm{In}(Y) = f(M) \cdot f(R) \cdot f(SC) \cdot f(SoF) \pm \varepsilon\sigma \tag{4.2}$$

In this equation, these components stand for the different effects such as Magnitude $f(M)$ Source to site distance $f(R)$ Site class $f(SC)$, Style of Fault or Fault Mechanism $f(SoF)$. These parameters are adopted in GMPEs models and are independent variables. In addition to these, the standard deviation (σ) and standard normal variable (ϵ) represent scattering earthquake data and uncertainty which fall into two categories as aleatory uncertainty (randomness) and epistemic uncertainty (lack of knowledge). The former is related to randomness or inherent variability and it cannot be also reduced by obtaining information or data. The latter originates from the lack of knowledge and it can be reduced by adding developed information. By means of the last term ($\pm\ \epsilon\sigma$) in the equation, the below or above the estimated logarithmic mean (median) is adjusted to the GMPEs model (Sucuoğlu et al., 2014).

Gülerce et al. (2016) evaluated the compatibility between the NGA-W1 GMPEs and Turkish strong ground motion data set in terms of the site effects, magnitude, and distance scaling. They asserted that incompatibilities in small to moderate magnitude scaling, large distance scaling, and site amplification were observed. They modified

NGA-W1 GMPEs by means of the adjustment function for the best fitting with NGA-W1 GMPEs.

In this thesis, two GMPEs models developed or adjusted for Turkey were selected. These GMPEs models are Kale et al. (2015) and Gülerce et al. (2016). PGA, Sa (T= 1, 2 and 3 s) by two models were examined and compared with the recorded Simav earthquake (19/05/2011, Mw 5.9). The input parameters for the Simav earthquake such as seismic moment, fault type, depth, and distance are obtained from GCMT and observed data gained from AFAD.

Another step is the residual analysis which is carried out for the comparison of recorded value with the predicted value acquired from GMPEs. In this way, it declares whether the predicted value is overestimated or underestimated.

Table 4.6. Predicted PGA and PSA values of the 2011 Mw 5.9 Simav earthquake recordings in Eskişehir - GMPE by Gülerce et al. (2016).

Station Code	PGA 0.01s (cm/s^2)	PSA 1s (cm/s^2)	PSA 2s (cm/s^2)	PSA 3s (cm/s^2)
2601	8.97	13.38	4.39	1.98
2602	7.71	9.94	3.30	1.50
2603	6.60	5.89	1.99	0.93
2604	8.18	10.98	3.63	1.65
2606	7.63	9.49	3.15	1.44
2607	11.04	13.74	4.45	2.03
2608	4.03	5.64	1.97	0.90
2610	8.60	11.44	3.77	1.71
2611	8.90	12.04	3.95	1.79
2613	8.15	11.36	3.75	1.70
2614	5.76	6.30	2.14	0.99
2615	7.32	10.15	3.38	1.53
2616	5.93	6.81	2.30	1.06

Table 4.7. Predicted PGA and PSA values of the 2011 Mw 5.9 Simav earthquake recordings in Eskişehir - GMPE by Kale et al. (2015).

Station Code	PGA 0.01 (cm/s^2)	PSA 1 (cm/s^2)	PSA 2 (cm/s^2)	PSA 3 (cm/s^2)
2601	6.03	11.56	4.42	2.23
2602	5.54	8.60	3.39	1.74
2603	4.12	4.37	1.84	0.99
2604	5.77	9.53	3.71	1.90
2606	5.56	8.25	3.26	1.69
2607	7.86	12.46	4.73	2.40
2608	3.07	4.50	1.90	1.01
2610	6.06	9.99	3.88	1.98
2611	6.21	10.54	4.07	2.07
2613	5.68	9.81	3.81	1.94
2614	4.49	5.36	2.21	1.18
2615	5.16	8.66	3.41	1.75
2616	4.54	5.79	2.37	1.25

Table 4.8. Recorded PGA and PSA Values of the 2011 Mw 5.9 Simav Earthquake recordings in Eskişehir

Station Code	PGA (cm/s^2)	PSA 1s (cm/s^2)	PSA 2s (cm/s^2)	PSA 3s (cm/s^2)
2601	6.94	7.81	1.05	0.65
2602	7.04	12.56	10.07	2.98
2603	7.01	3.31	1.94	1.23
2604	9.90	16.53	4.07	1.73
2606	13.30	7.82	3.07	1.53
2607	7.30	8.96	3.42	2.98
2608	1.55	1.38	0.69	0.52
2610	11.18	18.42	5.39	2.30
2611	10.29	12.26	8.43	5.47
2613	9.89	11.60	7.11	2.13
2614	4.25	6.74	3.99	1.55
2615	7.97	16.73	7.00	3.74
2616	4.83	5.15	1.87	1.17

Table 4.9. Residual values - GMPE by Gülerce et al. (2016).

2601		2602		2603		2604	
T	In(recd./pred.)	T	In(recd./pred.)	T	In(recd./pred.)	T	In(recd./pred.)
0.01	-0.26	0.01	-0.09	0.01	0.06	0.01	0.19
1	-0.54	1	0.23	1	-0.58	1	0.41
2	-1.43	2	1.12	2	-0.02	2	0.11
3	-1.11	3	0.68	3	0.28	3	0.05
2606		2607		2608		2610	
T	In(recd./pred.)	T	In(recd./pred.)	T	In(recd./pred.)	T	In(recd./pred.)
0.01	0.56	0.01	-0.41	0.01	-0.95	0.01	0.26
1	-0.19	1	-0.43	1	-1.41	1	0.48
2	-0.03	2	-0.26	2	-1.06	2	0.36
3	0.06	3	0.38	3	-0.55	3	0.30
2611		2613		2614		2615	
T	In(recd./pred.)	T	In(recd./pred.)	T	In(recd./pred.)	T	In(recd./pred.)
0.01	0.15	0.01	0.19	0.01	-0.30	0.01	0.09
1	0.02	1	0.02	1	0.07	1	0.50
2	0.76	2	0.64	2	0.62	2	0.73
3	1.12	3	0.23	3	0.45	3	0.89
2616							
T	In(recd./pred.)						
0.01	-0.21						
1	-0.28						
2	-0.21						
3	0.10						

Table 4.10. Residual values - GMPE by Kale et al. (2015).

2601		2602		2603		2604	
T	In(recd./pred.)	T	In(recd./pred.)	T	In(recd./pred.)	T	In(recd./pred.)
0.01	0.14	0.01	0.24	0.01	0.53	0.01	0.54
1	-0.39	1	0.38	1	-0.28	1	0.55
2	-1.44	2	1.09	2	0.05	2	0.09
3	-1.23	3	0.53	3	0.22	3	-0.10
2606		2607		2608		2610	
T	In(recd./pred.)	T	In(recd./pred.)	T	In(recd./pred.)	T	In(recd./pred.)
0.01	0.87	0.01	-0.07	0.01	-0.68	0.01	0.61
1	-0.05	1	-0.33	1	-1.19	1	0.61
2	-0.06	2	-0.32	2	-1.02	2	0.33
3	-0.10	3	0.22	3	-0.67	3	0.15
2611		2613		2614		2615	
T	In(recd./pred.)	T	In(recd./prec.)	T	In(recd./pred.)	T	In(recd./pred.)
0.01	0.50	0.01	0.56	0.01	-0.05	0.01	0.43
1	0.15	1	0.17	1	0.23	1	0.66
2	0.73	2	0.62	2	0.59	2	0.72
3	0.97	3	0.09	3	0.28	3	0.76
2616							
T	In(recd./pred.)						
0.01	0.06						
1	-0.12						
2	-0.24						
3	-0.06						

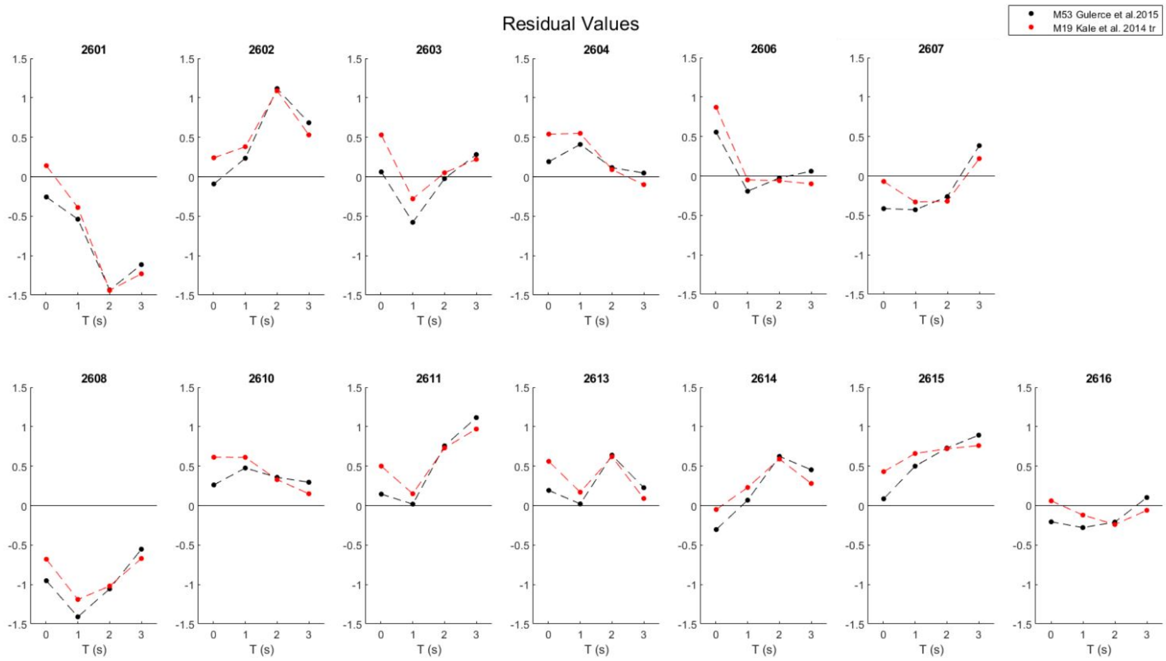

Figure 4.13. Residual value at distinct seismic stations with respect to different periods.

SA (Spectral acceleration) calculated by two GMPEs models have a similar trend at different periods. One of the outstanding results of the residual analysis is that predicted SA at distinct periods (0.01s, 1s, 2s, 3s) for 2610, 2611, 2613, 2615 stations, which are located in the edge and center of the basin, is underestimated by each of the GMPEs models. The residual value at the 2 s period reaches about 1.1 which means that SA at 2s period calculated by recordings is 3 times more than SA at 2s period estimated by GMPEs for 2602 station.

On the other hand, SA at all periods for 2601 station is overestimated by GMPEs. Although 2601 is situated in the center of the basin, recording belonging to 2601 does not contain basin effects in terms of amplitude and content of frequency. Apart from these, the predicted SA for 2608 is overestimated for almost whole periods due to existing outside of the basin.

Additionally, the basin effect of the recordings (e.g. 2601, 2603, 2604, 2606, 2608 and 2609) is negligible since the ingredient of observed data has involved the waves with low amplitude relatively. The larger amplitude arrives with S-onset. As a result, the amplitude of surface waves can be overlooked in the recordings of these stations.

4.2.3. Envelope Delay (Group Delay)

The phase is the arctangent of the ratio of imaginary parts to real parts of the Fourier transform of seismic motion. The derivative of phase with regard to frequency can be called the envelop delay. Envelop delay, known as group delay, is used for various purposes; e.g., data processing, and simulating strong ground motions. Group delay is capable of being put the expression of the frequency-dependent time shift of waves in the basin. It makes the basin structure clear with the phase spectrum of group waves. Moreover, it can also explain that the phase differences are not arbitrary (Boore, 2003). The envelope delay makes differences in arrival time intelligible at distinct frequencies. The unit of group delay is time.

In addition to these, envelope delay is used to determine the cut-off frequency by Abrahamson and Sykora (1993) in terms of the data processing. If there is a spike in seismic data, it shows us a lower frequency in earlier relative arrival time.

In view of all information, group delay time plays a prominent role in evaluating the phase properties of a wave field in a basin structure.

The numerical calculation of the phase derivatives are briefly exemplified over the continuous signal step by step at below.

- Continuous Signal,

$$x(t), \quad -\infty < t < +\infty \tag{4.3}$$

- Fourier Transform,

$$x(f) = \int_{-\infty}^{+\infty} x(t)e^{-i2\pi ft}dt \tag{4.4}$$

- Euler's Identity,

$$e^{i\omega} = \cos(\omega) + i\sin(\omega)$$
$$X(f) = \int_{-\infty}^{+\infty} x(t)\cos(2\pi ft)dt - i\int_{-\infty}^{+\infty} x(t)\sin(2\pi ft)dt \tag{4.5}$$
$$X(f) = X_R(f) - iX_I(f)$$

- Fourier Amplitude,

$$A(f) = |X(f)| = \sqrt{X_R^2(f) + iX_I^2(f)} \tag{4.6}$$

- Phase,

$$\phi(t) = \arctan\left(\frac{X_I(f)}{X_R(f)}\right) \tag{4.7}$$

- The frequency-dependent envelope delay,

$$t_e(f) = \frac{1}{2\pi}\frac{d\phi(f)}{df} \tag{4.8}$$

Sawada et al. (1998) asserted that the frequency-dependent envelope delay of earthquake records, $t_e(f)$, is generated by a component of source effects $t_e^S(f)$, propagation path, $t_e^P(f)$ and site effects $t_e^G(f)$.

$$t_e(f) = t_e^S(f) + t_e^P(f) + t_e^G(f) \tag{4.9}$$

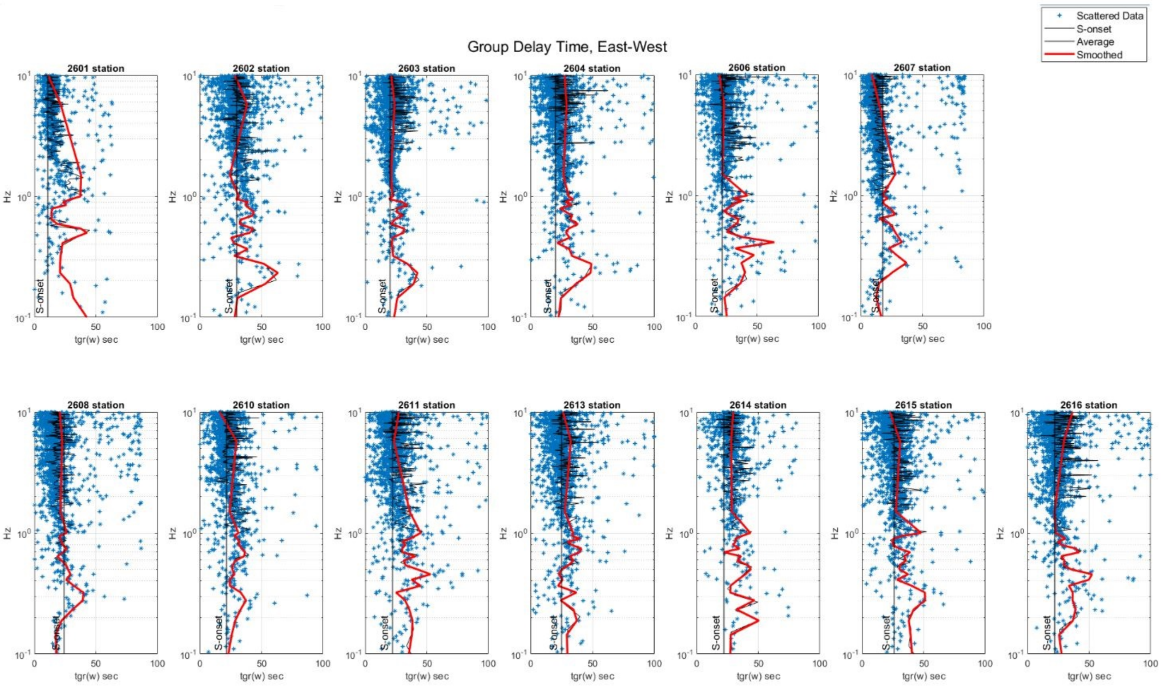

Figure 4.14. Distribution of group delay time observed at distinct seismic stations in EW direction.

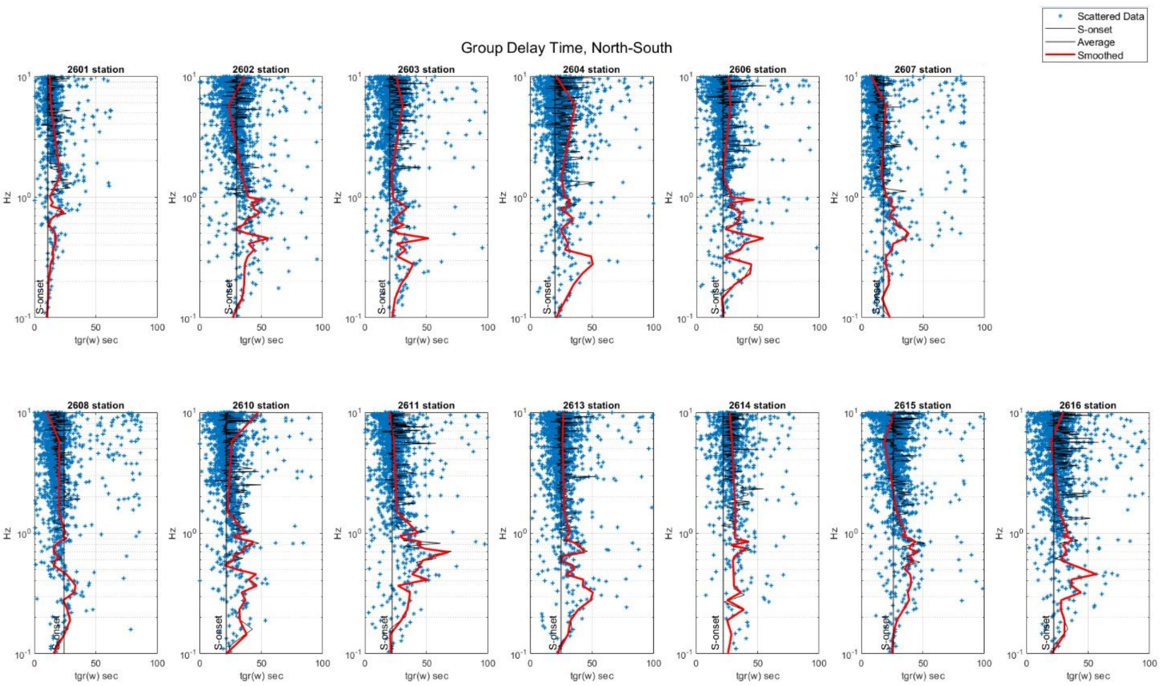

Figure 4.15. Distribution of group delay time observed at distinct seismic stations in NS direction.

Table 4.11. Maximum group delay time with respect to frequency for two directions.

	E-W		N-S	
Station	freq.(Hz)	GDT(s)	freq.(Hz)	GDT(s)
2601	0.50	32	0.74	13
2602	0.23	33	0.45	26
2603	0.23	22	0.45	32
2604	0.28	29	0.28	31
2606	0.40	43	0.45	34
2607	0.30	19	0.50	20
2608	0.30	16	0.36	9
2610	0.30	16	0.45	25
2611	0.45	31	0.69	46
2613	0.75	15	0.32	25
2614	0.20	28	0.23	17
2615	0.30	25	0.69	20
2616	0.45	30	0.45	34

The maximum Group Delay Time (GDT), which is assessed by taking away from delay time with S arrival time, has generally been restricted frequency to range of 0.2 and 0.5 Hz. Group delay times of recordings have their first high values at sites predominant frequencies such as station 2613 (fpred:0.75 Hz) and station 2601 (fpred:0.5 Hz). Then lengthening increases at lower frequencies. The maximum group delay values are observed between 0.2-0.3 Hz, in EW component of 2602, 2603 and 2604 stations. Delay is low at the 2603 station and get higher at the 2604 and 2602 stations. A large delay at the 2604 station is also clearly seen in the NS component. A similar observation can be done at 0.3 Hz in EW component of the 2615 station.As expected, stations on the basin have higher delay time. In other words lengthening of the ground motion mainly occurs at low frequencies due to very low attenuation. However, no systematic changes between the group delay of basin-edge and basin-center stations are observed with limited data.

4.2.4. Particle Motion (Surface Waves: Rayleigh waves)

Other waves can be produced due to the finite medium in all directions. Since the surface waves are restricted in the vicinity of the surface medium, it is called surface waves. There are two types of surface waves. One of the surface waves is the Rayleigh wave, while the other is the Love wave.

The Rayleigh waves are also known as ground rolls. The motion of the Rayleigh wave is not only transverse but also longitudinal with a particular phase relationship to each other. It is an elliptical motion. They also travel along with the surface medium. The amplitude of this motion is inversely proportion to the depth. The amplitude of this motion decreases rapidly with the depth. Particle motion is limited to the vertical plane containing the direction of propagation of the wave. When its passages the near the surface, its movements track the elliptical way, and also, the central axis of its motion is vertical. This movement is named retrograde. The velocity of the Rayleigh wave is more minor than S-wave, which varies from 1000 to 100 m/s. Its velocity is almost 90% velocity of S-waves inhomogeneous medium. The velocity of these waves changes with their wavelength because of the variance of the elastic constant with depth. The velocity shift with wavelength or frequency is considered dispersion (Telford et al., 1990).

The particle motion generated by the 2011 Simav Earthquake in Eskişehir was investigated and plotted below in Figure 4.16-4.20. After the S-waves arrives, wave packets are seen with a little effort by applying band pass filtering between in 0.25 and 0.5 Hz. The fundamental period of surface waves varies from 2 s to 4 s.

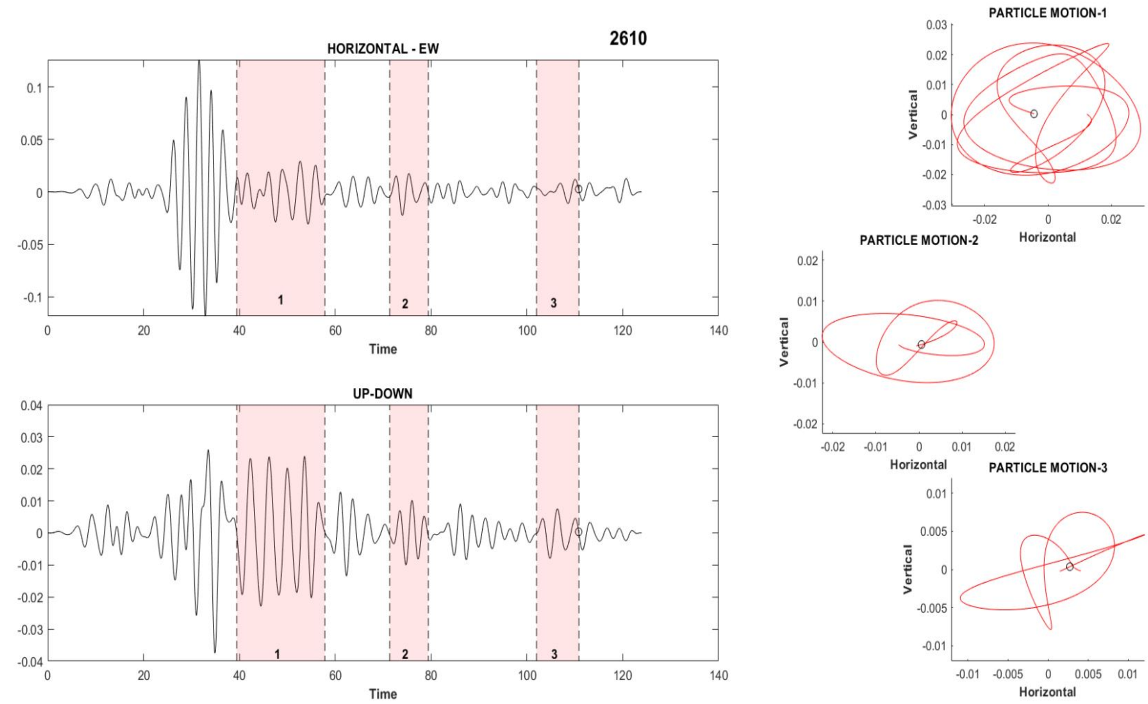

Figure 4.16. Displacement time series of the 2011 Simav Earthquake recorded by 2610 station (units of cm).

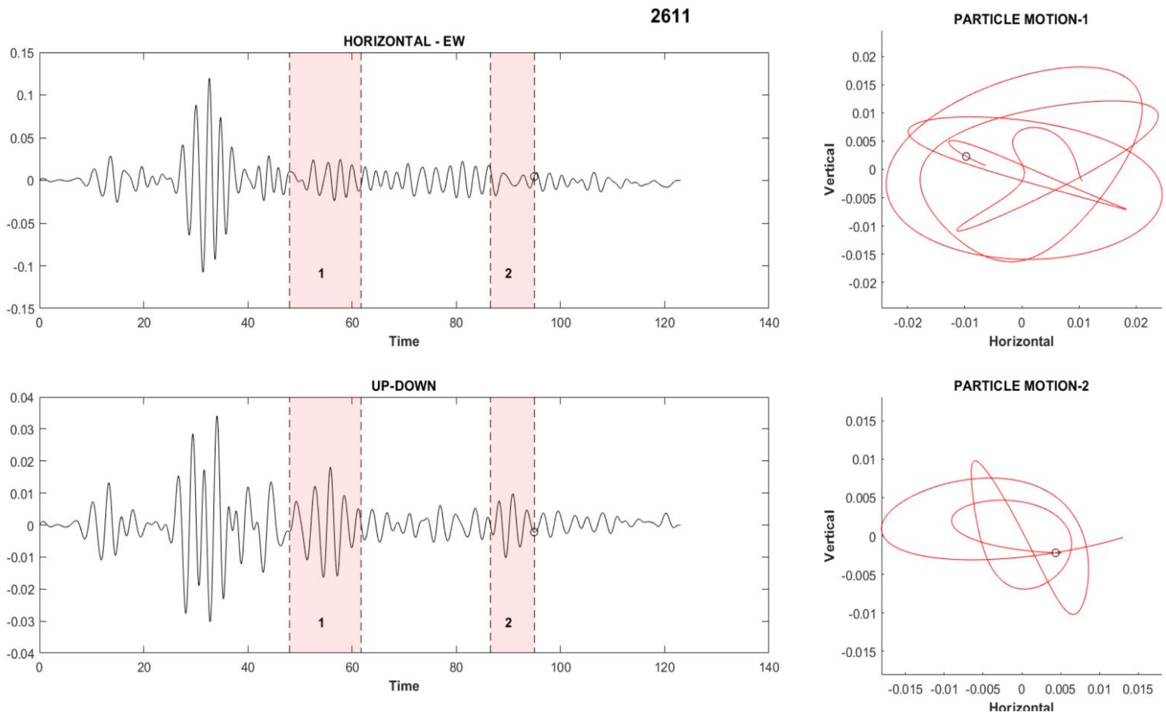

Figure 4.17. Displacement time series of the 2011 Simav Earthquake recorded by 2611 station (units of cm).

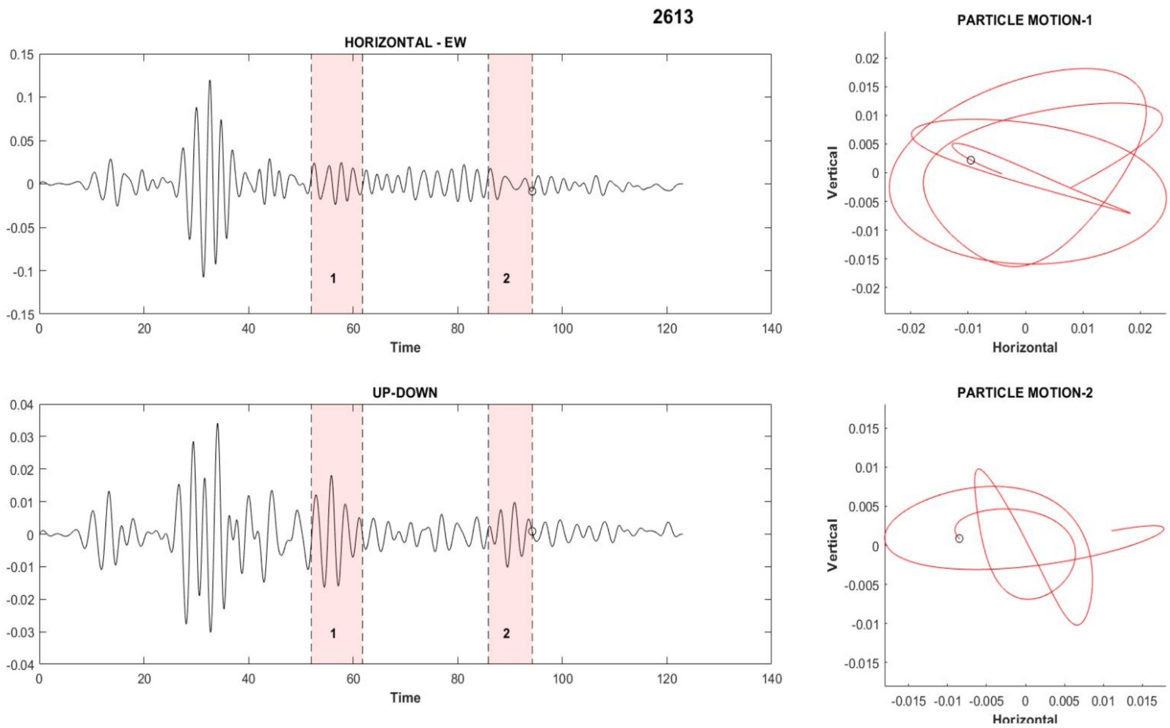

Figure 4.18. Displacement time series of the 2011 Simav Earthquake recorded by 2613 station (units of cm).

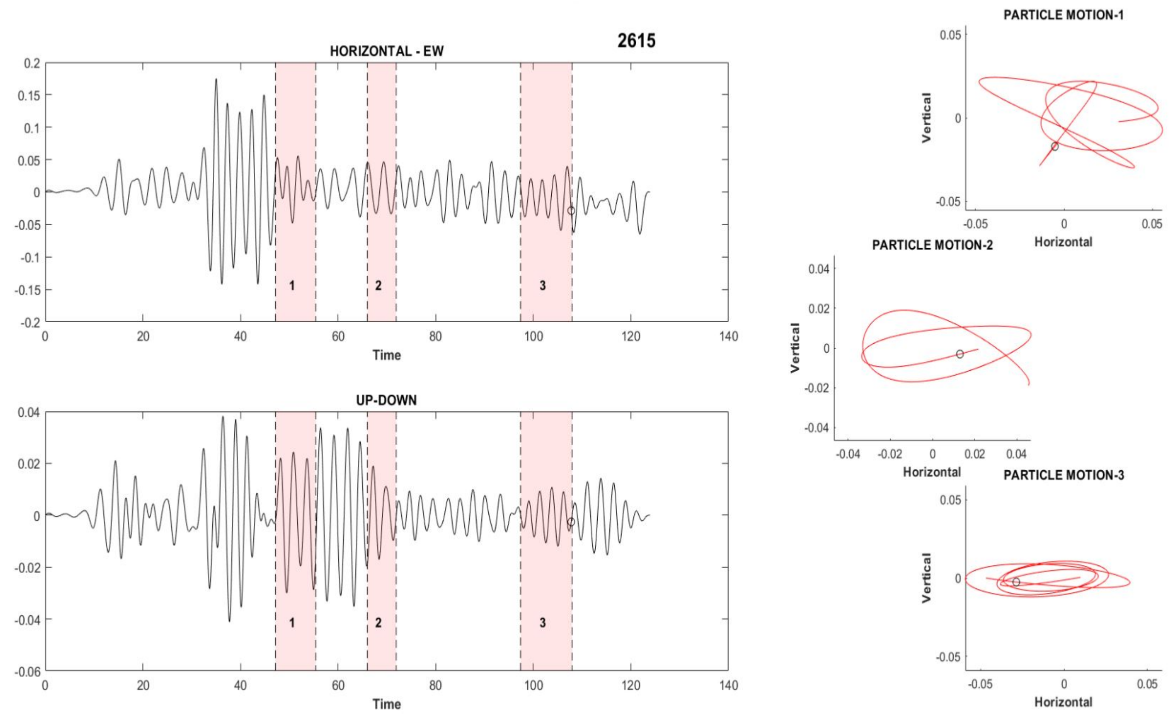

Figure 4.19. Displacement time series of the 2011 Simav Earthquake recorded by 2615 station (units of cm).

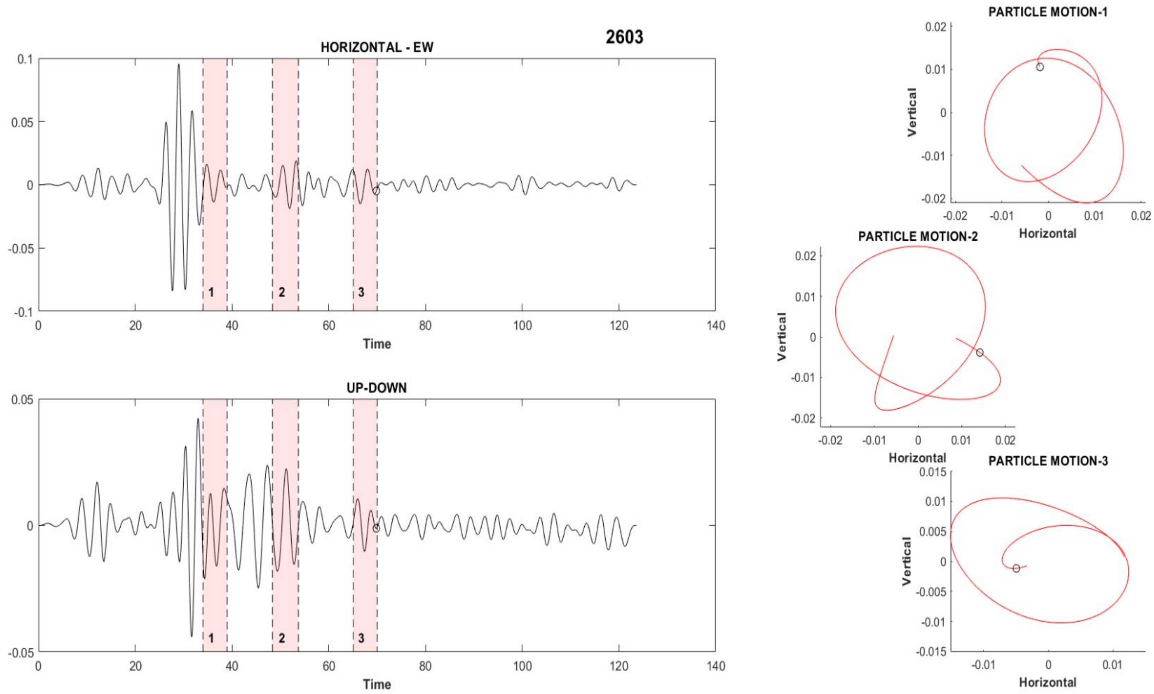

Figure 4.20. Displacement time series of the 2011 Simav Earthquake recorded by 2603 station (units of cm).

4.2.5. Earthquakes in the vicinity of Eskişehir

The earthquake on 17 Jan. 2015, Mw 4.3, occurred north of Eskişehir and outside of the basin, with a latitude of 40.06 and a longitude of 30.53. The moment tensor solution evaluated by Internatioanl Seismological Center (ISC, http://www.isc.ac.uk/) is shown in Table 4.12. The epicenter is close to two settlements: Çalkara, northwest of the epicenter, and Atalan, southeastern of the epicenter. Ten seismic stations operated by AFAD captured this event, the details of the stations shown in Table 4.13.

Velocity time series of the event Mw 4.3 at stations 2602, 2611, 2615 have longer duration waveforms. Large amplitude S phase followed by some other phases as visible in NS component of 2611. Simple, short pulses reflecting source effects are observed at waveforms at 2610 and 2012 stations. Among stations, the highest PGV is observed at 2610 station in EW (0.03 cm/s) and UD direction (0.09 cm/s). Even though epicentral distance of 2601 (basin center) and 2610 (basin edge) stations are almost equal, 2610 station, have 2.5 to 5 times higher PGV values. The highest PGV appears after S arrival at one of the farthest station, 2615.

Table 4.12. Moment tensor solution of Eskişehir earthquake Mw 4.3 from the ISC.

Date-Time (UTC)	**Location**		**Mw**	**Depth**	**Mo**	**Strike (°)**	**Dip (°)**	**Rake (°)**
	Latitude	**longitude**		**(km)**	**(dyne*cm)**			
17.01.2015	40.09°	30.53°	4.3	10	3.04E+22	273	82	-86

Table 4.13. Features of AFAD stations and distance parameters for 17.01.2015 Mw 4.3 earthquake

Station	**Long. (°)**	**Lat. (°)**	**V_{S30} (m/s)**	**Location**	**R_{epi} (km)**	**R_{hyp} (km)**
2601	30.528	39.814	237	Center	30.69	32.27
2602	30.497	39.789	328	Center	33.58	35.04
2606	30.456	39.749	348	Edge	38.43	39.71
2610	30.422	39.822	289	Edge	31.18	32.75
2611	30.443	39.788	275	Center	34.39	35.81
2612	30.4017	39.771	—	Edge	37.11	38.43
2613	30.54	39.794	281	Center	32.92	34.41
2614	30.556	39.753	516	Edge	37.53	38.85
2615	30.652	39.74	307	Edge	40.28	41.51
2616	30.619	39.706	471	Edge	43.36	44.51

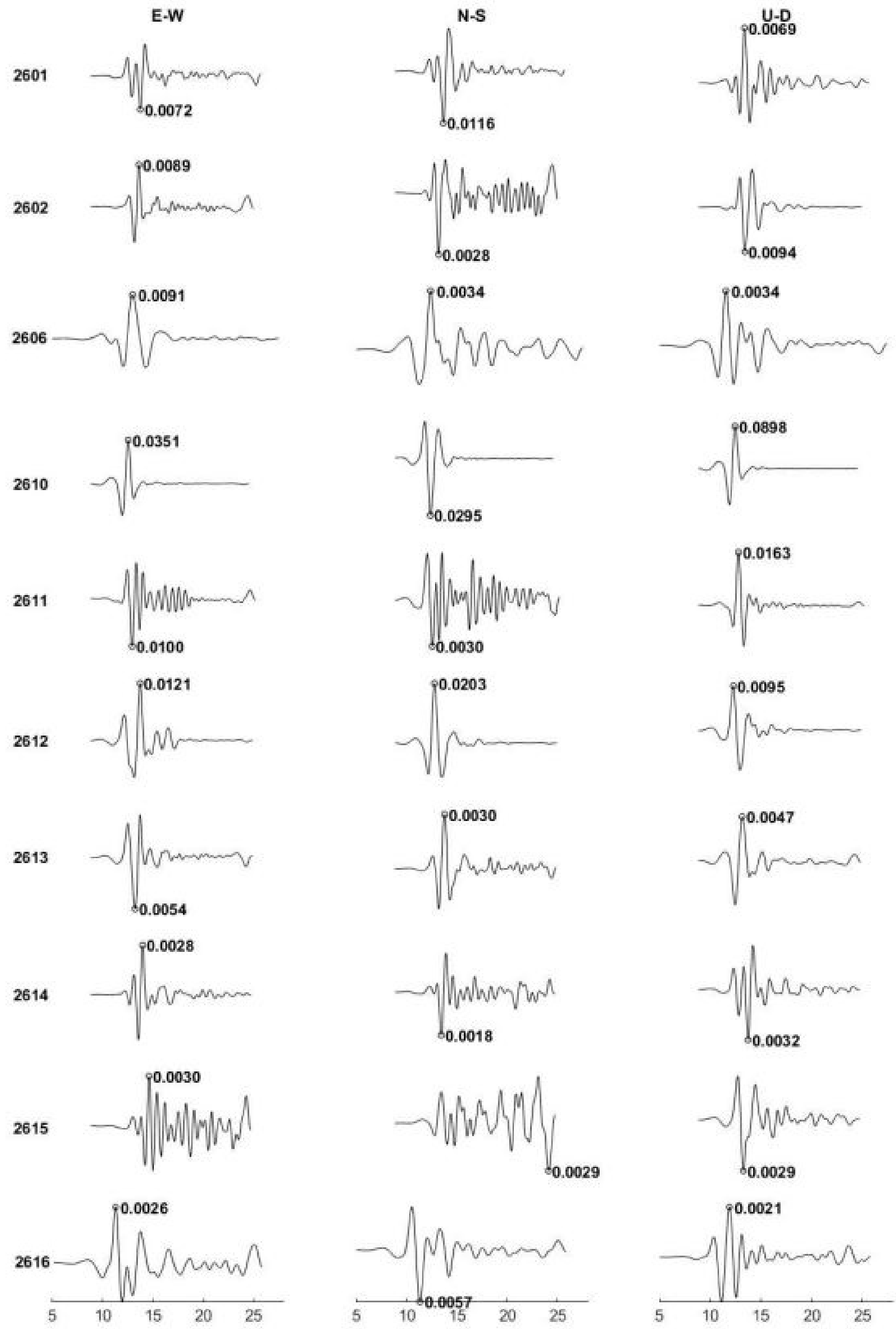

Figure 4.21. Velocity time series of the 17.01.2015 Mw 4.3 earthquake bandpass filtered at 0.3-1 Hz.

Apart from this, two earthquakes which are 18 Sept. 2015 Mw 3.7 and 24 Jul. 2020 Mw 4.1 happened inside of the basin. The details on these seismic motions are given, in the previous section and also below, which were announced by the Kandilli Observatory and Research Institute (KOERI) and AFAD. In addition, the velocity time series are filtered bandpass between the frequency ranges of 0.3 and 1 Hz, represented at Figure 4.22 and Figure 4.23. Filtered waveforms of the 3.7 event mostly show simple, short pulses due to source effects.The highest horizontal PGV is (0.11 cm/s) observed at 2610 station in NS direction, whereas highert vertical PGV (0.13cm/s) is observed at 2602 station. Regarding Mw.4.1 earthquake, since recorded ground motions are too short (about 9 s.) to evaluate the possible surface waves, they are not taken into account in the thesis.The location of three earthquakes, seismic stations, active fault surrounding Eskişehir and geological exploration fields are demonstrated in Figure 4.24.

Table 4.14. Moment tensor solution of Eskişehir earthquake Mw 3.7 from the KOERI.

Date-Time (UTC)	**Location**		**Mw**	**Depth (km)**	**Mo (dyne*cm)**	**Strike (°)**	**Dip (°)**	**Rake (°)**
	Latitude	**longitude**						
18.09.2015	39.81°	30.43°	3.7	7	4.28E+21	277	32	-65

Table 4.15. Features of AFAD stations and distance parameters for 18.09.2015 Mw 3.7 earthquake.

Station	**Long. (°)**	**Lat. (°)**	**V_{S30} (m/s)**	**Location**	**Repi (km)**	**Rhyp (km)**
2601	30.528	39.814	237	Center	6.67	9.67
2602	30.497	39.789	328	Center	4.64	8.40
2604	30.51	39.773	296	Center	6.57	9.60
2606	30.456	39.749	348	Edge	6.80	9.76
2610	30.422	39.822	289	Edge	2.73	7.52
2611	30.443	39.788	275	Center	2.51	7.44
2614	30.556	39.753	516	Edge	11.05	13.08
2615	30.652	39.74	307	Edge	18.93	20.19

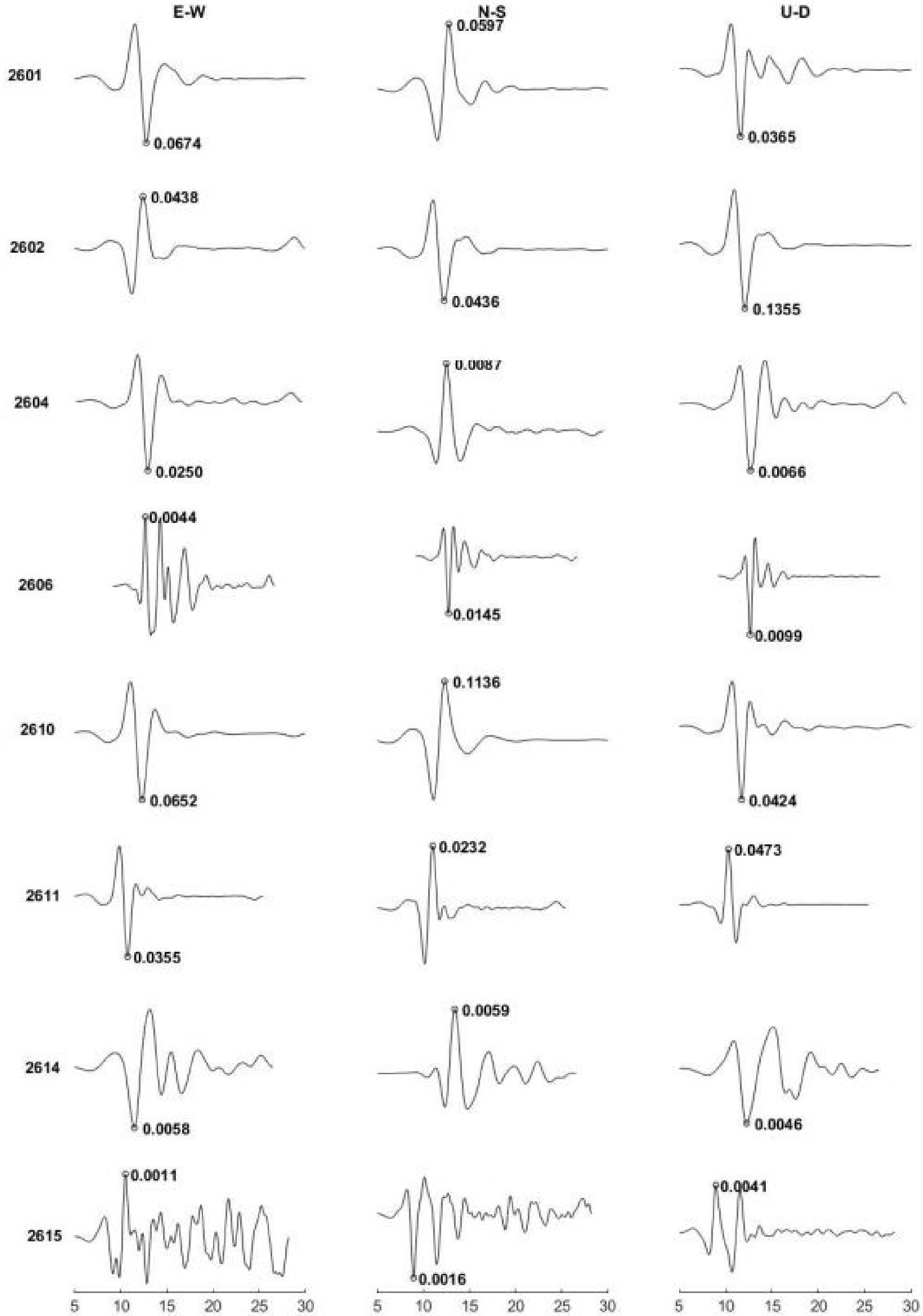

Figure 4.22. Velocity time series of the 18.09.2015 Mw 3.7 earthquake bandpass filtered at 0.3-1 Hz.

Table 4.16. Moment tensor solution of Eskişehir earthquake Mw 4.1 from the AFAD.

Date-Time (UTC)	Location		Mw	Depth (km)	Mo (dyne*cm)	Strike (°)	Dip (°)	Rake (°)
	Latitude	longitude						
24.07.2020	39.8478°	30.4398°	4.1	10.84	—	289	65	-111

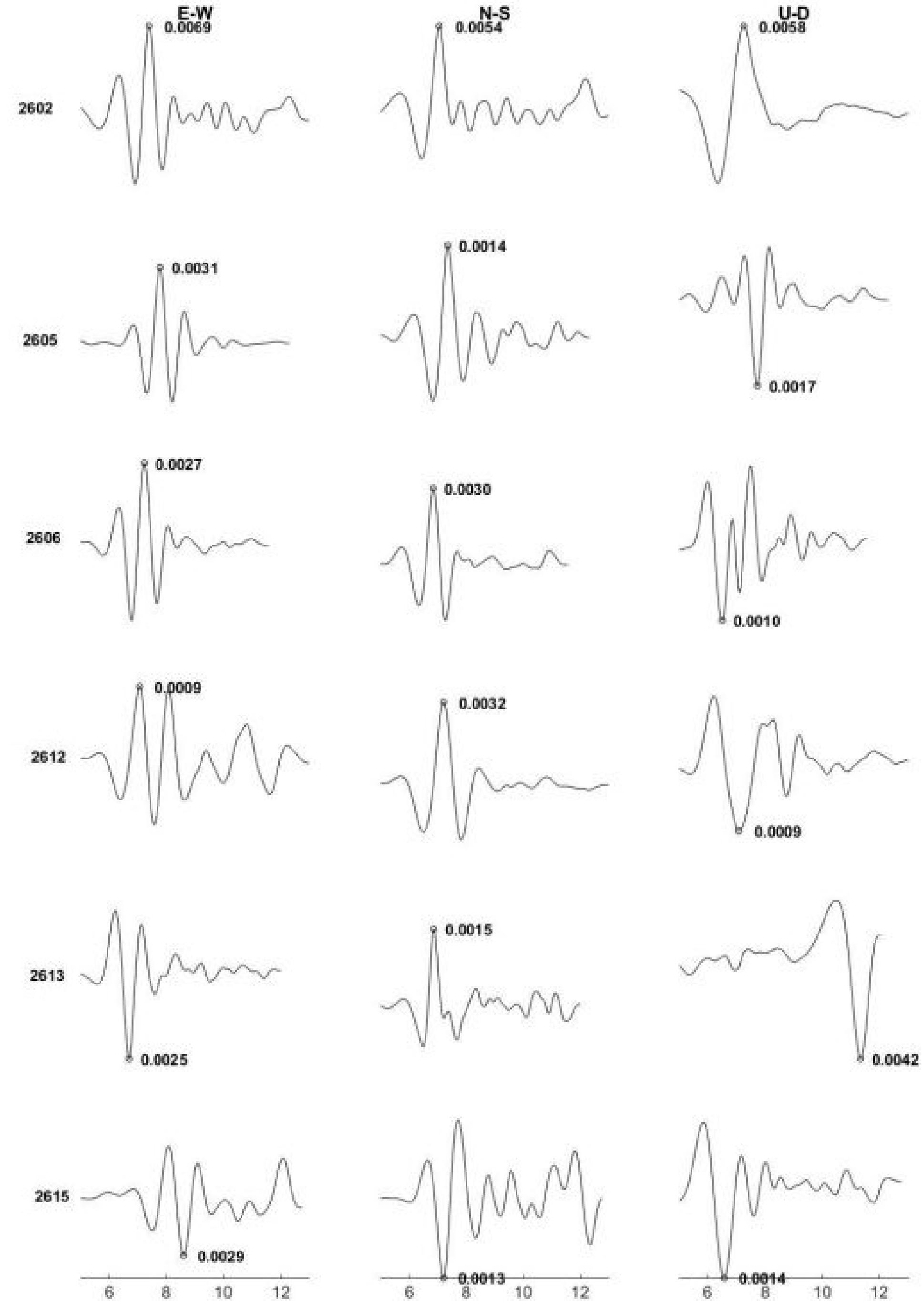

Figure 4.23. Velocity time series of the 24.07.2020 Mw 4.1 Earthquake bandpass filtered at 0.3-1 Hz.

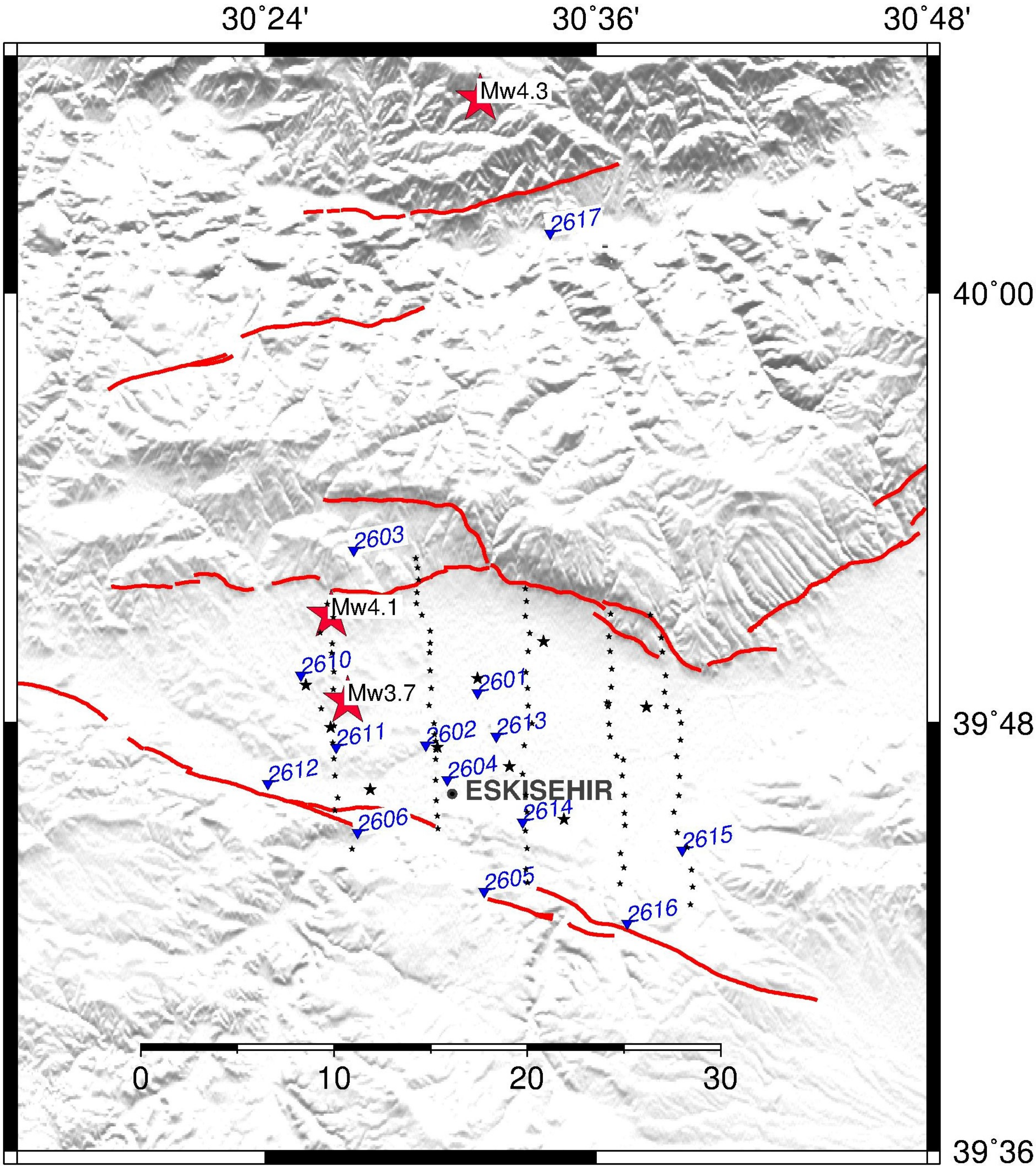

Figure 4.24. Demonstration of the epicenter of 3 earthquakes with red start, strong ground motions' stations with blue downward-pointing triangles, active faults surrounding Eskişehir with red lines, MAM (microtremor array measurements) single stations via black points and stars.

5. SIMULATION OF SEISMIC WAVES AT ESKİŞEHİR BASIN

5.1. Methodology (Finite Difference Method)

5.1.1. The Finite-Difference Method

There are many numerical methods to model seismic motion in heterogeneous media. However, the finite difference method is one of the most well-known numerical methods in seismology and robust ground motion modeling. Many seismologists also prefer it because of enough accuracy in representing the complex structure of The Earth's interior. The finite-difference method is known as the grid-point method. It covers a computational area with a space-time grid. All functions are defined by their values and grid point. This method provides a sufficiently accurate solution for modeling seismic wave propagation, seismic motion, and natural attenuation.

Furthermore, heterogeneity of the medium, including material discontinuities and gradients, can be provided by this numerical method. Moreover, numerical methods use the finite set of numbers stored in computer memory to represent a solution for the differential equation. It is also a valuable tool for users in terms of easy implementation (time) and usage of less computer memory.

5.1.2. The Finite-Difference Method using staggered grids with non-uniform spacing in 3D Elastic Media

Seismologists and engineers have widely used a simulation of strong ground motion in 3D elastic media using the finite-difference method at the frequency of interest. This numerical method offers the opportunity for researchers to generate synthetic waves in a short time utilizing non-uniform grid spacing compared to FD with uniform grid spacing. In this way, seismic waves can be synthesized without wasting vast computational resources because of the unnecessary over-sampling of complex earth structures.

The 3D elastic finite difference method using staggered grids with non-uniform spacing implemented in this study has been approved by Pitarka (1999). Pitarka (1999) has also compared modeling of seismic motion using this method with analytical solutions, conventional 3D staggered grid FD with uniform grid spacing, and reflectivity methods for various velocity models. He asserted that the synthetic motion generated by FD with non-uniform is very similar to others when the grid sampling rate is at least six grid points per shortest shear wavelength. This is known as the dispersion error criterion or sampling criterion Equation (5.1). To yield logical results, these criteria should be satisfied. The lowest velocity determines the grid spacing by considering the sampling criterion. In contrast, the time step is restricted by the highest velocity according to the stability conditions Equation (5.2).

$$f_{\max} \leq \frac{V_{s\min}}{6\ d_{\min}} \tag{5.1}$$

$$\varDelta_t \leq \frac{6}{7}\frac{h}{V_{\max}} \tag{5.2}$$

The non-uniform spacing enables researchers to apply this method to the large-scale structure by missing spatial oversampling in the field with high velocity. This technique offers small computer memory to the user by avoiding spatial oversampling via non-uniform spacing without utilizing supercomputer platforms.

5.1.3. Space-time Grids

The combination of space and time points defines the space-time grid. Grid coordinates show us location x, y, and z. it declares spatial information for specific grid points. A space-time grid can be constructed if time is taken into domain variables.

There are many types of the grid systems, such as conventional grid, collocated grid, partly-staggered grid, and staggered grid. Staggered grids were used for Finite Difference Schemes. Each particle velocity component and shear stress component are located in different grid positions, while all normal stress-tensor components are situated in another grid position. Some velocity and stress components are shifted from the location of other components by half grid space in Finite Difference Schemes (Pitarka, 1999), as shown in the Figure 5.1.

Another point is that the grid spacing is nonuniform, meaning grid space changes from point to point, Figure 5.1(b). This supplies users with computational efficiency. Remarkably, the nonuniform spacing technique avoids the spatial oversampling issue triggered by the uniform spacing approach.

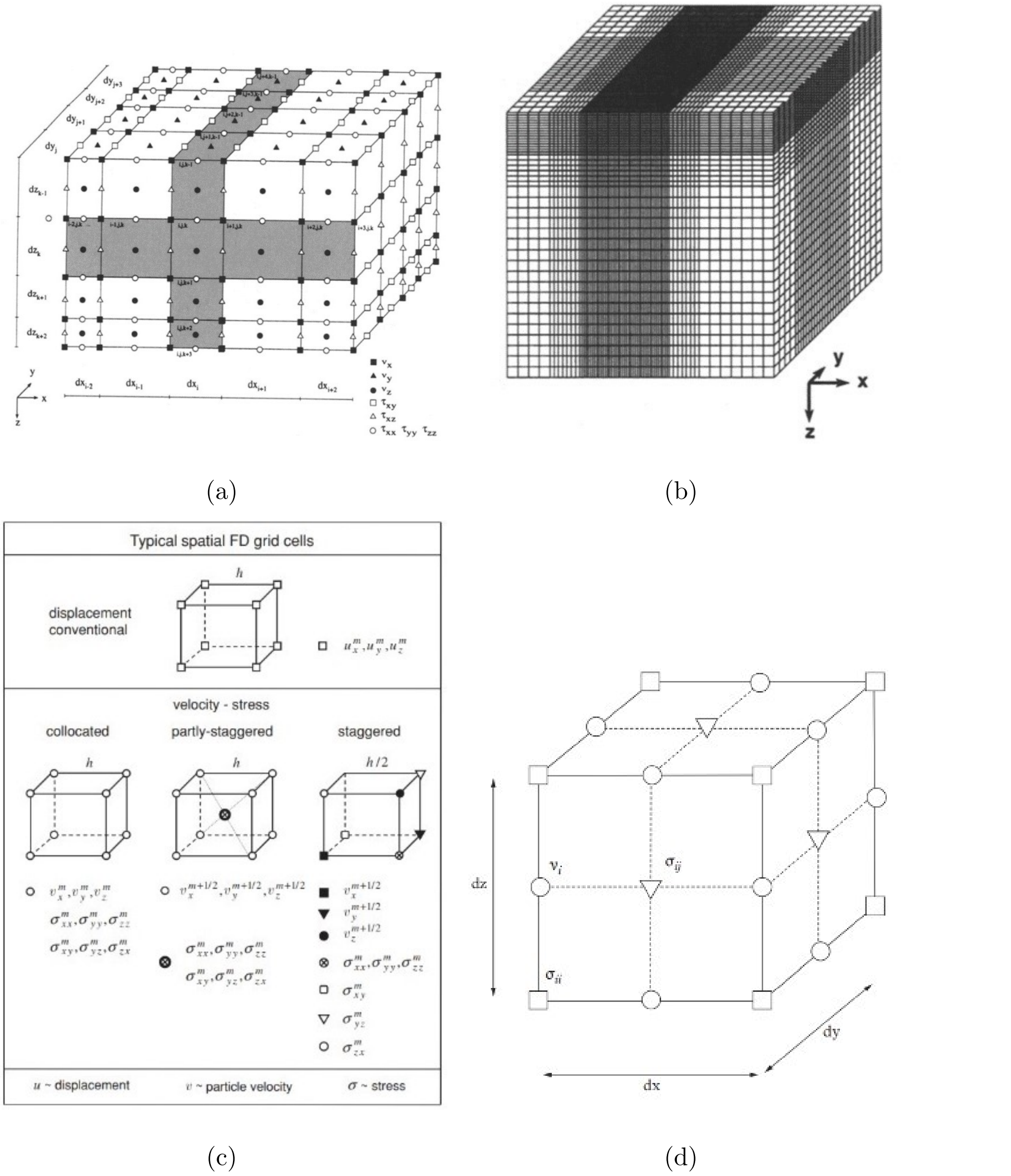

Figure 5.1. Illustration of finite difference schemes. (a) shows the finite difference schemes and (b) indicates the nonuniform spacing both of them acquired from Pitarka (1999). (c) and (d) also demonstrate the the grid cell in FD method obtained from Igel (2017) and Moczo et al. (2014) respectively.

5.1.4. Equations of Motion

The wave propagation is explained by the following equations in 3D, linear, and isotropic elastic media.

Equation of momentum conservation:

$$\begin{aligned} \rho\partial_{tt}u_x &= \partial_x\tau_{xx} + \partial_y\tau_{xy} + \partial_z\tau_{xz} + f_x \\ \rho\partial_{tt}u_y &= \partial_x\tau_{xy} + \partial_y\tau_{yy} + \partial_z\tau_{yz} + f_y \\ \rho\partial_{tt}u_z &= \partial_x\tau_{xz} + \partial_y\tau_{yz} + \partial_z\tau_{zz} + f_z \end{aligned} \tag{5.3}$$

Stress-strain relationships:

$$\begin{aligned} \tau_{xx} &= (\lambda + 2\mu)\partial_x u_x + \lambda\left(\partial_y u_y + \partial_z u_z\right) \\ \tau_{yy} &= (\lambda + 2\mu)\partial_y u_y + \lambda\left(\partial_x u_x + \partial_z u_z\right) \\ \tau_{zz} &= (\lambda + 2\mu)\partial_z u_z + \lambda\left(\partial_x u_x + \partial_y u_y\right) \\ \tau_{xy} &= \mu\left(\partial_y u_x + \partial_x u_y\right) \\ \tau_{xz} &= \mu\left(\partial_z u_x + \partial_x u_z\right) \\ \tau_{yz} &= \mu\left(\partial_z u_y + \partial_y u_z\right) \end{aligned} \tag{5.4}$$

In these equations, u,τ and f represent the displacement, the stress, and the body-force components respectively. The ρ is the density. The Lamé coefficients are μ,and λ. ∂ is the symbol of the differential with respect to the time(t). When the second derivative of displacement is considered as the first derivative of the velocity by the time. Also, when ρ is replaced with $1/b$, Equation (5.3) can be written as the below form;

$$\rho\partial_{\mathrm{t}} v_x = b\left(\partial_x \tau_{xx} + \partial_y \tau_{xy} + \partial_z \tau_{xz} + f_x\right)$$
$$\rho\partial_{\mathrm{t}} v_y = b\left(\partial_x \tau_{xy} + \partial_y \tau_{yy} + \partial_z \tau_{yz} + f_y\right) \tag{5.5}$$
$$\rho\partial_{\mathrm{t}} v_z = b\left(\partial_x \tau_{xz} + \partial_y \tau_{yz} + \partial_z \tau_{zz} + f_z\right)$$

where b is the buoyancy $(1/\rho)$.

The first derivative of the Equation (5.5) is formulated as below,

$$\partial_{\mathrm{t}} \tau_{\mathrm{xx}} = (\lambda + 2\mu)\partial_x v_z + \lambda\left(\partial_y v_y + \partial_z v_z\right)$$
$$\partial_{\mathrm{t}} \tau_{\mathrm{yy}} = (\lambda + 2\mu)\partial_y v_y + \lambda\left(\partial_x v_x + \partial_z v_z\right)$$
$$\partial_{\mathrm{t}} \tau_{\mathrm{zz}} = (\lambda + 2\mu)\partial_z v_z + \lambda\left(\partial_x v_x + \partial_y v_y\right)$$
$$\partial_{\mathrm{t}} \tau_{\mathrm{xy}} = \mu\left(\partial_y v_x + \partial_x v_y\right) \tag{5.6}$$
$$\partial_{\mathrm{t}} \tau_{\mathrm{xz}} = \mu\left(\partial_z v_x + \partial_x v_z\right)$$
$$\partial_{\mathrm{t}} \tau_{\mathrm{yz}} = \mu\left(\partial_z v_y + \partial_y v_z\right)$$

5.1.5. Application Equations of Motion to Finite-Difference

The equations (5.5) and (5.6) can be solved via the Finite-Difference method. Figure shows us not only spatial variable but also temporal variables in the staggered schemes. In the type of this grid system enables to define the various difference operators at the center of the same space-time point. Thus, implementation scheme is very efficient and brief.

The discrete form of equations:

For the velocities,

$$v_{x\ i+\frac{1}{2},j,k}^{n+1/2} = v_{xi+\frac{1}{2},j,k}^{n-1/2} + \left[\Delta t \underline{b}_x \left(D_x \tau_{xx} + D_y \tau_{xy} + D_z \tau_{xz} + f_x\right]\right|_{i+\frac{1}{2},j,k}^{n}$$
$$v_{y\ i,j+\frac{1}{2},k}^{n+1/2} = v_{xi,j+\frac{1}{2},k}^{n-1/2} + \left[\Delta t \underline{b}_y \left(D_x \tau_{xy} + D_y \tau_{yy} + D_z \tau_{yz} + f_y\right]\right|_{i,j+\frac{1}{2},k}^{n} \tag{5.7}$$
$$v_{z\ i,j,k+\frac{1}{2}}^{n+1/2} = v_{xi,j,k+\frac{1}{2}}^{n-1/2} + \left[\Delta t \underline{b}_z \left(D_x \tau_{xz} + D_y \tau_{yz} + D_z \tau_{zz} + f_z\right]\right|_{i,j,k+\frac{1}{2}}^{n}$$

For the stresses:

Normal stresses,

$$
\begin{aligned}
\tau^{n+1}_{xx\ i,j,k} &= \tau^{n}_{xxi,j,k} + \Delta t \left[(\lambda + 2\mu) D_x v_x + \lambda \left(D_y v_y + D_z v_z\right)\right]\Big|^{n+1/2}_{i,j,k} \\
\tau^{n+1}_{yy\ i,j,k} &= \tau^{n}_{yy\quad i,j,k} + \Delta t \left[(\lambda + 2\mu) D_y v_y + \lambda \left(D_x v_x + D_z v_z\right)\right]\Big|^{n+1/2}_{i,j,k} \\
\tau^{n+1}_{zz\ i,j,k} &= \tau^{n}_{zzi,j,k} + \Delta t \left[(\lambda + 2\mu) D_z v_z + \lambda \left(D_x v_x + D_y v_y\right)\right]\Big|^{n+1/2}_{i,j,k}
\end{aligned}
\tag{5.8}
$$

Shear Stresses,

$$
\begin{aligned}
\tau^{n+1}_{xy\ i+\frac{1}{2},j+\frac{1}{2},k} &= \tau^{n}_{xy\ i+\frac{1}{2},j+\frac{1}{2},k} + \Delta t \left[\bar{\mu}^{H}_{xy} \left(D_y v_z + D_x v_y\right)\right]\Big|^{n+1/2}_{i+\frac{1}{2},j++\frac{1}{2},k} \\
\tau^{n+1}_{xz\ i+\frac{1}{2},j,k+1/2} &= \tau^{n}_{xzi+\frac{1}{2},j,k+\frac{1}{2}} + \Delta t \left[\bar{\mu}^{H}_{xz} \left(D_z v_x + D_x v_x\right)\right]\Big|^{n+1/2}_{i+\frac{1}{2},j,k+\frac{1}{2}} \\
\tau^{n+1}_{yz\ i,j+\frac{1}{2},k+\frac{1}{2}} &= \tau^{n}_{yzi,j+\frac{1}{2},k+\frac{1}{2}} + \Delta t \left[\bar{\mu}^{H}_{yz} \left(D_x v_y + D_y v_z\right)\right]\Big|^{n+1/2}_{i,j+\frac{1}{2},k+\frac{1}{2}}
\end{aligned}
\tag{5.9}
$$

5.2. Simulation & Comparison of Synthetic Waves with Recorded Seismic Events (17.01.2015 Mw 4.3 and 18.09.2015 Mw 3.7 earthquakes)

As a first step in validation of the velocity structure models, we have analyzed two observed ground motions, 17.01.2015 Mw 4.3 and 18.09.2015 Mw 3.7, and compared the synthetic and observed velocity seismograms about ten seismic stations in the frequency ranges of 0.3 to 1 and 0.3 to 0.6 Hz. Two frequency ranges were selected to evaluate the best fitting frequency ranges. We have concentrated on two velocity models in simulation: the Mindevalli velocity model with flat layers and the Mindavelli velocity model with basin, as mentioned in previous chapter. The velocity models are also described in Figure 3.16.

The simulation was carried out by following the finite difference method of Pitarka (1999) using staggered grids with nonuniform spacing in 3D Elastic Media. The total duration of the synthetic waves is 35 s for two candidate events.

Furthermore, the criteria are inherent in the finite difference technique, which should be satisfied for acquiring logical results in generating synthetic waves, such as sampling criterion and stability condition. While the minimum shear wave velocity controls the sampling criterion, the stability condition is driven by the maximum shear wave velocity. These parameters and the grid increments were taken into account to assess the frequency range in producing seismic motion. We have adjusted the grid spacing in the simulation by considering minimum S-wave velocity to determine the maximum frequency and computational time. The maximum frequency is the minimum S-wave velocity divided by six times the minimum grid spacing. Although the minimum grid spacing of 100 m enables us to calculate the wave field up to a frequency of 2.1 Hz, the high cut-off frequency is regarded as 1 Hz.

As for the comparison of seismograms, the goodness of fit factors mentioned by Pitarka et al. (2004) was calculated to grade simulation results by f_1 and f_2 terms quantitatively by Equation (5.10-5.11). Thus, the accuracy of the velocity structure has been questioned by the analyses of the goodness of fit. The former is familiar with the comparison between PGV_{obs} and PGV_{synt}. The latter is evaluated by integrating recorded and synthetic velocity seismograms in the time domain. Therefore, the f_2 term is more sensitive to the waveform, whereas the f_1 factor is susceptible to the amplitude. These factors vary from 1 to 0. If f_1 is equal to 1, the amplitude of the synthetic wave and observed waves are very close to each other. If f_2 is 1, the generated waveform are perfectly matched the recorded wave.

$$f_1 = \exp\left[-\left(\frac{PGV_{syn} - PGV_{obs}}{\min\left(PGV_{syn}, PGV_{obs}\right)}\right)^2\right] \tag{5.10}$$

$$f_2 = 2\left[\frac{\int obs(t).\,\mathrm{syn}(t)dt}{\int obs(t)^2dt + \int \mathrm{syn}(t)^2dt}\right] \tag{5.11}$$

Apart from these, the quality and quantity of the recordings plays a prominent role in validation of the velocity structure model in terms of comparison of the synthetic with observed data in the low frequency range.

In addition, another step in the simulation of seismic waves is the source model. The earthquake model was regarded as the point source model. The source parameters affect the amplitude, frequency content, and duration of motions. The orientation of fault and depth distinctly influence the horizontal components of the signals. The focal mechanism and the coordinate of these events were obtained from ISC and KOERI. The source parameters of both events used in simulation were described in Table 5.1.

Table 5.1. Source parameters.

Seismic Event Date	**Mw**	**Strike (°)**	**Dip (°)**	**Rake (°)**	**Depth (km)**	**Rise Time (s)**	**Mo (dyne*cm)**
17.01.2015	4.3	273	82	-86	10	0.2	3.04*10ˆ22
18.09.2015	3.7	277	32	-65	7	0.1	4.28*10ˆ21

Taking everything into consideration, there have challenges in the representation of realistic site effects. Maufroy et al. (2015) asserted that the differences between estimated and actual ground motion may originated from basin geometry, source parameters as well as uncertainties in the geological medium.

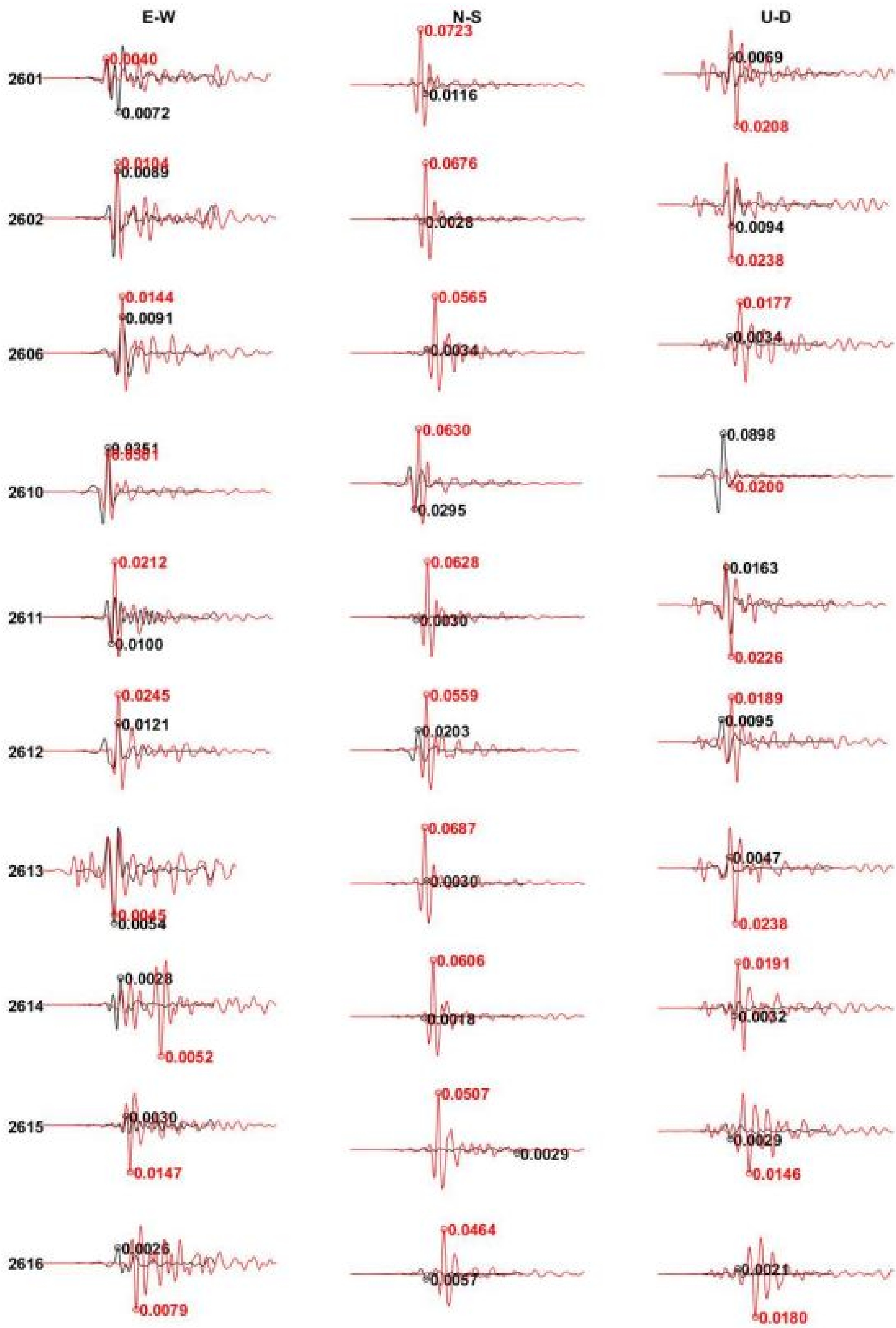

Figure 5.2. Comparison between the velocity time series (cm/s) of 1. model (with flat layer on top of the structure) and 17.01.2015 Mw 4.3 earthquake bandpass filtered at 0.3-1 Hz.

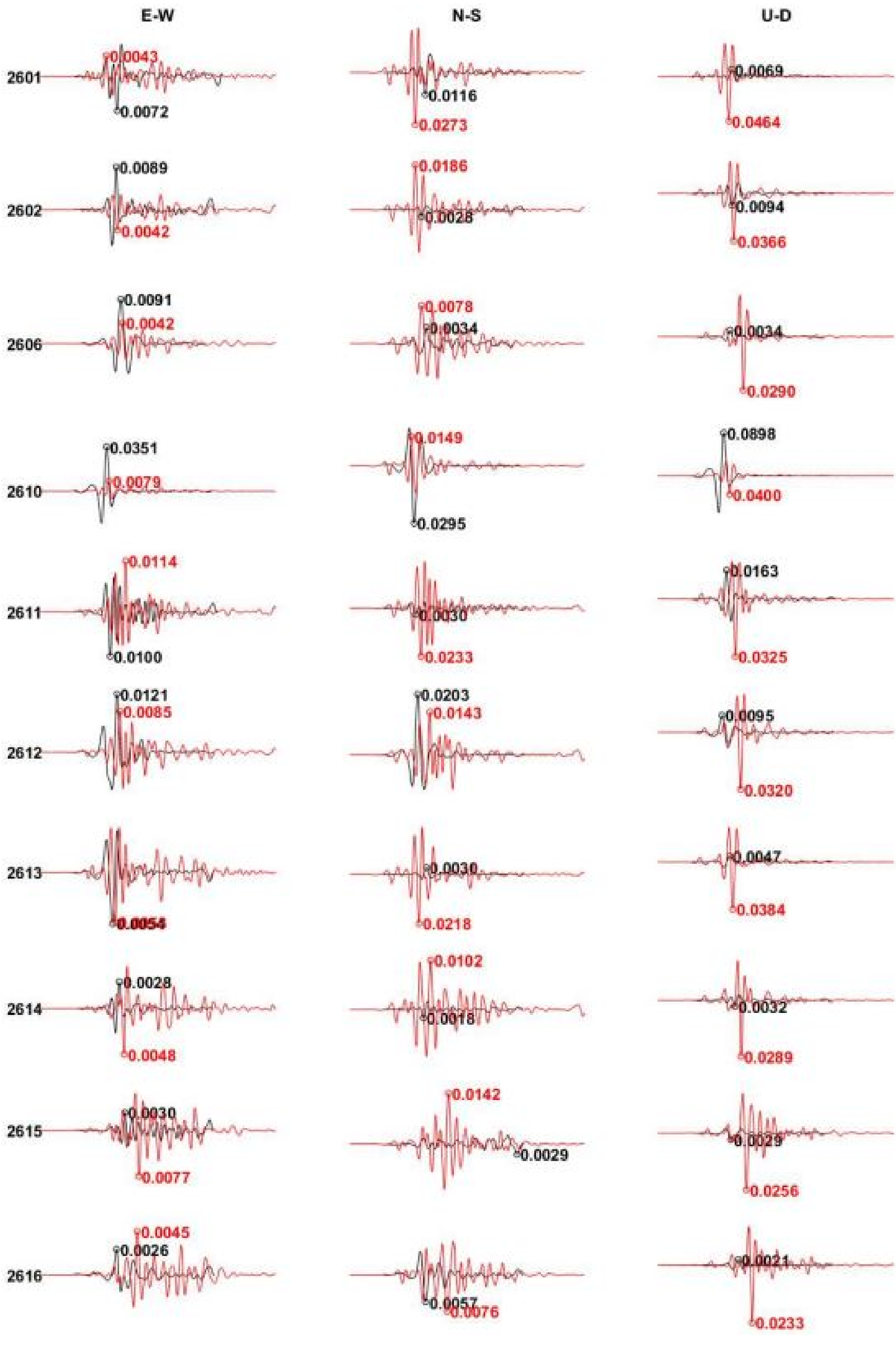

Figure 5.3. Comparison between the velocity time series (cm/s) of 2. model (added the basin geometry top of the substructure) and 17.01.2015 Mw 4.3 earthquake bandpass filtered at 0.3-1 Hz.

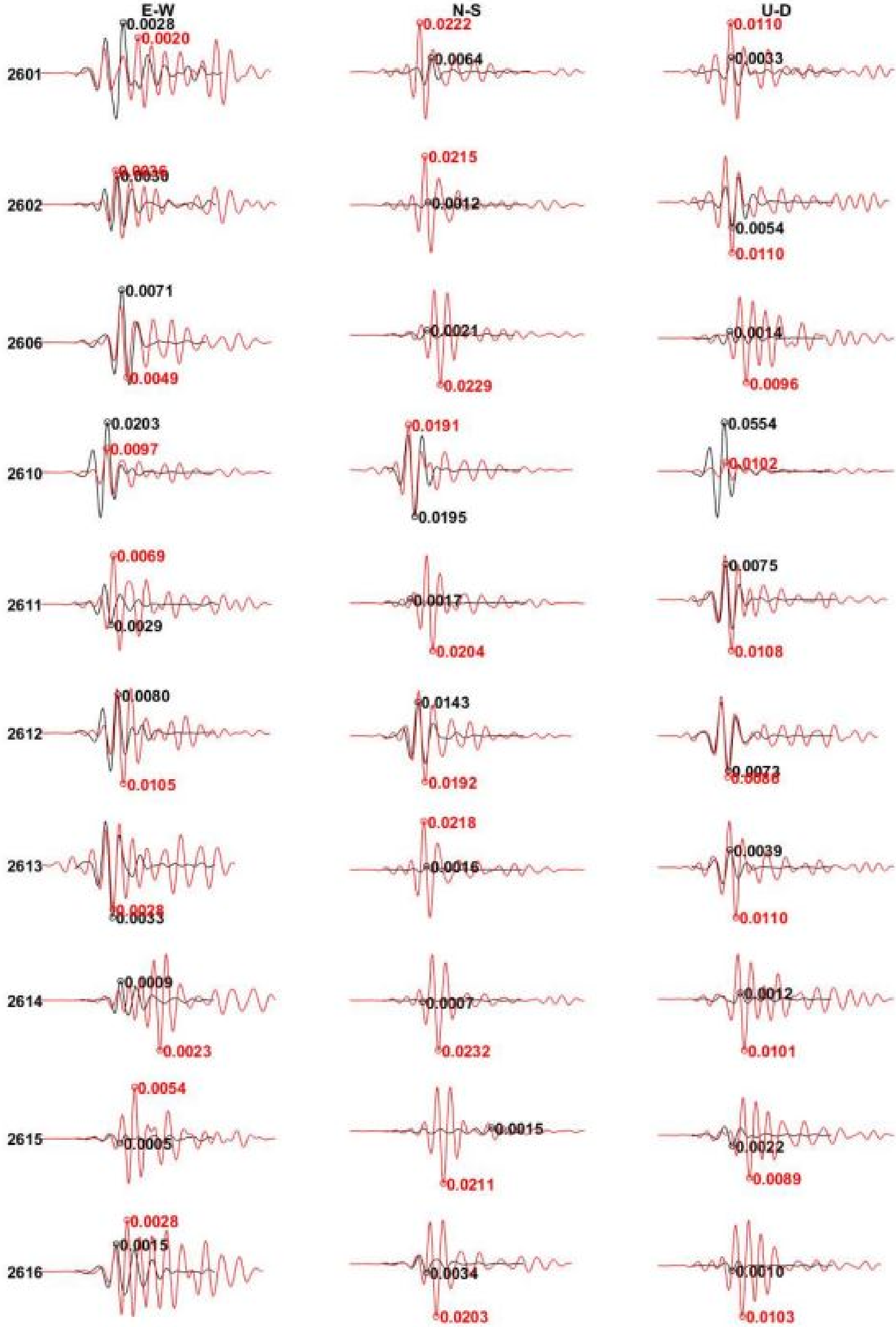

Figure 5.4. Comparison between the velocity time series (cm/s) of 1. model (with flat layer on top of the structure) and 17.01.2015 Mw 4.3 earthquake bandpass filtered at 0.3-0.6 Hz.

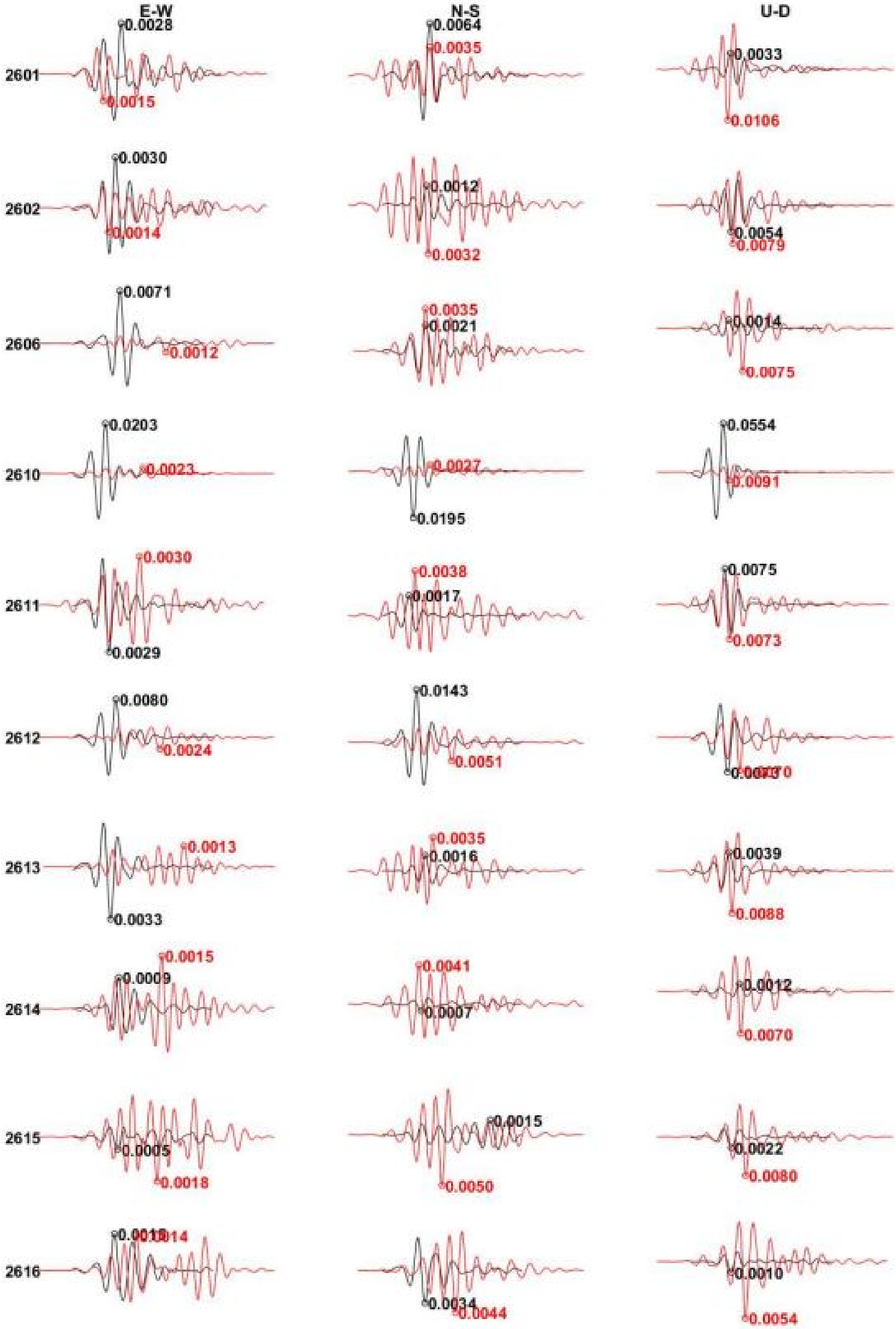

Figure 5.5. Comparison between the velocity time series (cm/s) of 2. model (added the basin geometry top of the substructure) and 17.01.2015 Mw 4.3 earthquake bandpass filtered at 0.3-0.6 Hz.

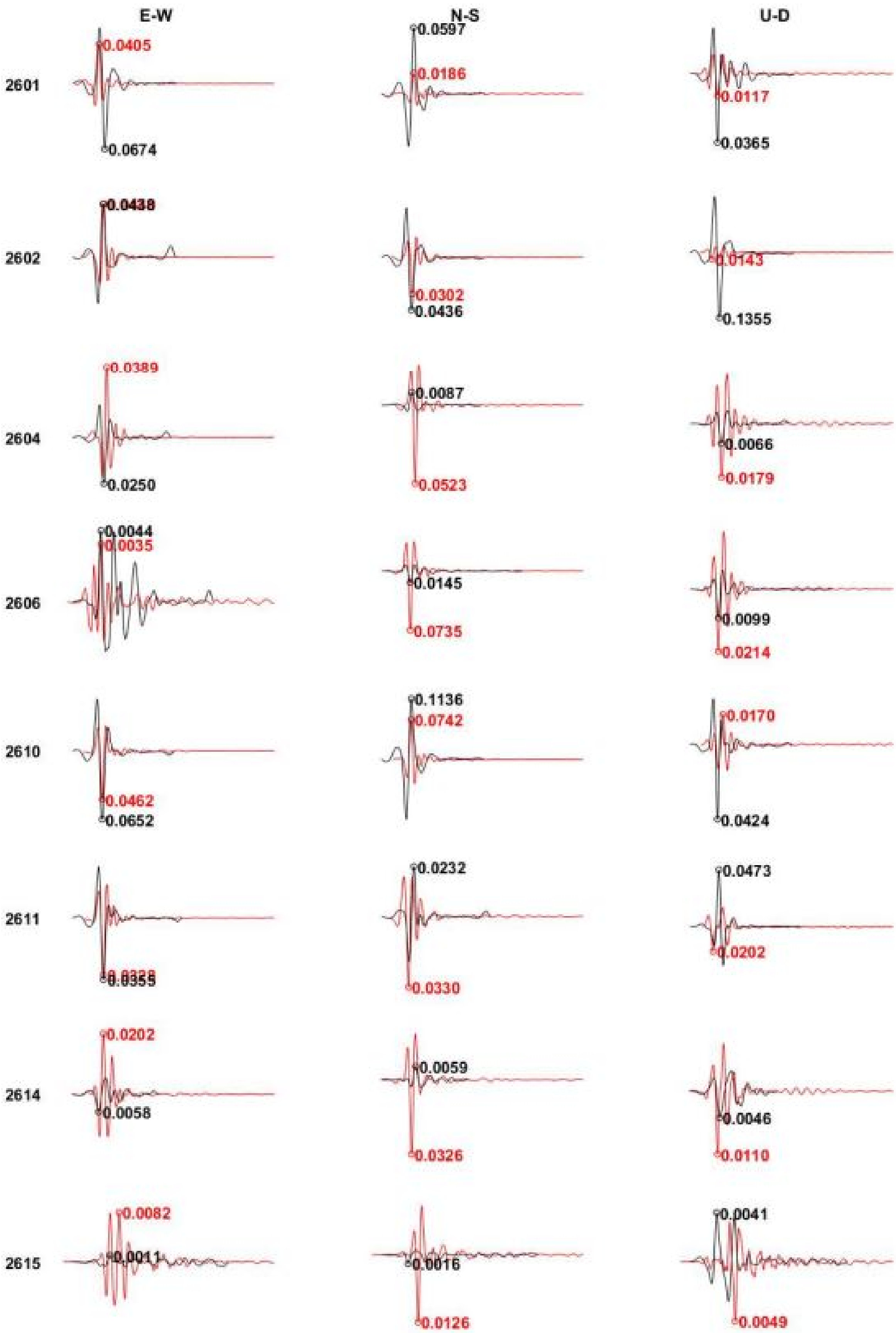

Figure 5.6. Comparison between the velocity time series (cm/s) of 1. model (with flat layer on top of the structure) and 18.09.2015 Mw 3.7 earthquake bandpass filtered at 0.3-1 Hz.

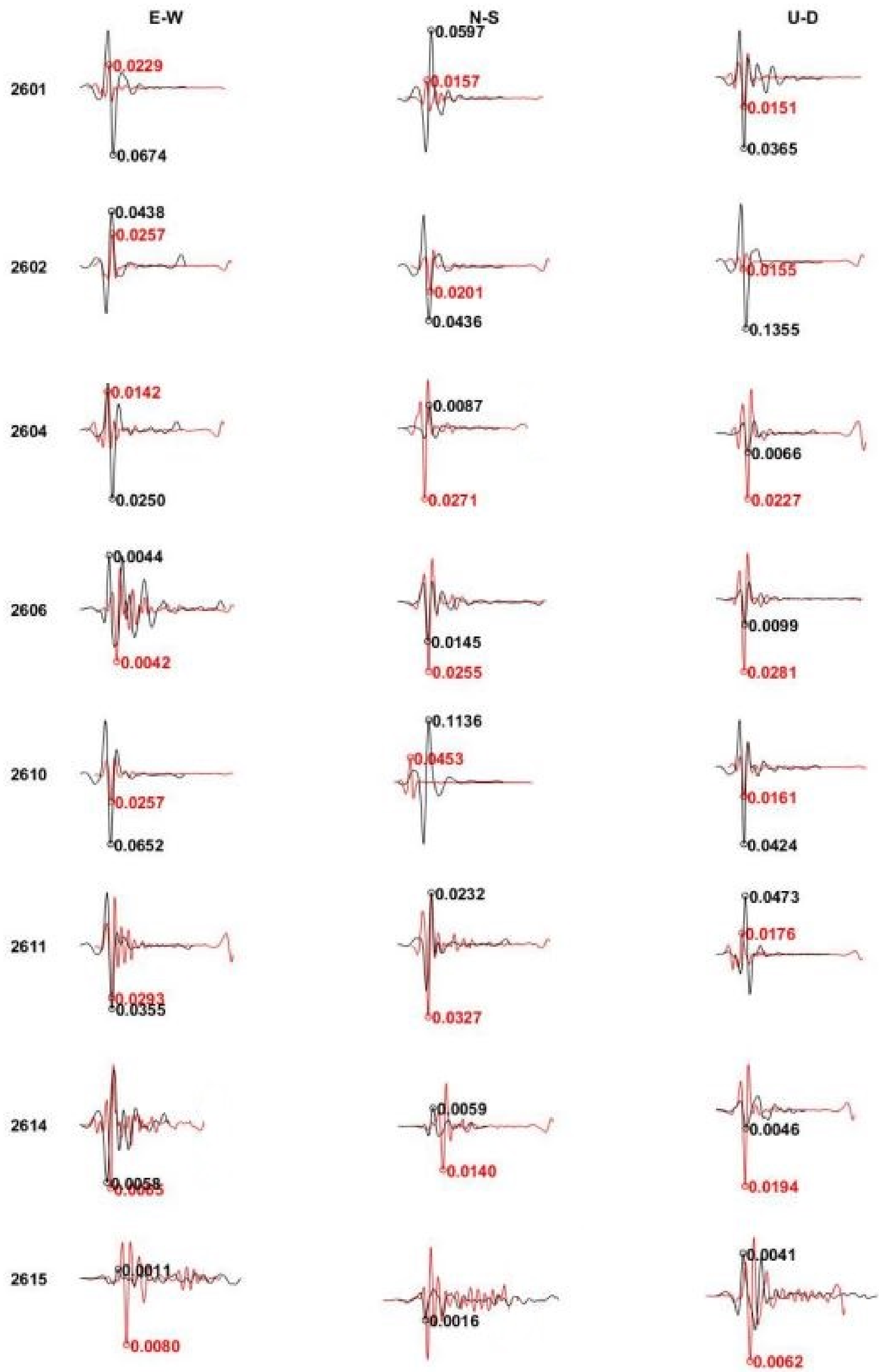

Figure 5.7. Comparison between the velocity time series (cm/s) of 2. model (added the basin geometry top of the substructure) and 18.09.2015 Mw 3.7 earthquake bandpass filtered at 0.3-1 Hz.

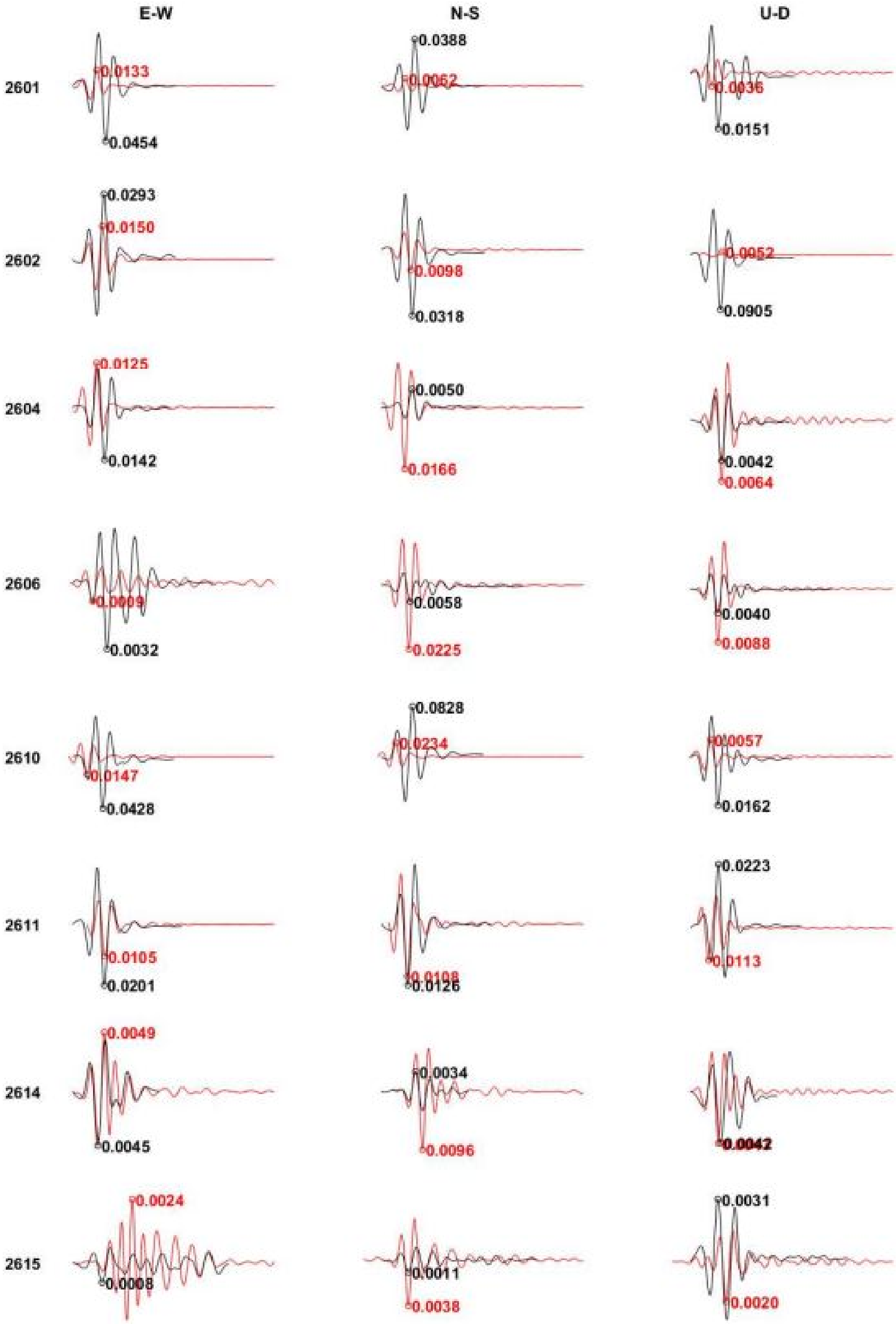

Figure 5.8. Comparison between the velocity time series (cm/s) of 1. model (with flat layer on top of the structure) and 18.09.2015 Mw 3.7 earthquake bandpass filtered at 0.3-0.6 Hz.

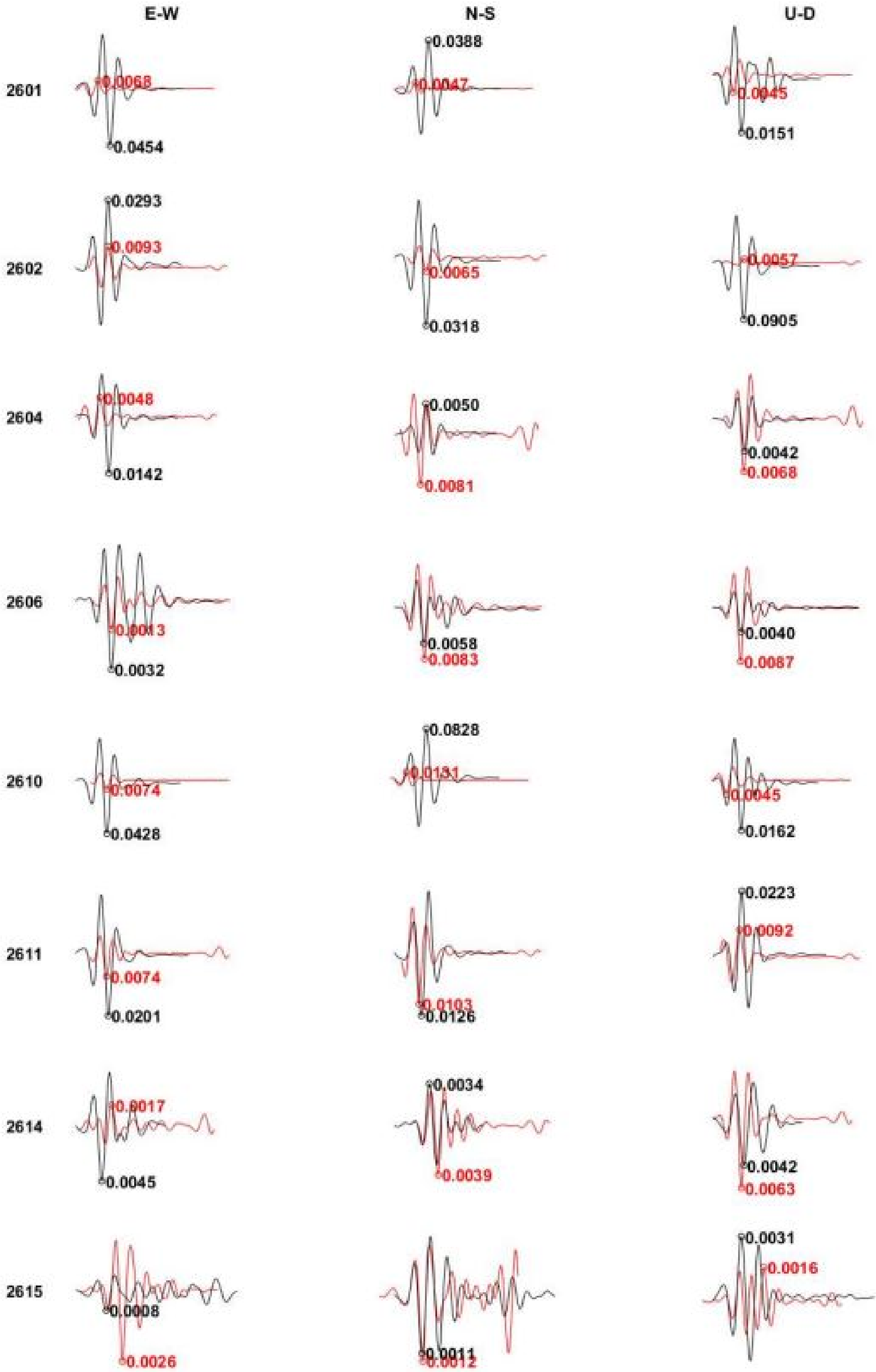

Figure 5.9. Comparison between the velocity time series (cm/s) of 2. model (added the basin geometry top of the substructure) and 18.09.2015 Mw 3.7 earthquake bandpass filtered at 0.3-0.6 Hz.

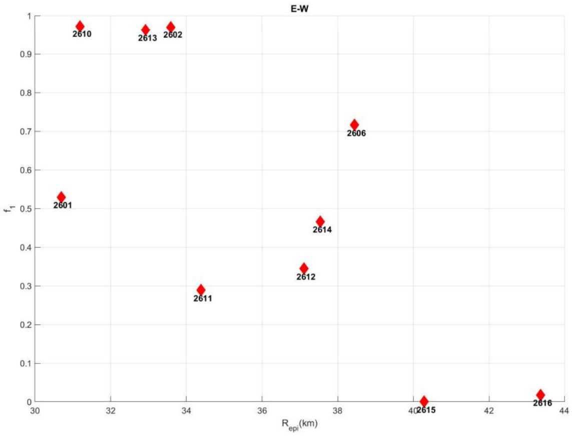

(a)

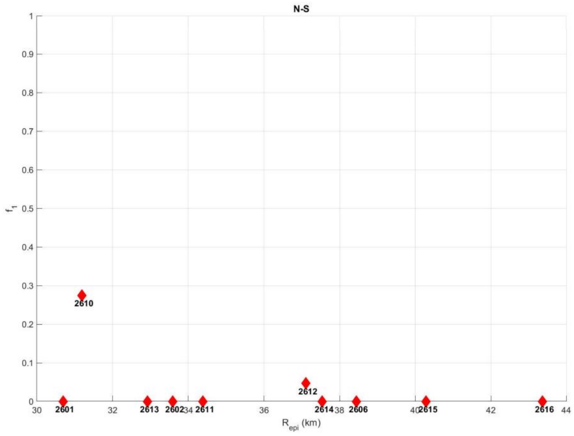

(b)

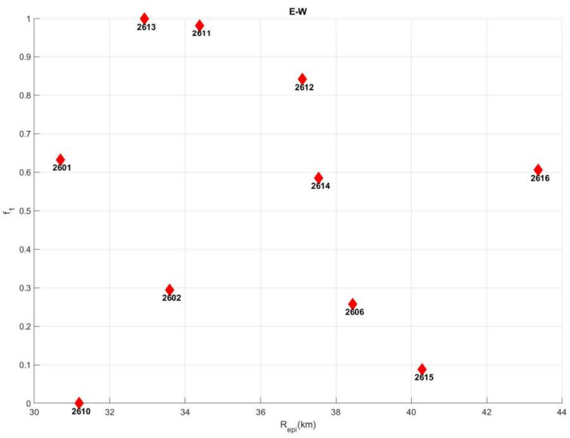

(c)

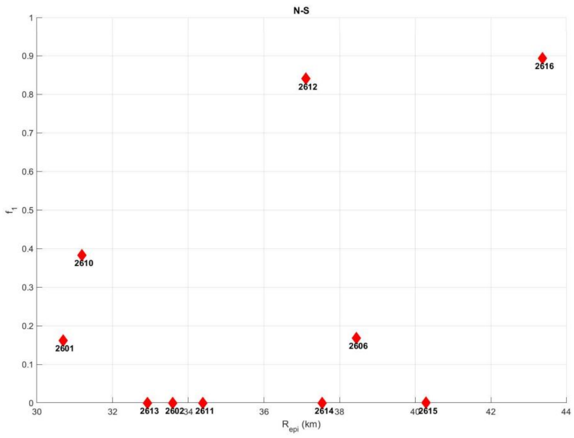

(d)

Figure 5.10. f_1 factor for 17.01.2015 Mw 4.3 using velocity model with basin (a) and (b), without basin (c) and (d) at frequency ranges of 0.3 and 1 Hz.

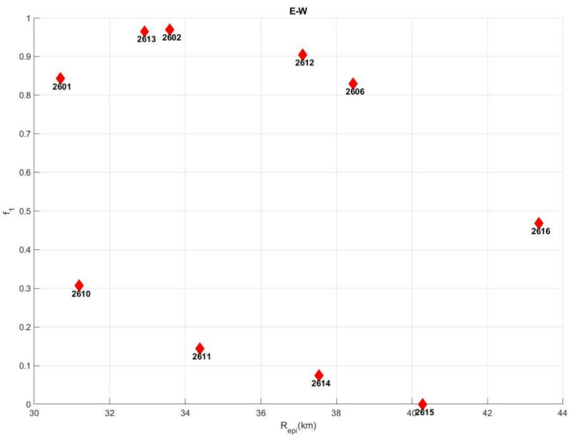

(a)

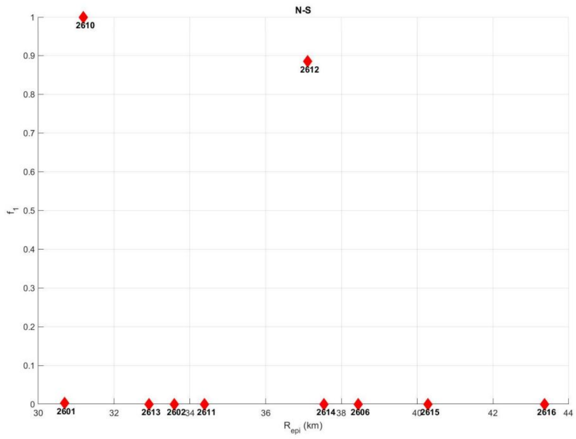

(b)

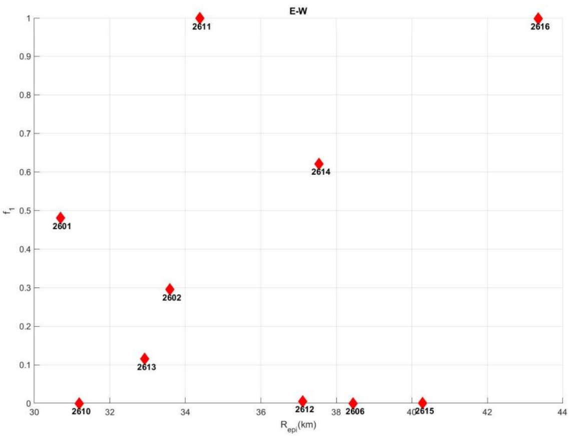

(c)

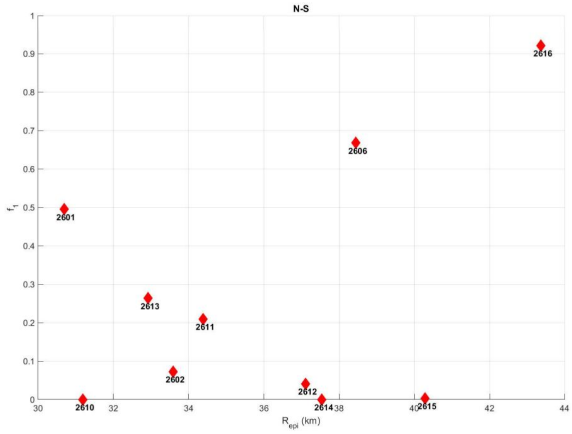

(d)

Figure 5.11. f_1 factor for 17.01.2015 Mw 4.3 using velocity model with (a) and (b), without basin (c) and (d) at frequency ranges of 0.3 and 0.6 Hz.

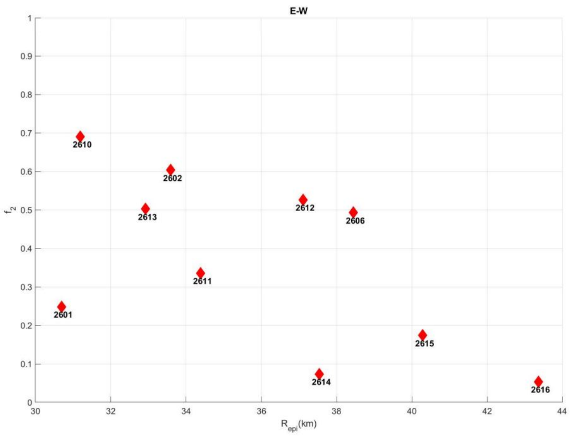

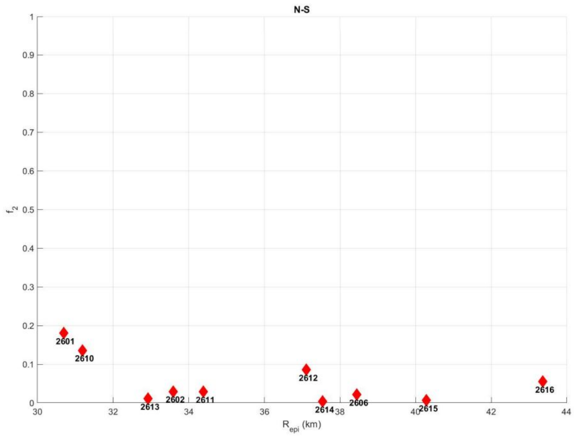

(a) (b)

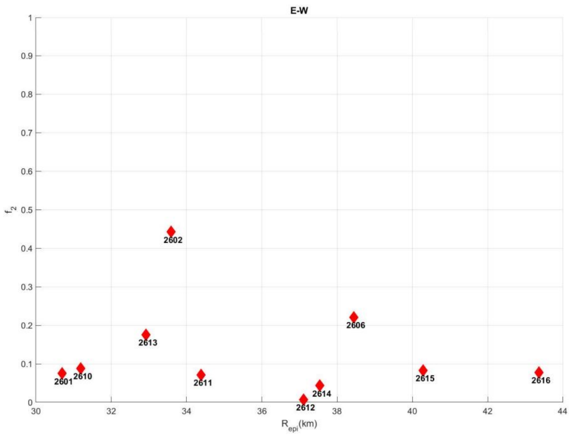

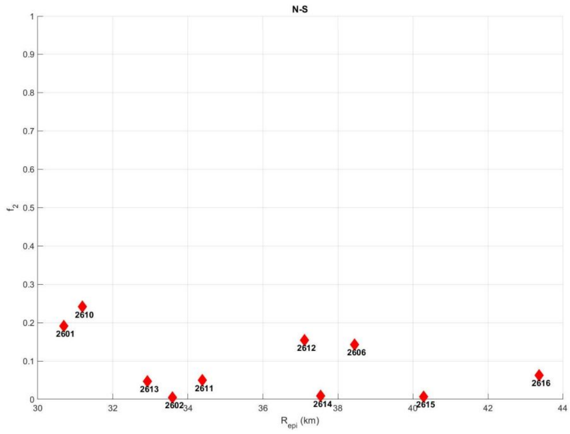

(c) (d)

Figure 5.12. f_2 factor for 17.01.2015 Mw 4.3 using velocity model with basin (a) and (b), without basin (c) and (d) at frequency ranges of 0.3 and 1 Hz.

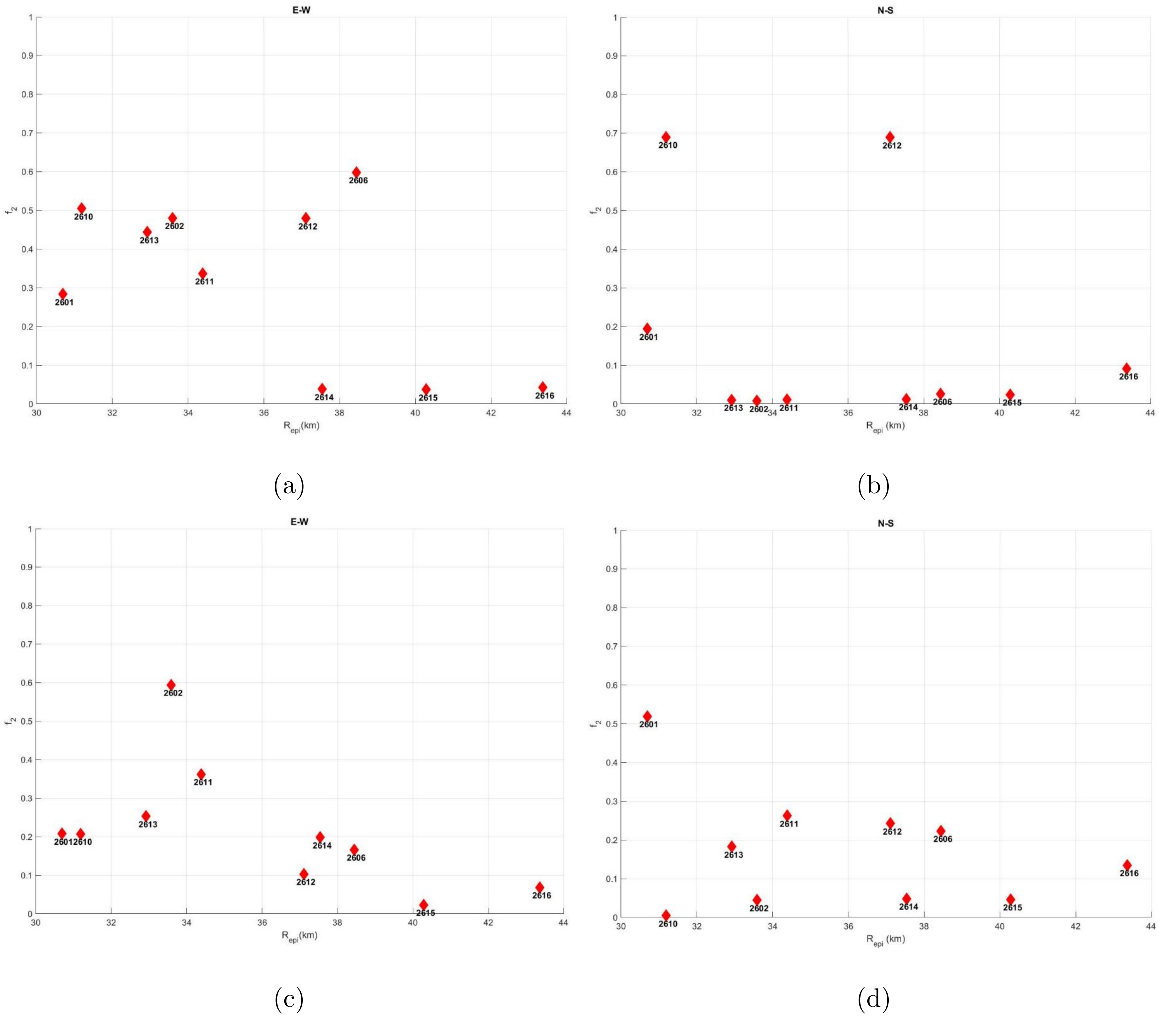

Figure 5.13. f_2 factor for 17.01.2015 Mw 4.3 using velocity model with basin (a) and (b), without basin (c) and (d) at frequency ranges of 0.3 and 0.6 Hz.

The compatibility and mismatch of the synthetic velocity time series with the actual time series were calculated numerically by employing the fit factors in two distinct frequency ranges for the two velocity structure models, as shown in the figure 5.10, 5.11, 5.12 and 5.13.

The results show that the amplitude harmony of generated waves in frequencies of 0.3 and 1 Hz using velocity model without basin generally agrees with the observed 17.01.2015 Mw 4.3 earthquake, but not 2615 and 2616 stations in the E-W direction. Moreover, producing waves utilizing the velocity model with basin improved harmonization of amplitude with observed seismograms except for 2610, 2602, and 2606 in the E-W direction. As for the N-S direction, there is good matching solely two stations for velocity model with basin, the 2612 and 2616 stations. The compatibility in phase, f_2 factor, is good in the E-W direction for the model without a basin compared to another model with a basin. On the contrary, the basin model usually increases the compatibility in phase and amplitude for the N-S direction, but not 2610 station.

On the other hand, synthetic waves of 2601, 2602, 2606, 2612, and 2613 stations using the velocity model without basin perfectly fit the f_1 factor for the E-W direction at frequency ranges of 0.3 and 0.6 Hz. The agreement between produced and recorded waves is not worthwhile in the N-S direction, except for 2616, 2614 and 2611 stations.

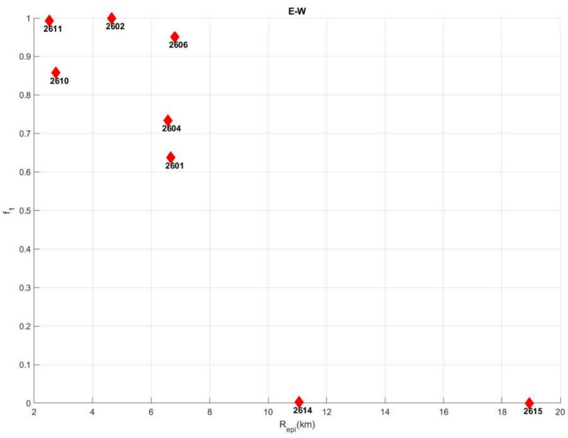

(a)

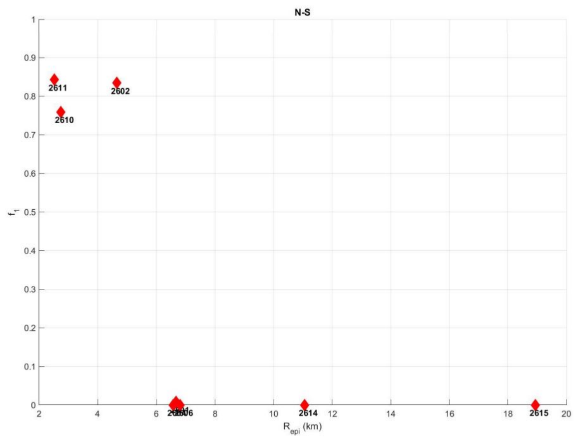

(b)

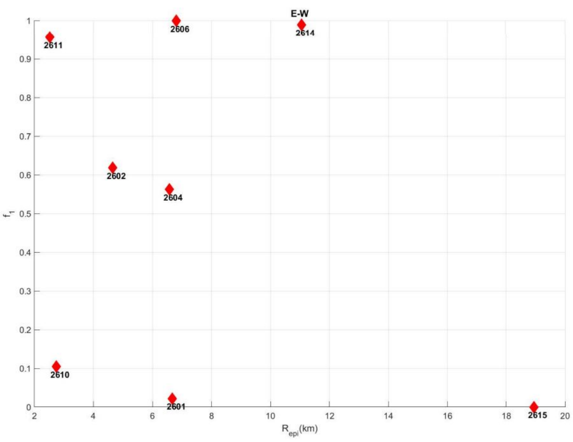

(c)

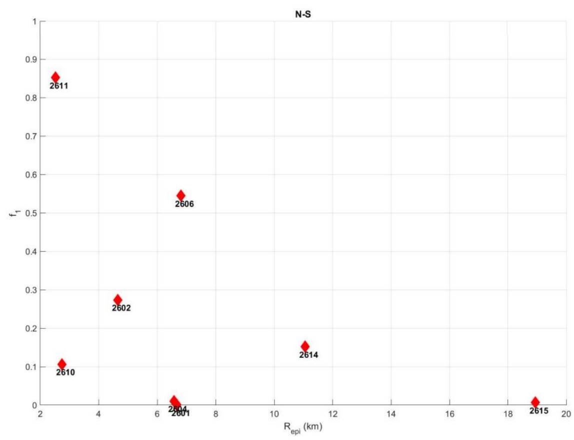

(d)

Figure 5.14. f_1 factor for 17.01.2015 Mw 3.7 using velocity model with basin (a) and (b), without basin (c) and (d) at frequency ranges of 0.3 and 1 Hz.

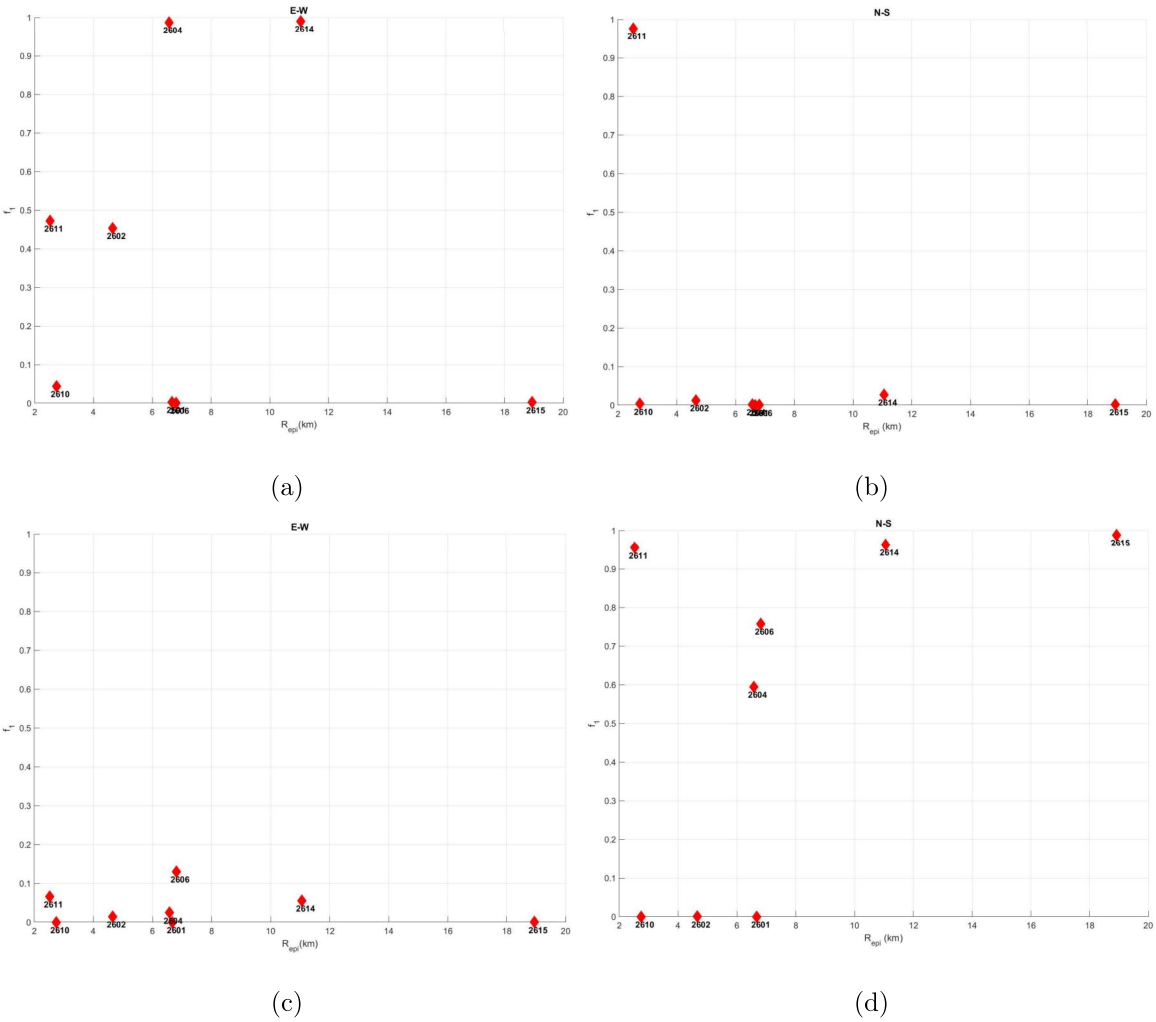

(a) (b)

(c) (d)

Figure 5.15. f_1 factor for 17.01.2015 Mw 3.7 using velocity model with (a) and (b), without basin (c) and (d) at frequency ranges of 0.3 and 0.6 Hz.

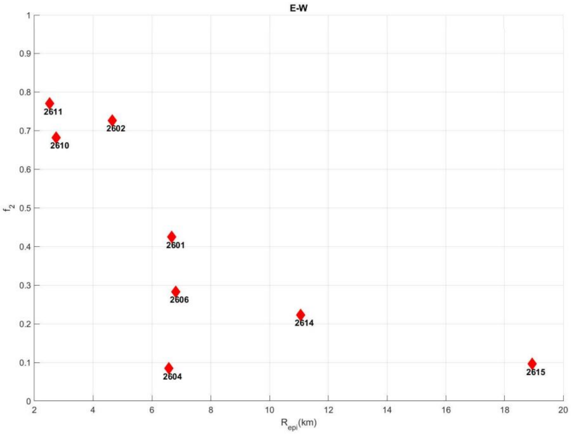

(a)

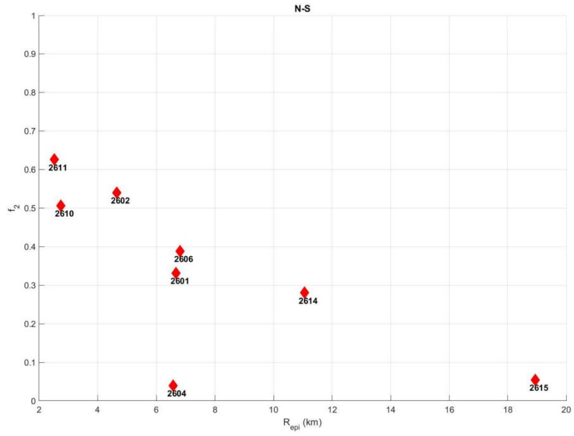

(b)

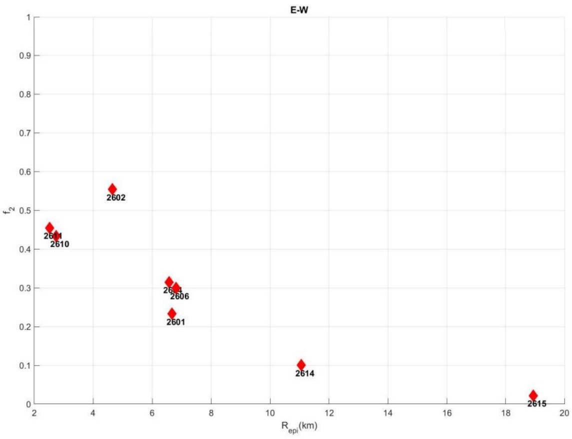

(c)

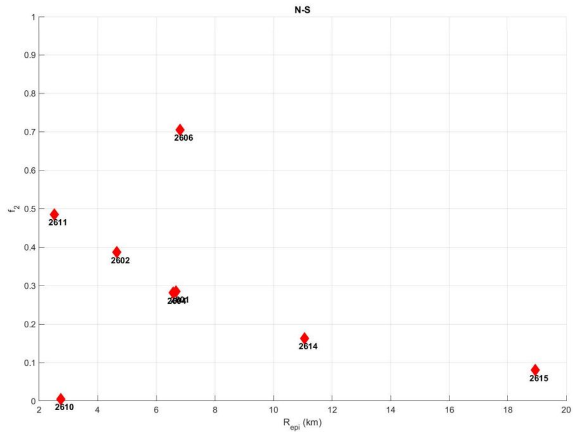

(d)

Figure 5.16. f_2 factor for 17.01.2015 Mw 3.7 using velocity model with basin (a) and (b), without basin (c) and (d) at frequency ranges of 0.3 and 1 Hz.

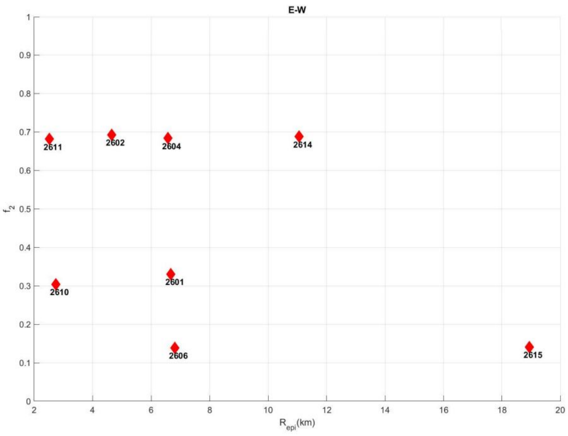

(a)

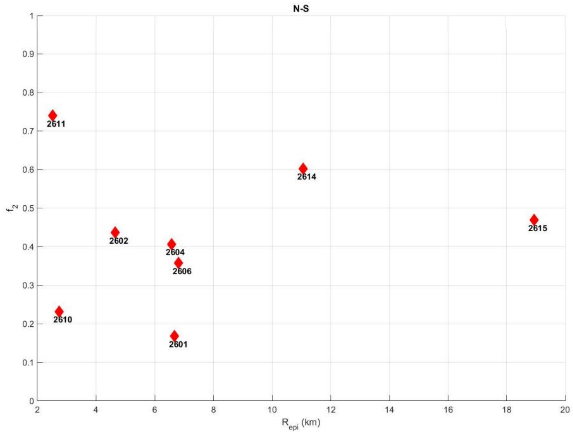

(b)

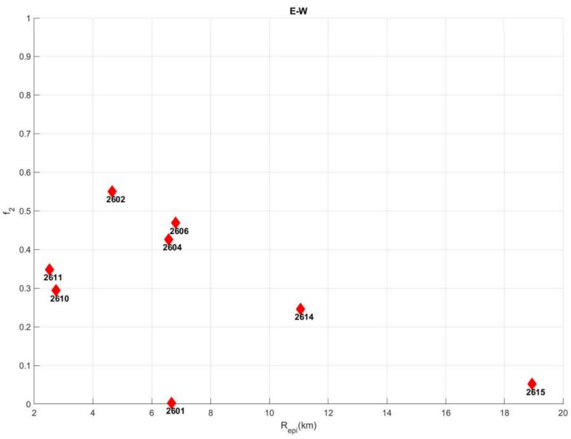

(c)

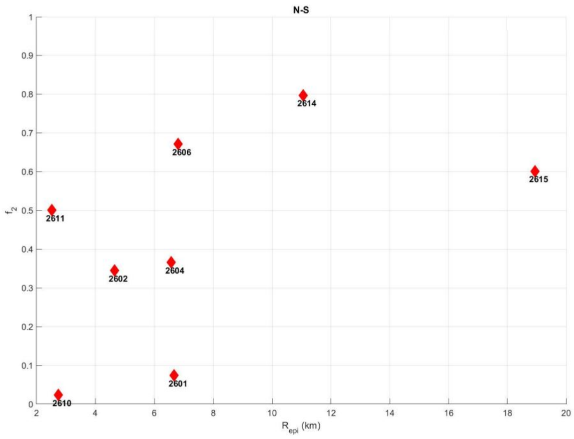

(d)

Figure 5.17. f_2 factor for 17.01.2015 Mw 3.7 using velocity model with basin (a) and (b), without basin (c) and (d) at frequency ranges of 0.3 and 0.6 Hz.

Simulation results of the 18.09.2015 Mw 3.7 earthquake were carried out using the basin model at 2606 station both amplitude and phase compatibility were achieved. In addition to the 2606 station, the 2614 station is also compatible with synthetic wave amplitudes. However, the model without a basin is generally more consistent with the observed data than the model with a basin. The simulation result of both earthquakes performed with the basin model indicated that the basin velocity structure does not represent the underlying layers of the 2610 station.

5.2.1. Propagation of Synthetic waves in Eskişehir Basin

In this chapter, we have investigated the wave propagation by virtual stations. Furthermore, it aims to reveal basin geometry's effects on the distribution of intensity measures in PGV at distinct frequencies. Two models on the distribution of virtual stations are utilized to understand the wave's behavior inside and outside the basin. The first model consists of 120 virtual stations, covering an epicenter of 17.01.2015 Mw 4.3, each 5 km for two axes, to determine IM distribution in the whole field, as shown in Figure 5.18. The second model comprises the only interested Eskişehir basin area to focus on the Eskişehir basin via the dense fictitious stations where geological exploration is carried out, as demonstrated in Figure 5.19.

Furthermore, the velocity-time series simulated using two distinct velocity models were examined to characterize the motion belonging to different basement depths and locations. Besides, the near-source motion is driven by the source radiation, directivity effect, and deep basin. The epicentral distance varies from 0 to 43 km in the basin.

Moreover, the recorded PGV values were superimposed on the PGV distribution map. However, 17.01.2015 Mw 4.3 is captured by twelve stations, while 18.09.2015 Mw 3.7 is recorded by eight stations. Spatial distribution of intensity measure is unavailable for the deepest Eskişehir basin in the east because the east part of the basin is not densely equipped with accelerometers. The location of the imaginary stations is given in the following Figures.

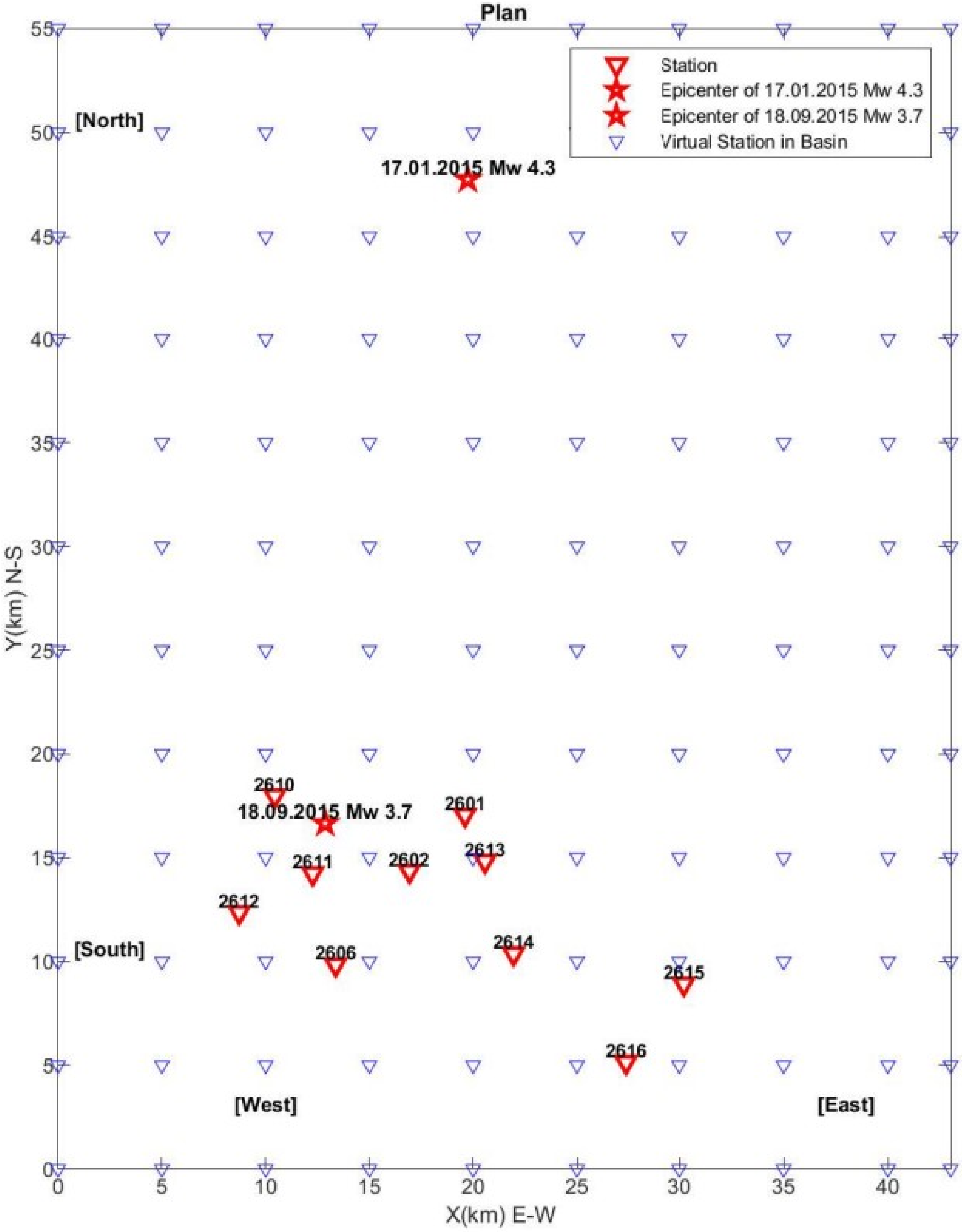

Figure 5.18. Distribution of seismic stations and all virtual stations spatially.

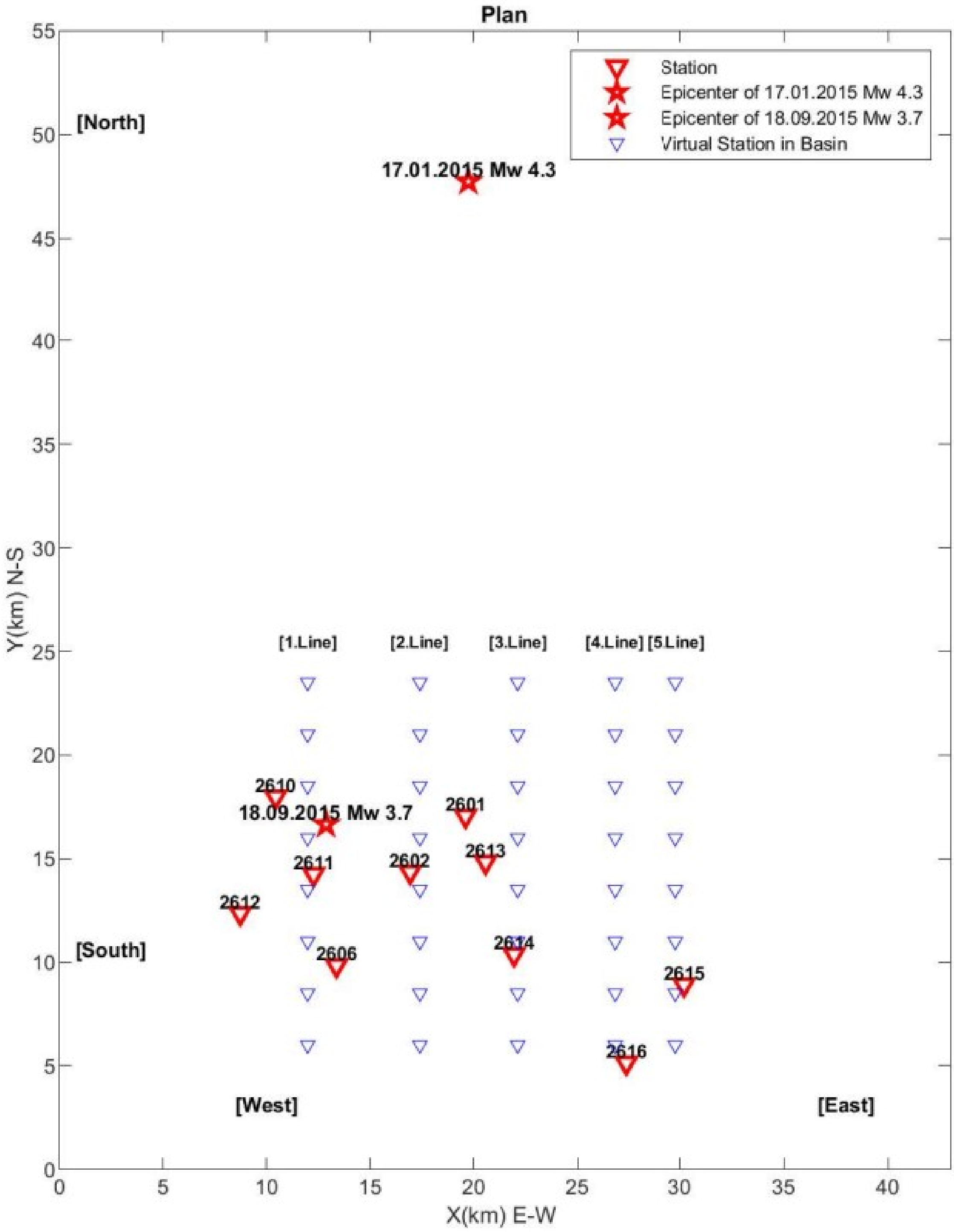

Figure 5.19. Distribution of seismic stations and virtual stations which are only located on the basin.

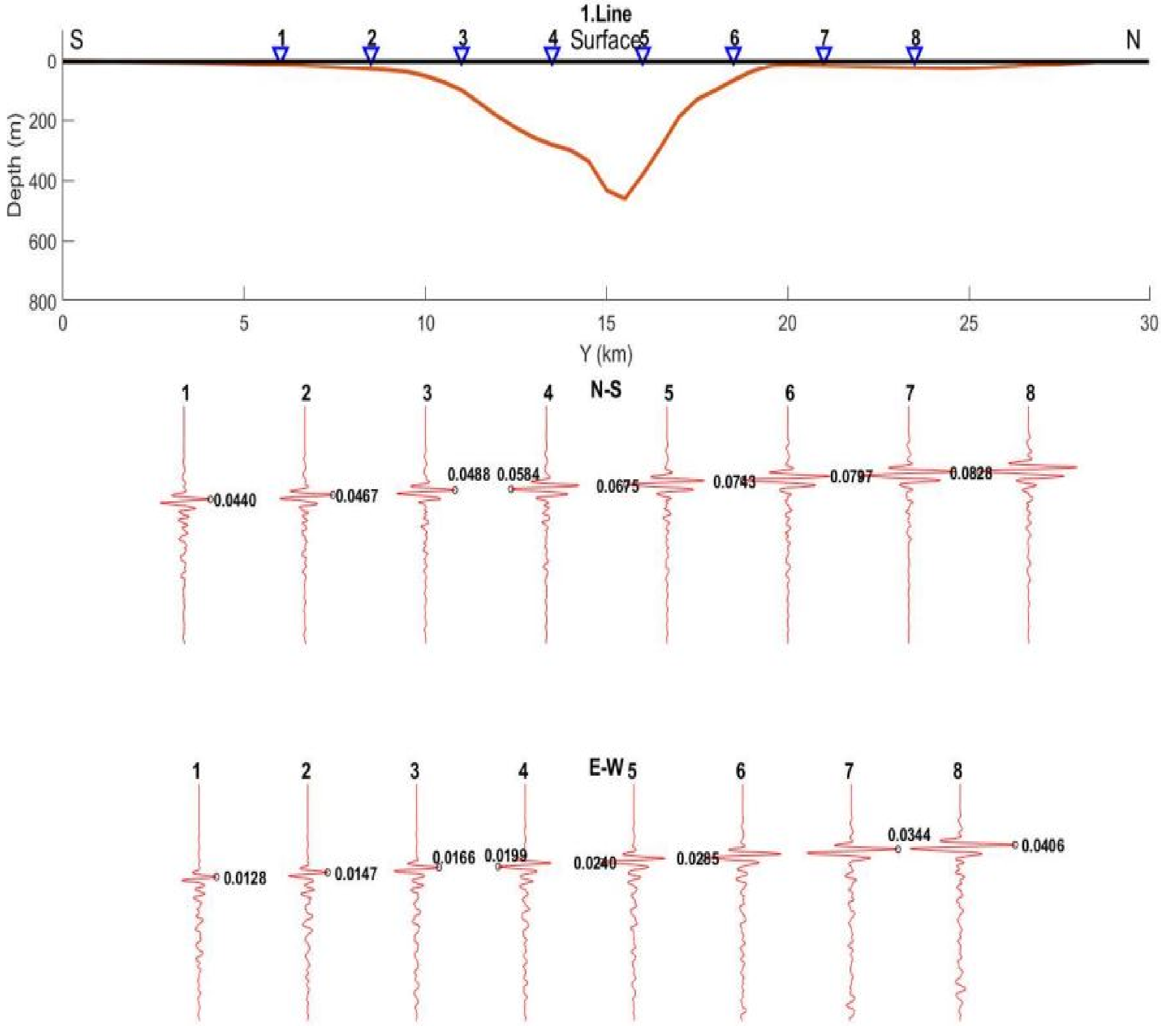

Figure 5.20. The generated velocity time histories of 17.01.2015 Mw 4.3 using Mindavelli model without basin bandpass filtered at 0.3-1 Hz (unit of cm/s).

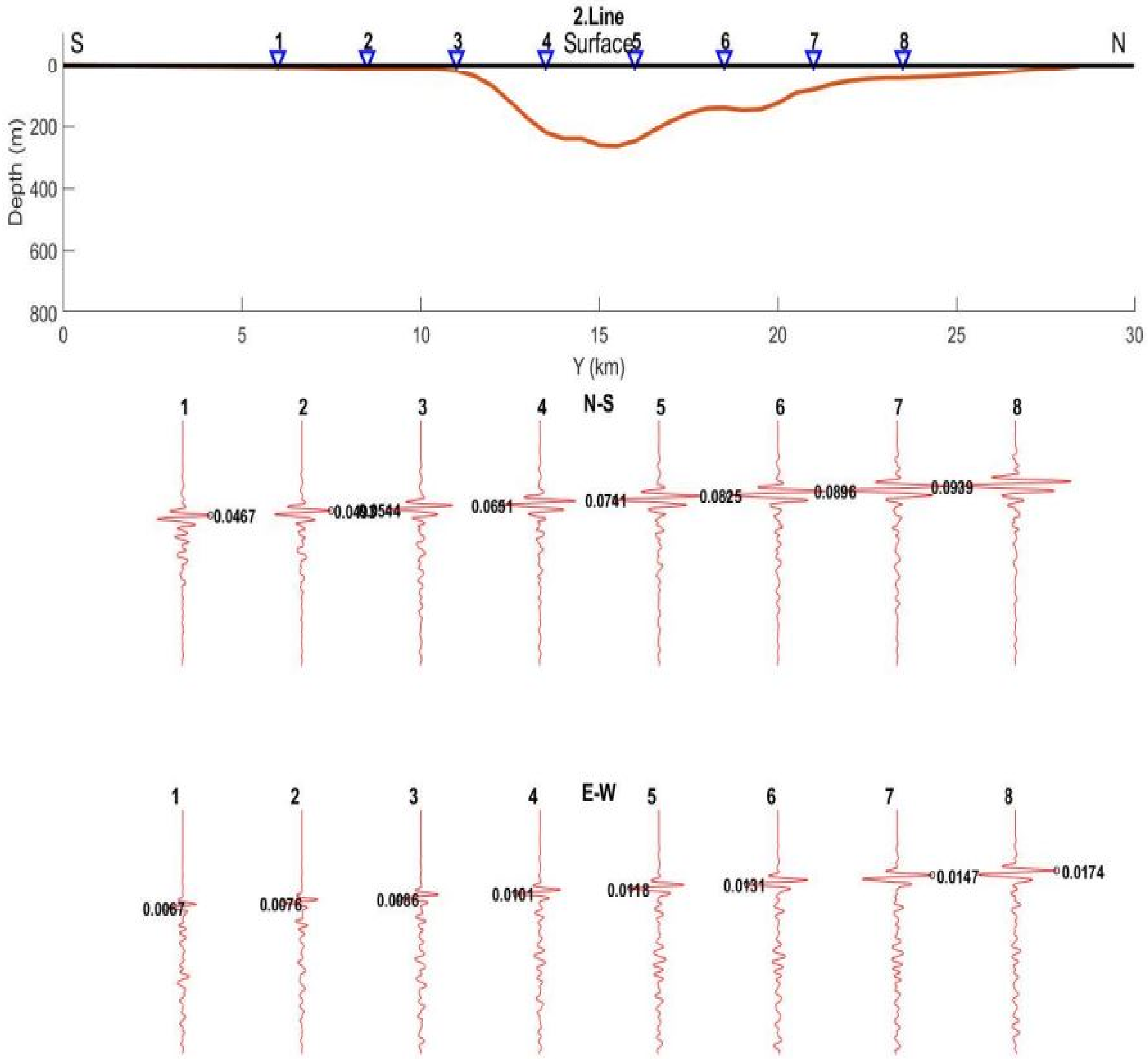

Figure 5.21. The generated velocity time histories of 17.01.2015 Mw 4.3 using Mindavelli model without basin bandpass filtered at 0.3-1 Hz (unit of cm/s).

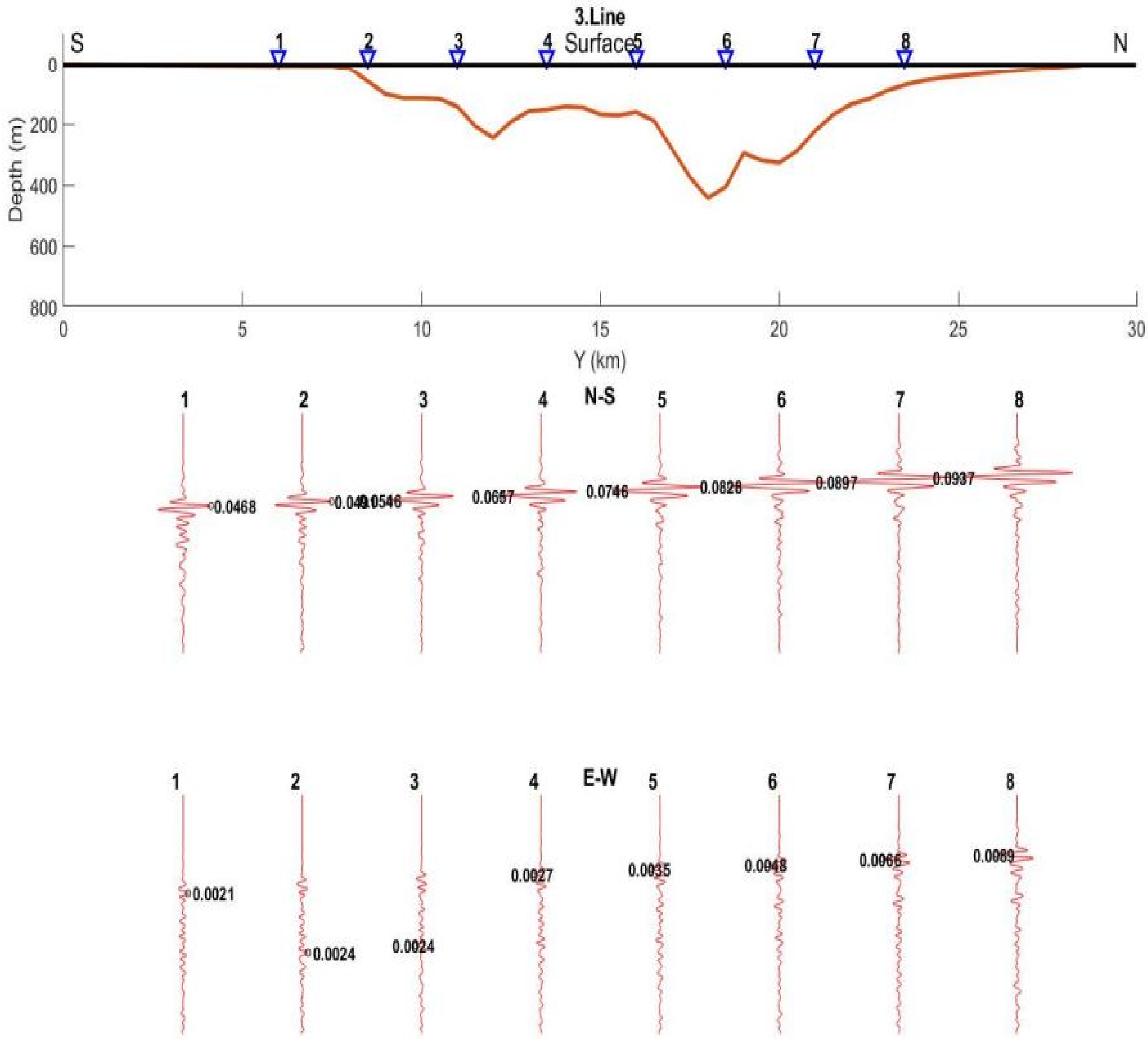

Figure 5.22. The generated velocity time histories of 17.01.2015 Mw 4.3 using Mindavelli model without basin bandpass filtered at 0.3-1 Hz (unit of cm/s).

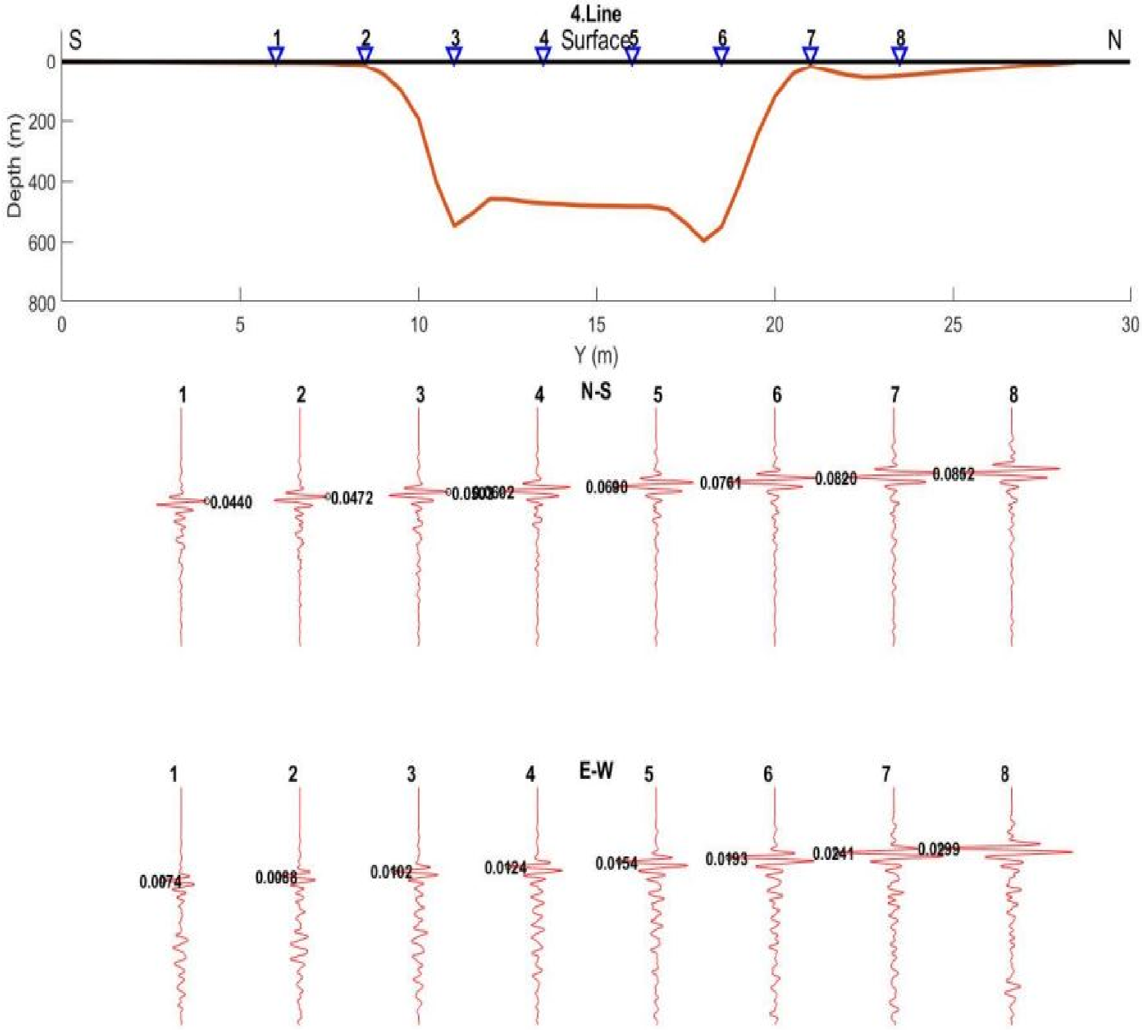

Figure 5.23. The generated velocity time histories of 17.01.2015 Mw 4.3 using Mindavelli model without basin bandpass filtered at 0.3-1 Hz (unit of cm/s).

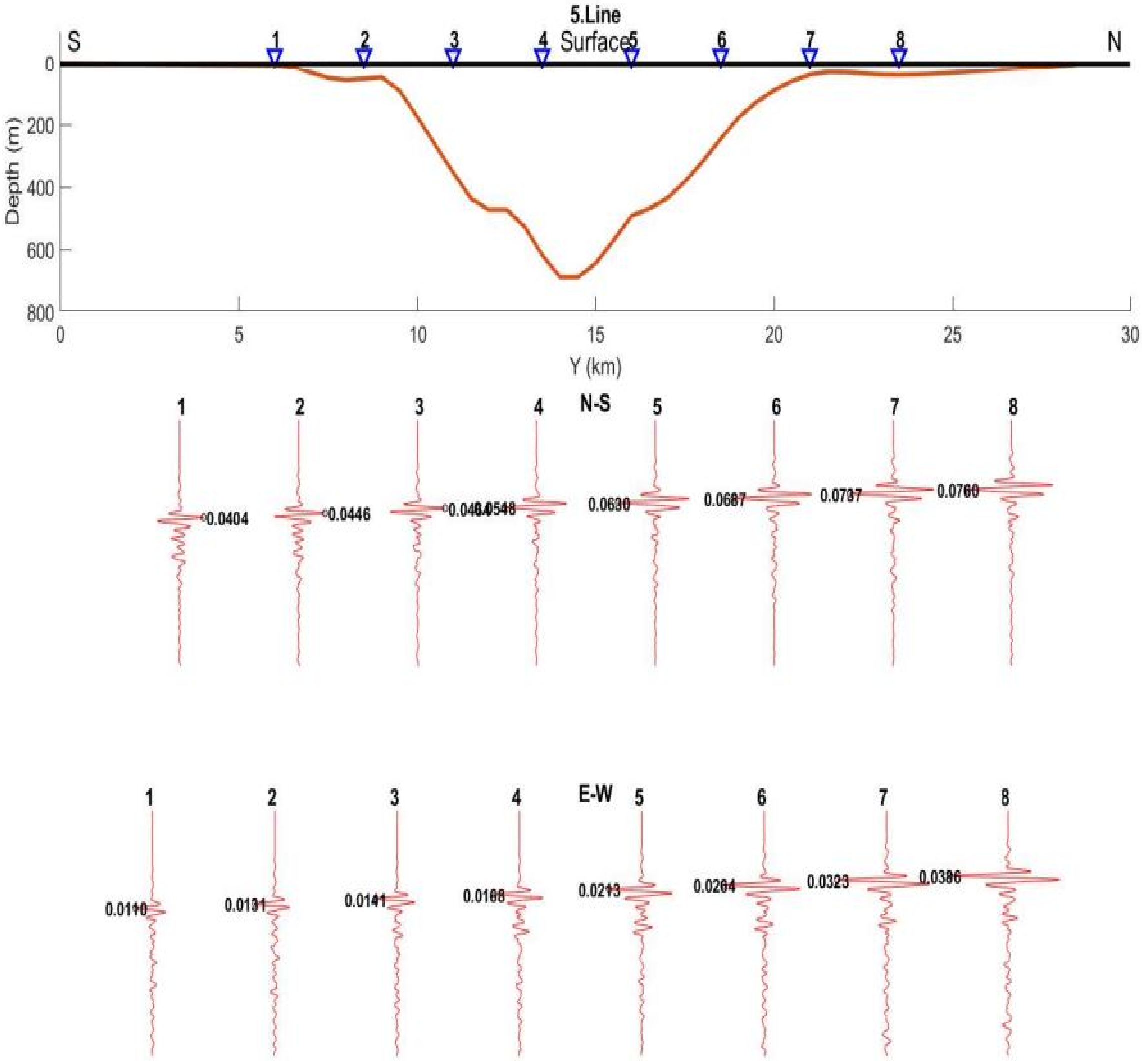

Figure 5.24. The generated velocity time histories of 17.01.2015 Mw 4.3 using Mindavelli model without basin bandpass filtered at 0.3-1 Hz (unit of cm/s).

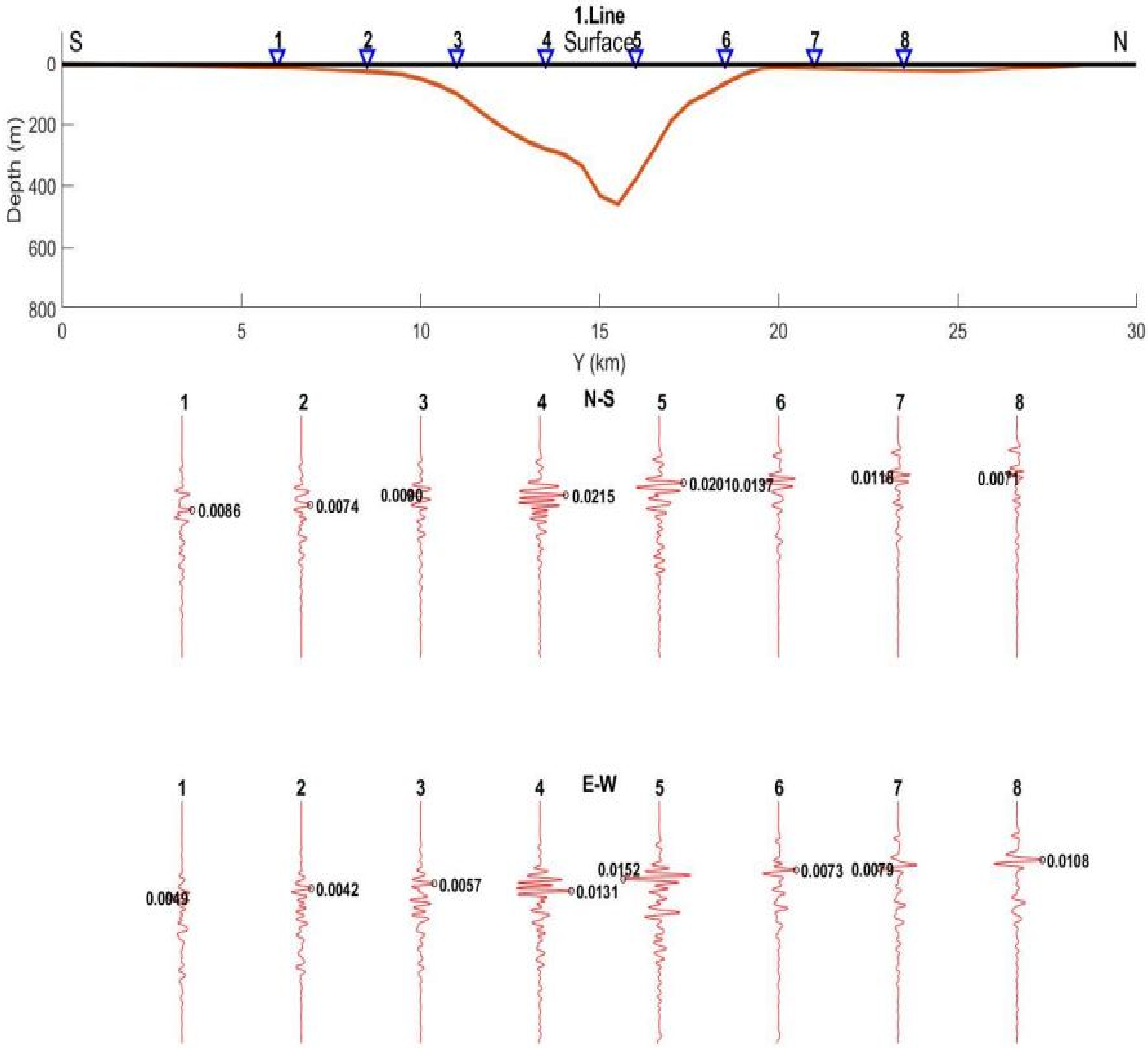

Figure 5.25. The generated velocity time histories of 17.01.2015 Mw 4.3 using Mindavelli model with basin bandpass filtered at 0.3-1 Hz (unit of cm/s).

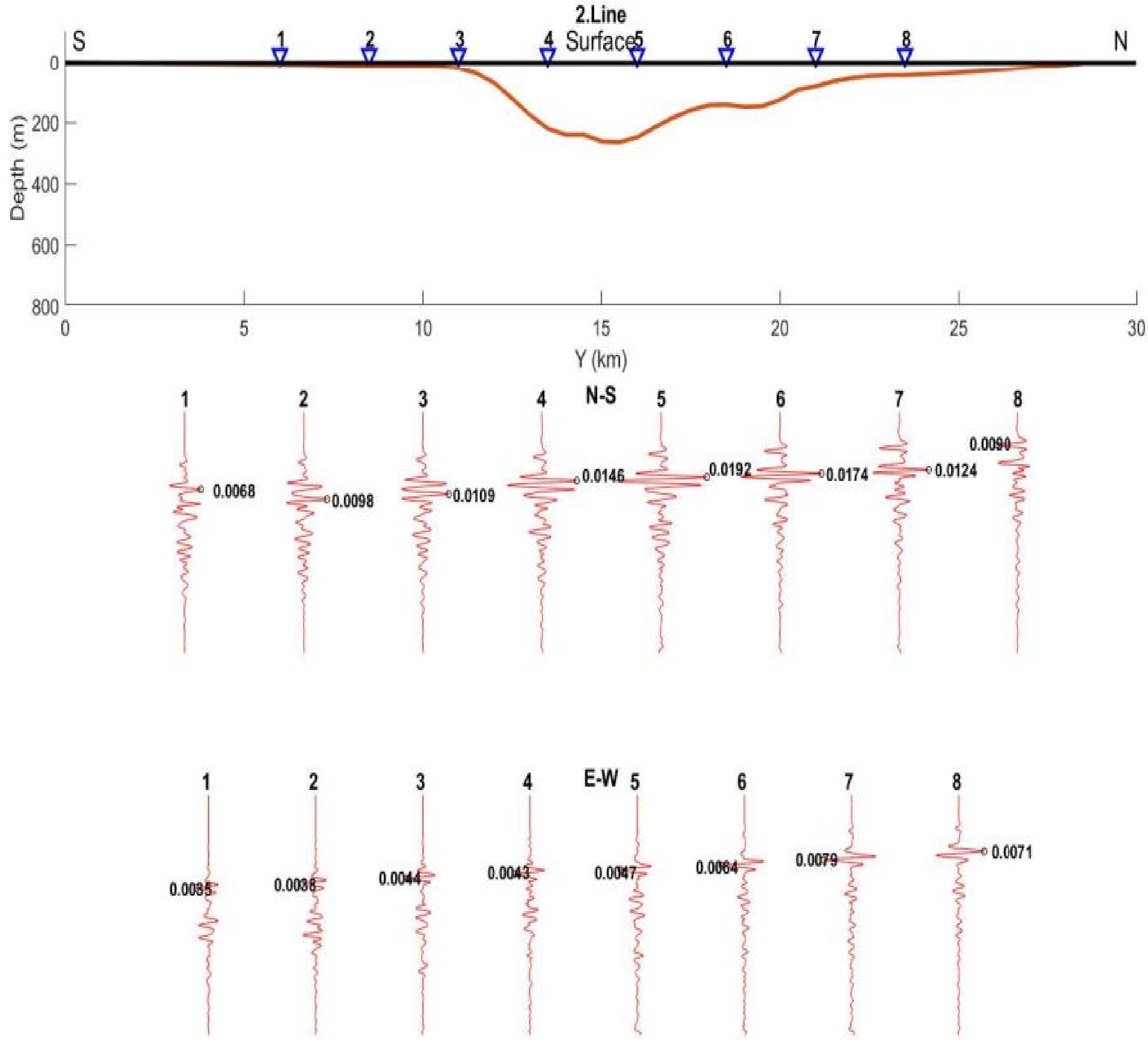

Figure 5.26. The generated velocity time histories of 17.01.2015 Mw 4.3 using Mindavelli model with basin bandpass filtered at 0.3-1 Hz (unit of cm/s).

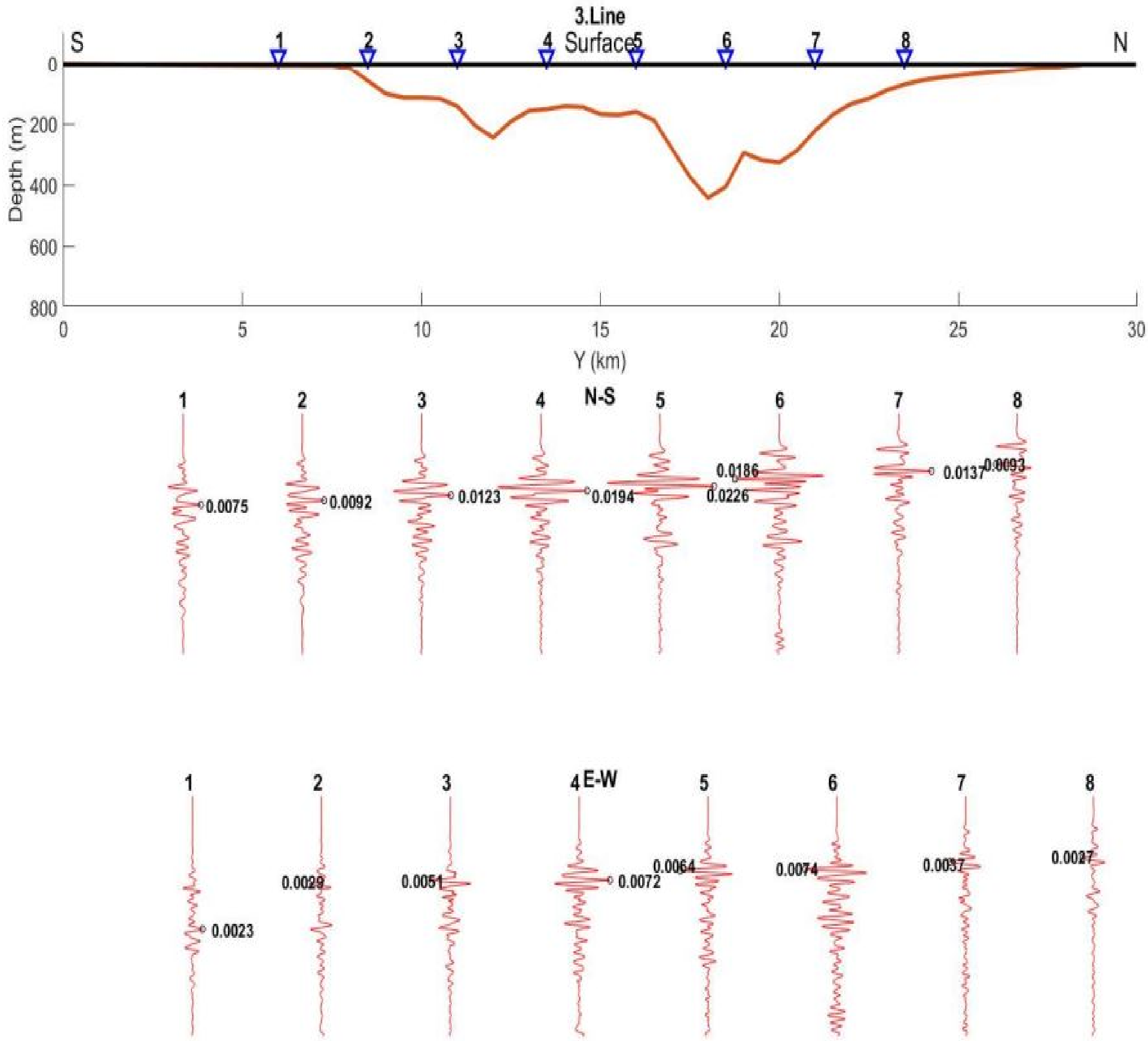

Figure 5.27. The generated velocity time histories of 17.01.2015 Mw 4.3 using Mindavelli model with basin bandpass filtered at 0.3-1 Hz (unit of cm/s).

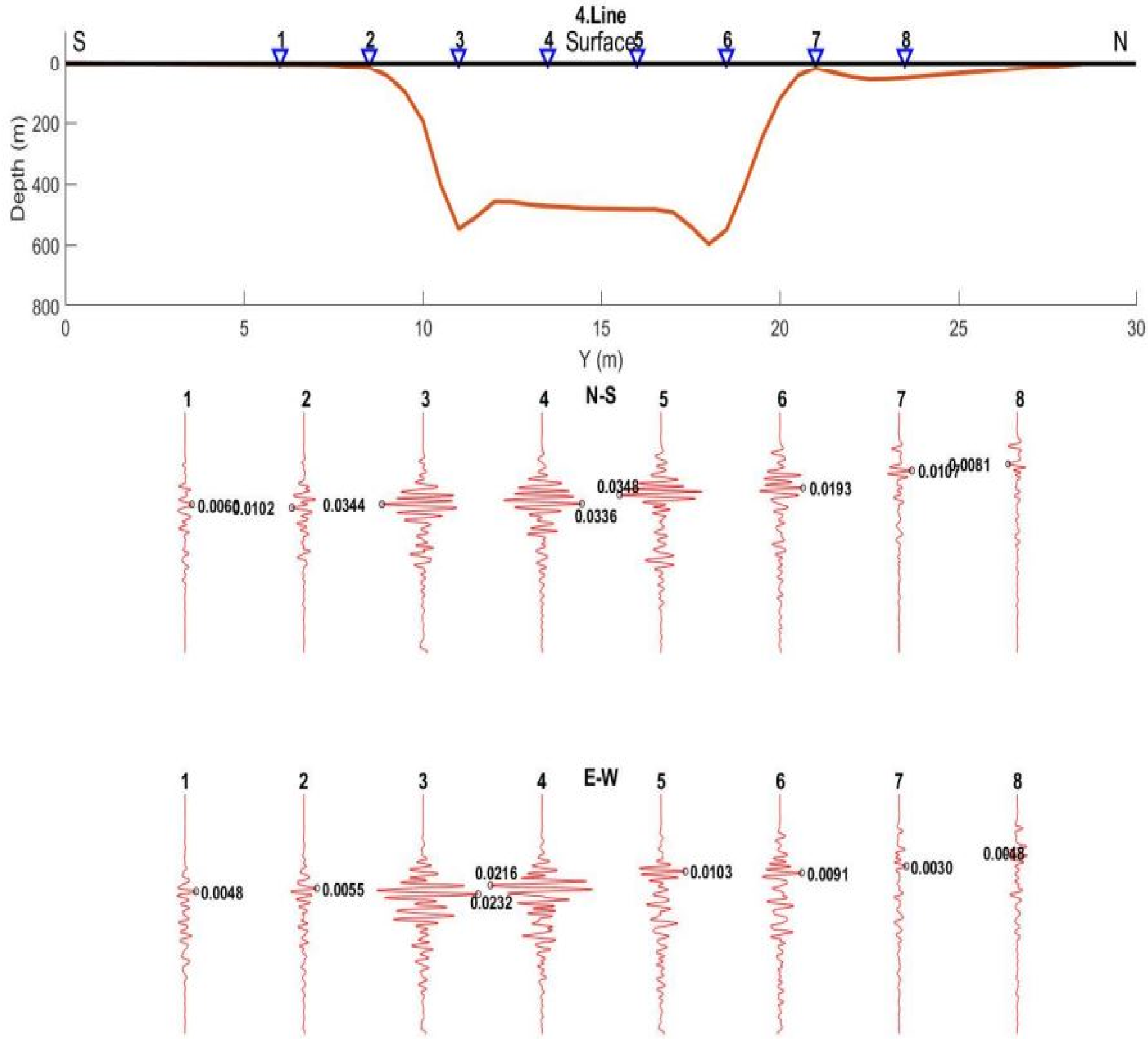

Figure 5.28. The generated velocity time histories of 17.01.2015 Mw 4.3 using Mindavelli model with basin bandpass filtered at 0.3-1 Hz (unit of cm/s).

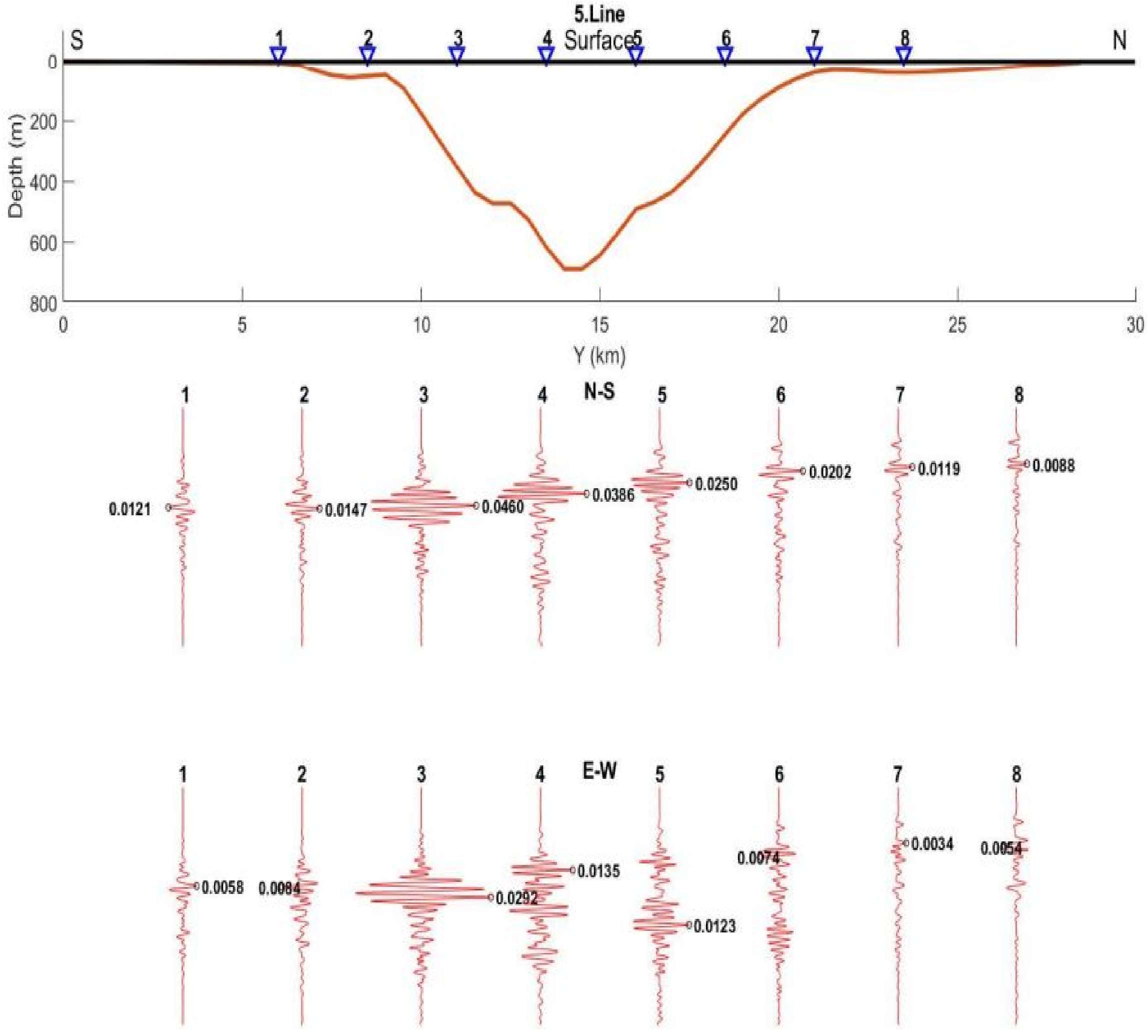

Figure 5.29. The generated velocity time histories of 17.01.2015 Mw 4.3 using Mindavelli model with basin bandpass filtered at 0.3-1 Hz (unit of cm/s).

Table 5.2. Simulation results of 17.01.2015 Mw 4.3 among the lines using the Mindevalli velocity model without basin.

Mindevalli without Basin Model					
PGVmax(cm/s)					
0.3-0.6 Hz			**0.3-1Hz**		
EW	**NS**	**UD**	**EW**	**NS**	**UD**
0.0135	0.0293	0.012	0.0406	0.0939	0.0295

Table 5.3. Simulation results of 17.01.2015 Mw 4.3 among the lines using the Mindevalli velocity model with basin.

Mindevalli with Basin Model					
PGVmax(cm/s)					
0.3-0.6 Hz			0.3-1Hz		
EW	NS	UD	EW	NS	UD
0.0041	0.0078	0.0139	0.0292	0.046	0.0718

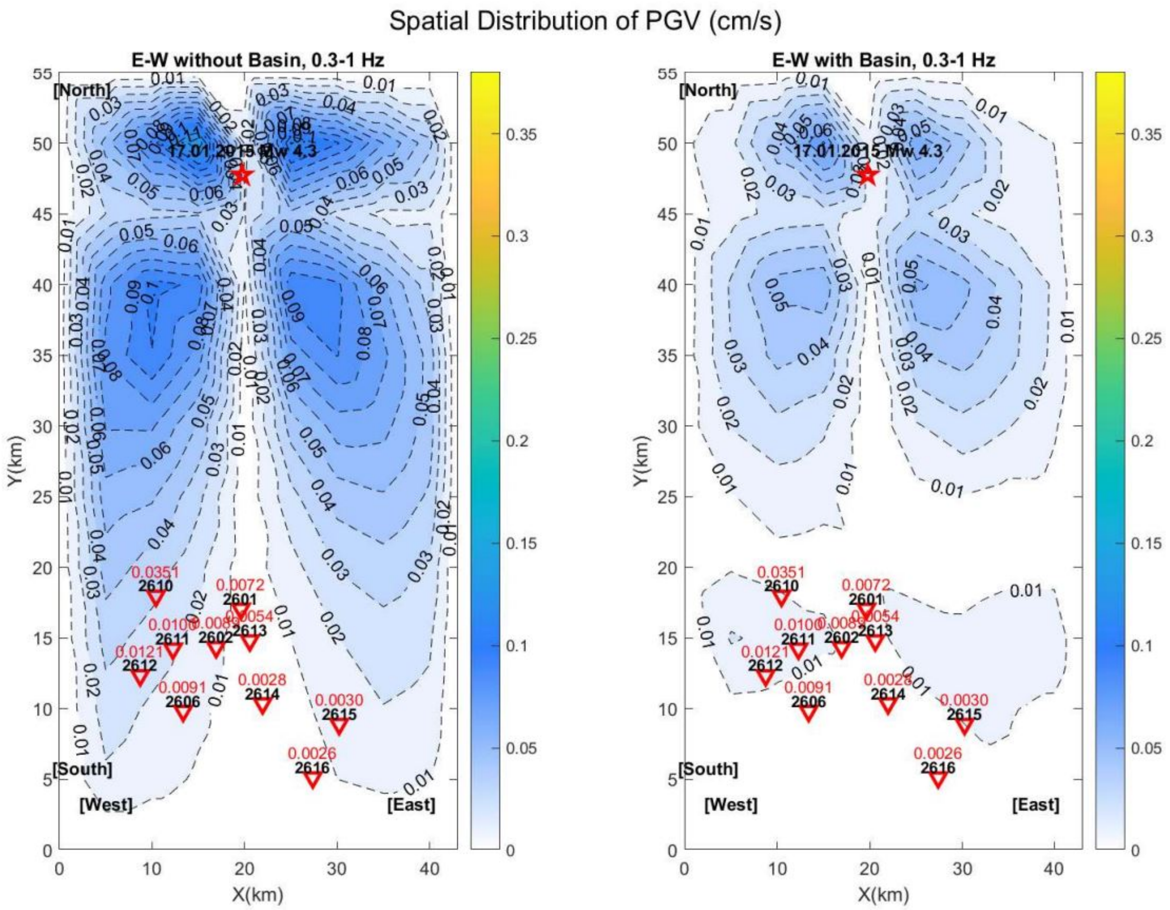

Figure 5.30. Spatial Distribution of PGV (cm/s) for two Models at frequency ranges of 0.3-1 Hz in EW (17.01.2015 Mw 4.3). Left Figure shows the PGV distribution using flat velocity structure, right Figure indicates the PGV distribution using velocity structure added basin on top.

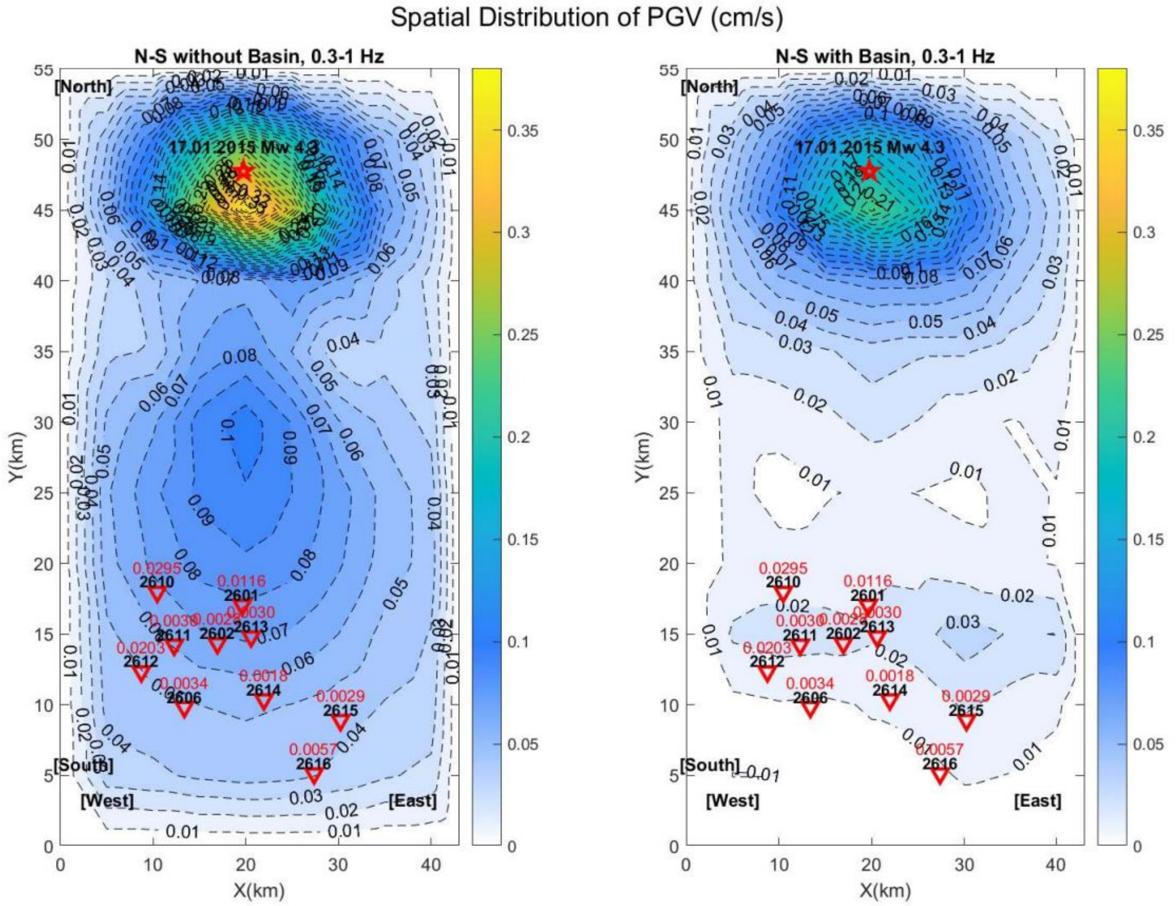

Figure 5.31. Spatial Distribution of PGV (cm/s) for two Models at frequency ranges of 0.3-1 Hz in NS (17.01.2015 Mw 4.3). Left Figure shows the PGV distribution using flat velocity structure, right Figure indicates the PGV distribution using velocity structure added basin on top.

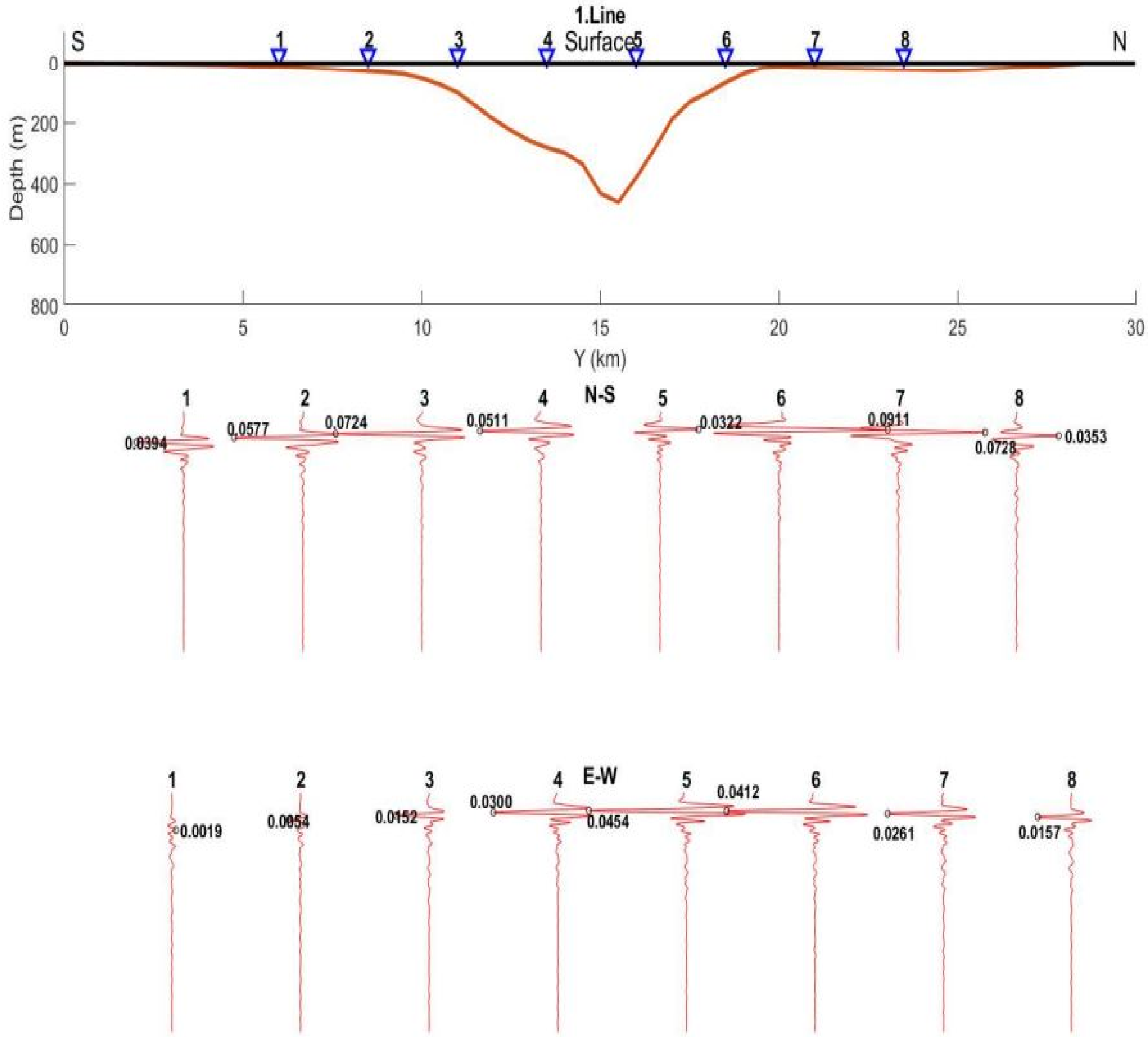

Figure 5.32. The generated velocity time histories of 18.09.2015 Mw 3.7 using Mindavelli model without basin bandpass filtered at 0.3-1 Hz (unit of cm/s).

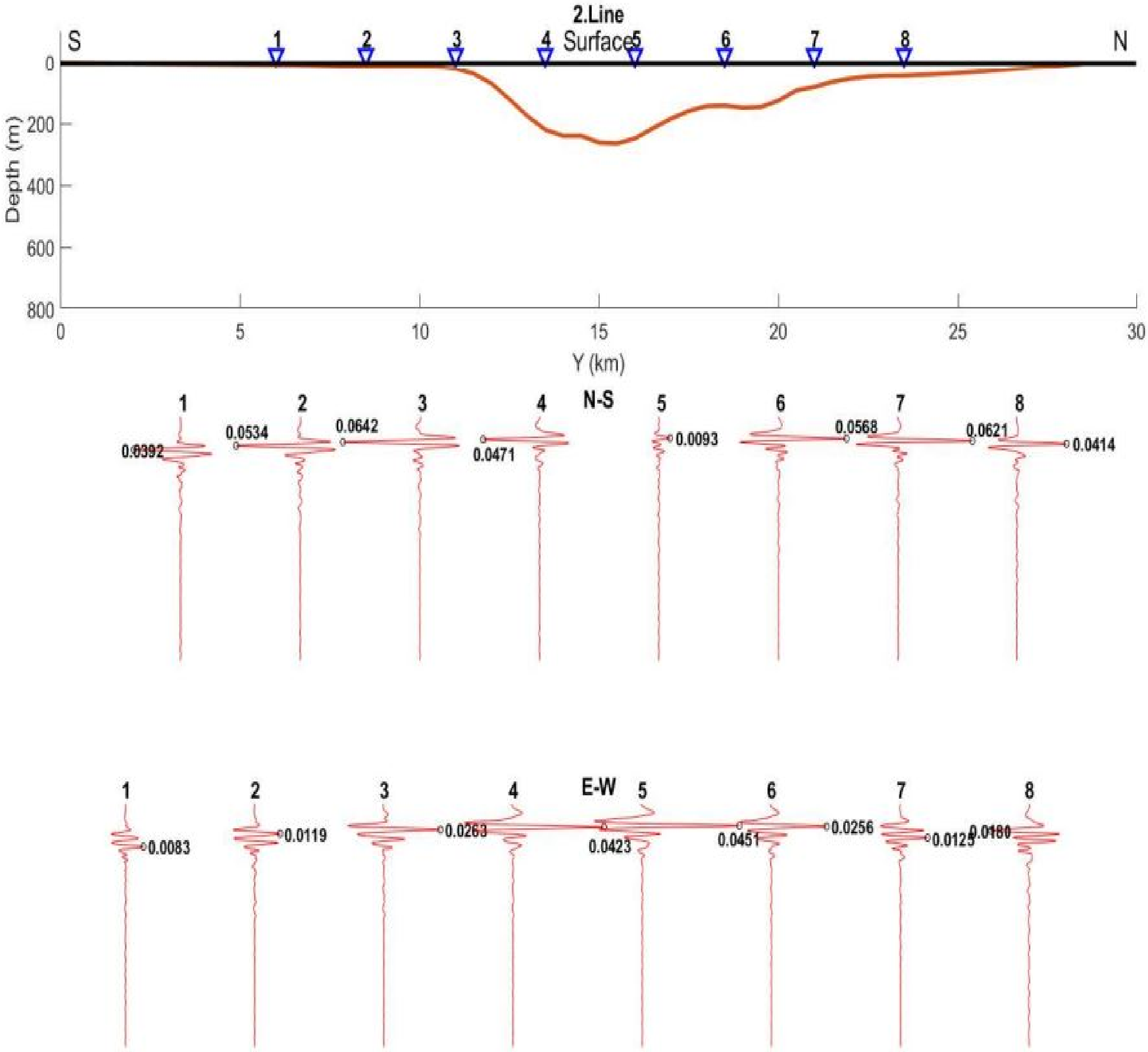

Figure 5.33. The generated velocity time histories of 18.09.2015 Mw 3.7 using Mindavelli model without basin bandpass filtered at 0.3-1 Hz (unit of cm/s).

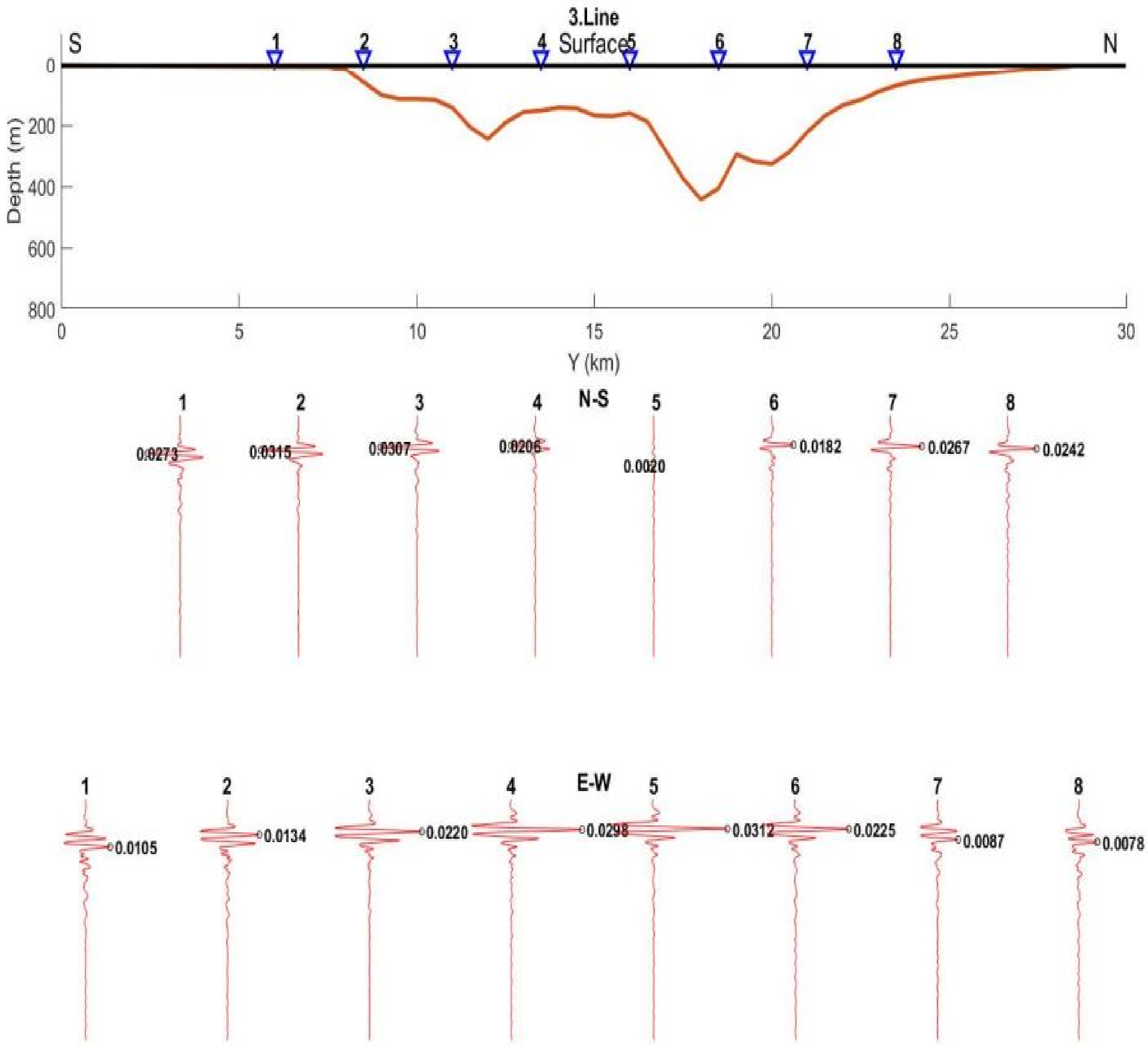

Figure 5.34. The generated velocity time histories of 18.09.2015 Mw 3.7 using Mindavelli model without basin bandpass filtered at 0.3-1 Hz (unit of cm/s).

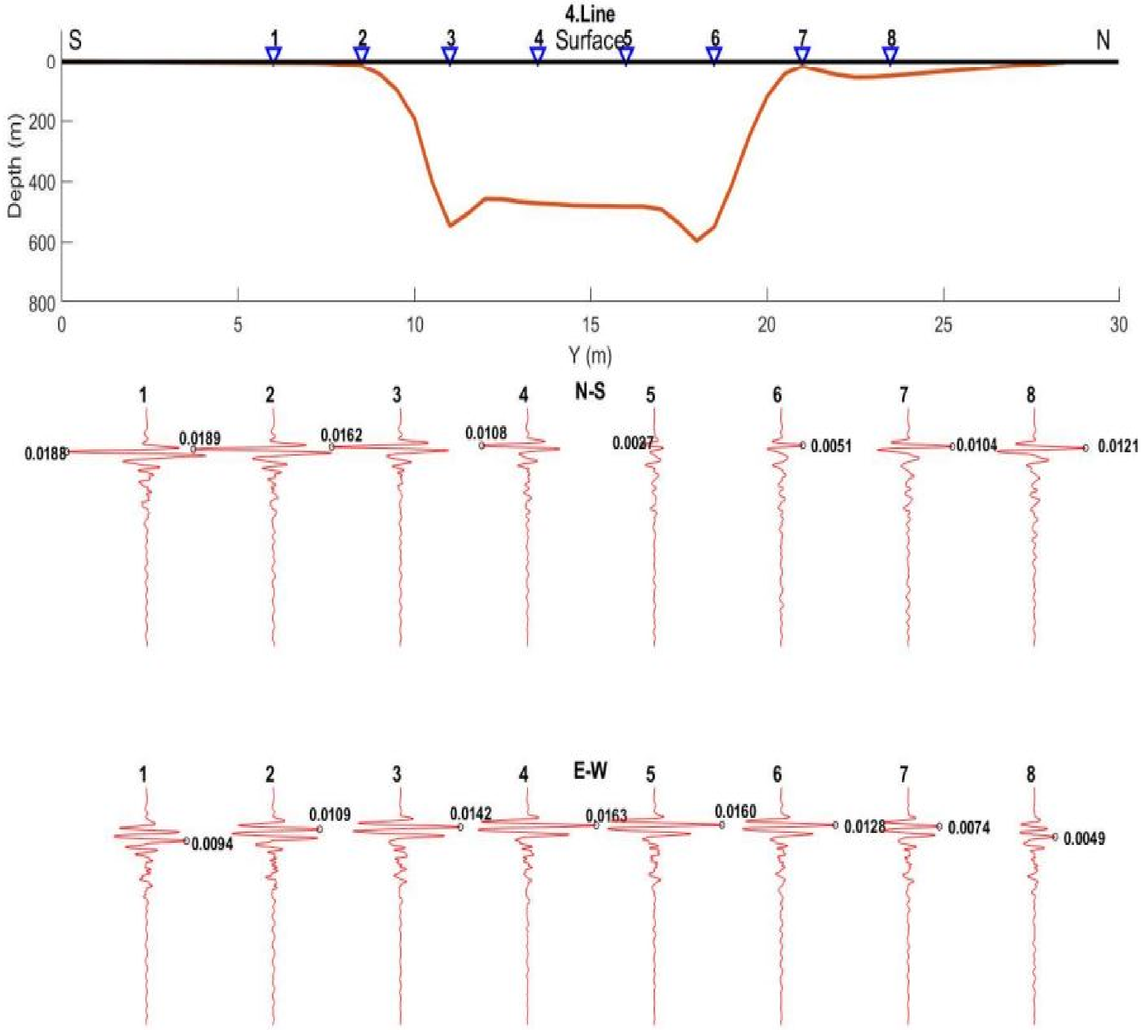

Figure 5.35. The generated velocity time histories of 18.09.2015 Mw 3.7 using Mindavelli model without basin bandpass filtered at 0.3-1 Hz (unit of cm/s).

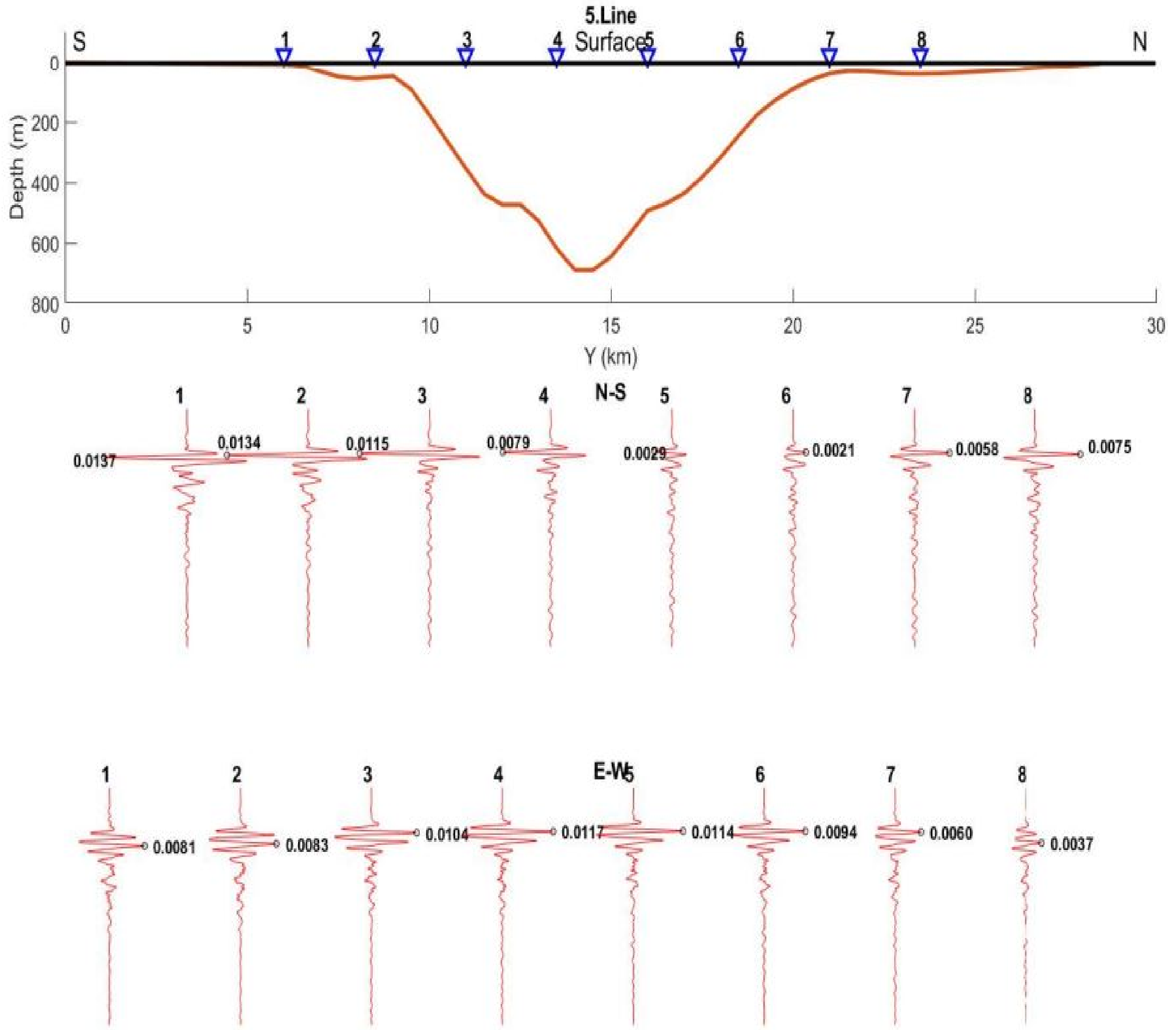

Figure 5.36. The generated velocity time histories of 18.09.2015 Mw 3.7 using Mindavelli model without basin bandpass filtered at 0.3-1 Hz (unit of cm/s).

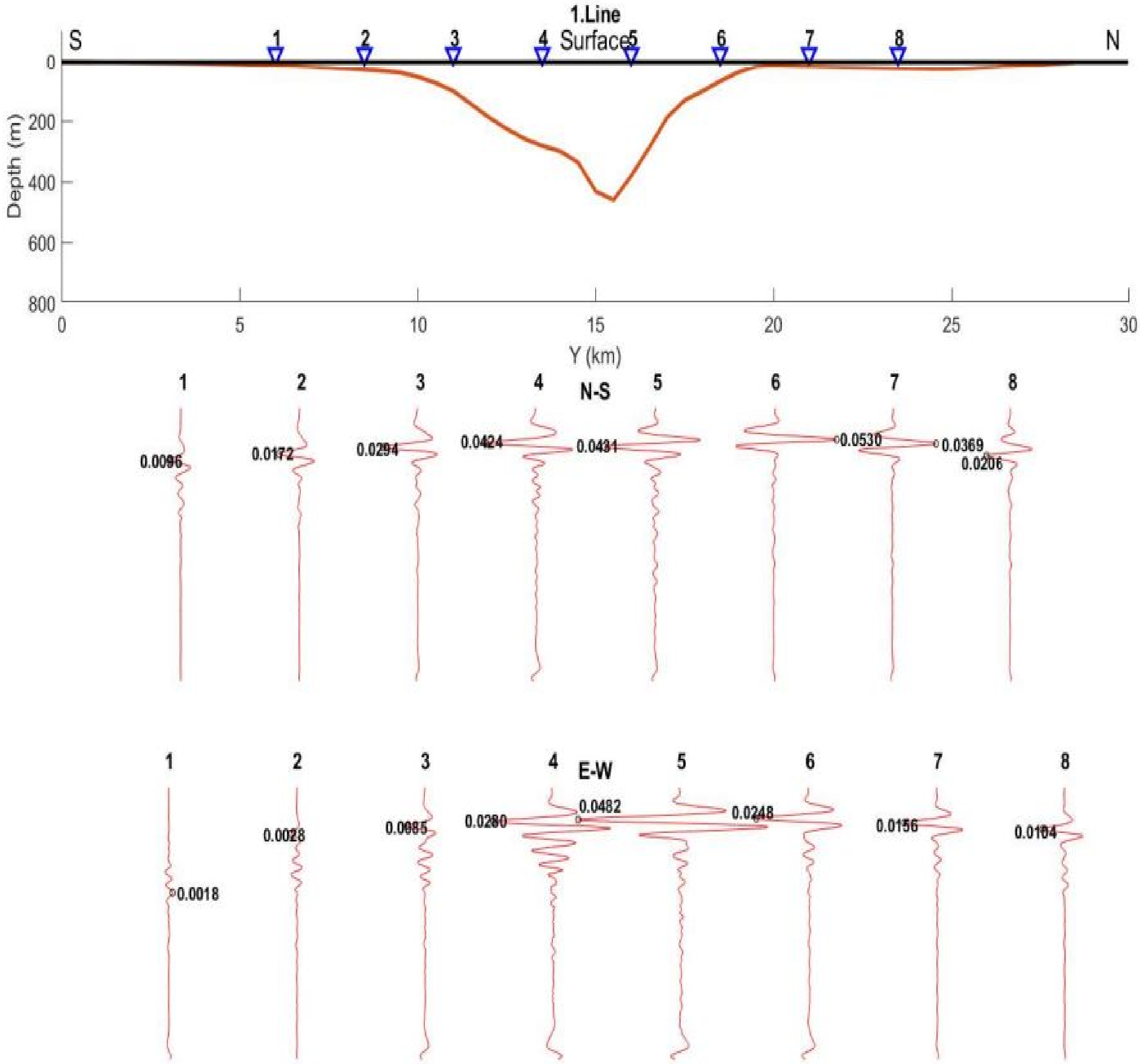

Figure 5.37. The generated velocity time histories of 18.09.2015 Mw 3.7 using Mindavelli model with basin bandpass filtered at 0.3-1 Hz (unit of cm/s).

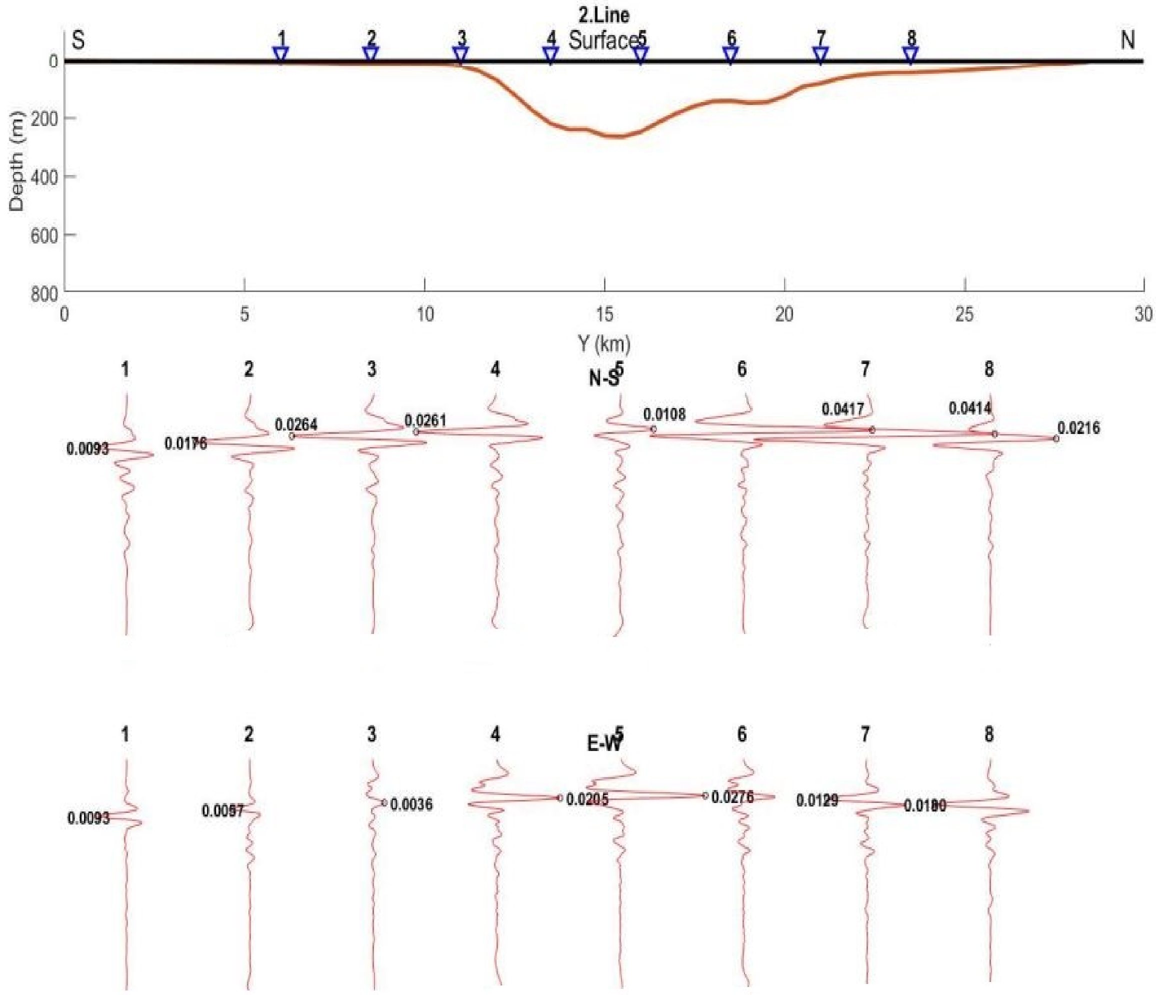

Figure 5.38. The generated velocity time histories of 18.09.2015 Mw 3.7 using Mindavelli model with basin bandpass filtered at 0.3-1 Hz (unit of cm/s).

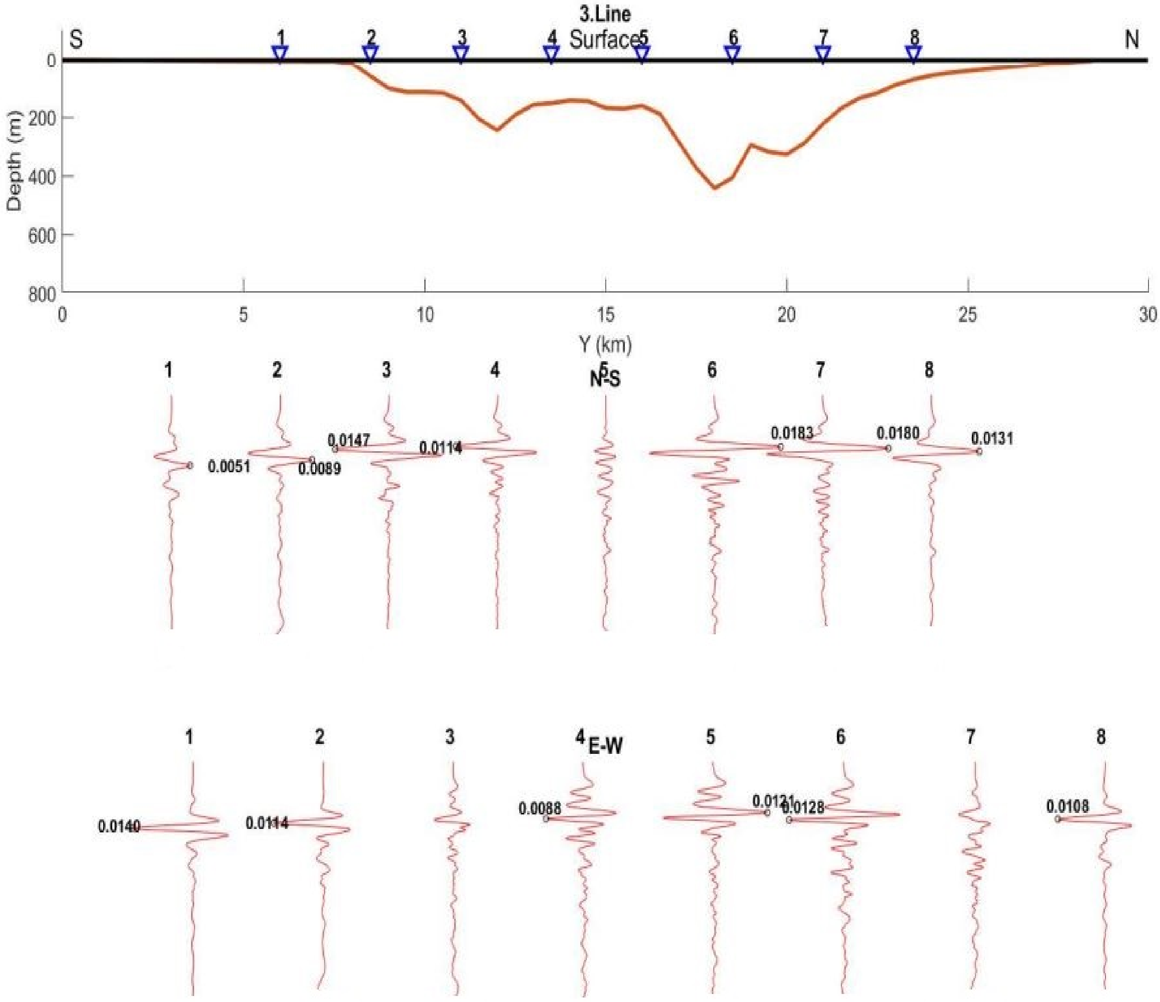

Figure 5.39. The generated velocity time histories of 18.09.2015 Mw 3.7 using Mindavelli model with basin bandpass filtered at 0.3-1 Hz (unit of cm/s).

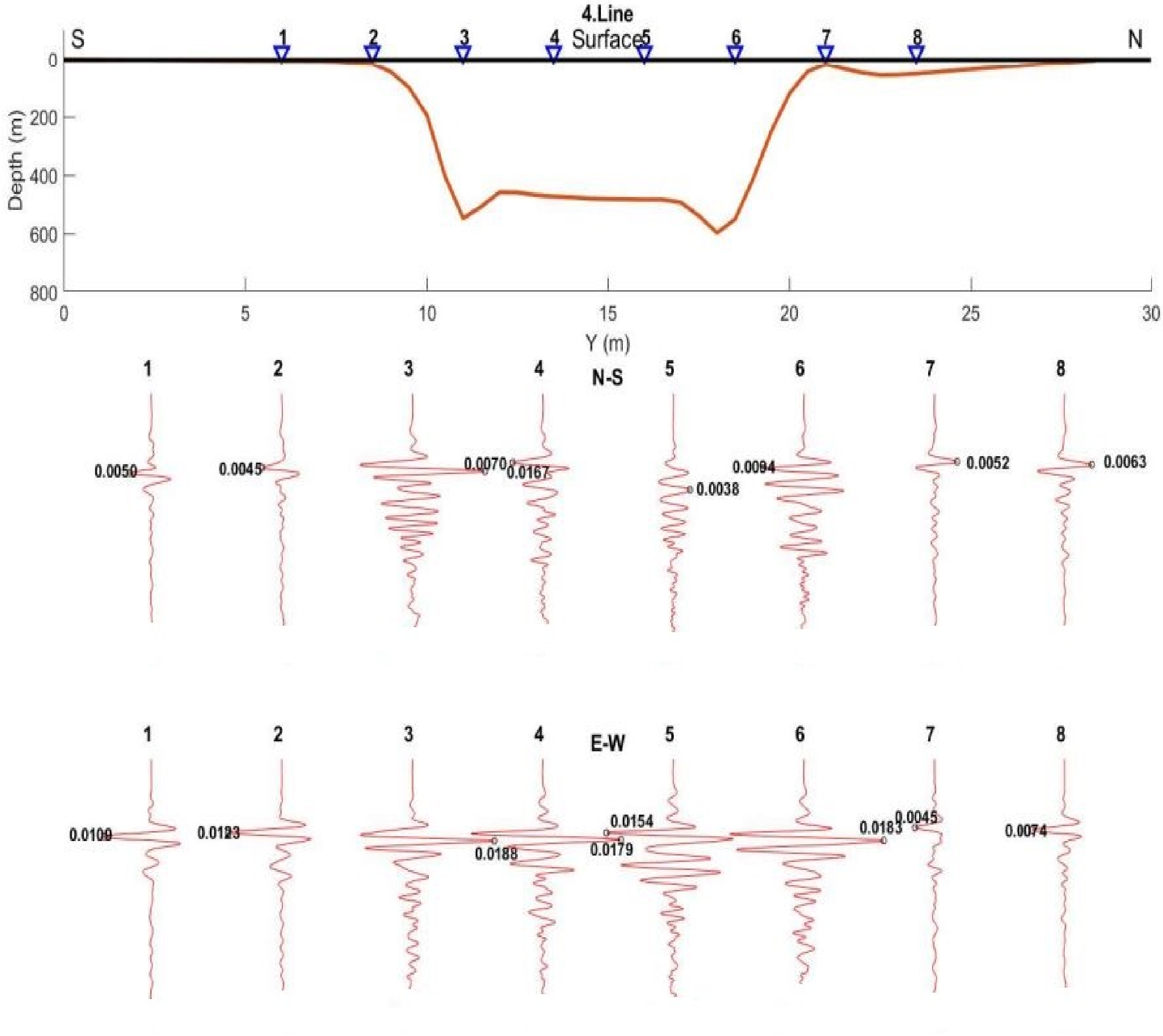

Figure 5.40. The generated velocity time histories of 18.09.2015 Mw 3.7 using Mindavelli model with basin bandpass filtered at 0.3-1 Hz (unit of cm/s).

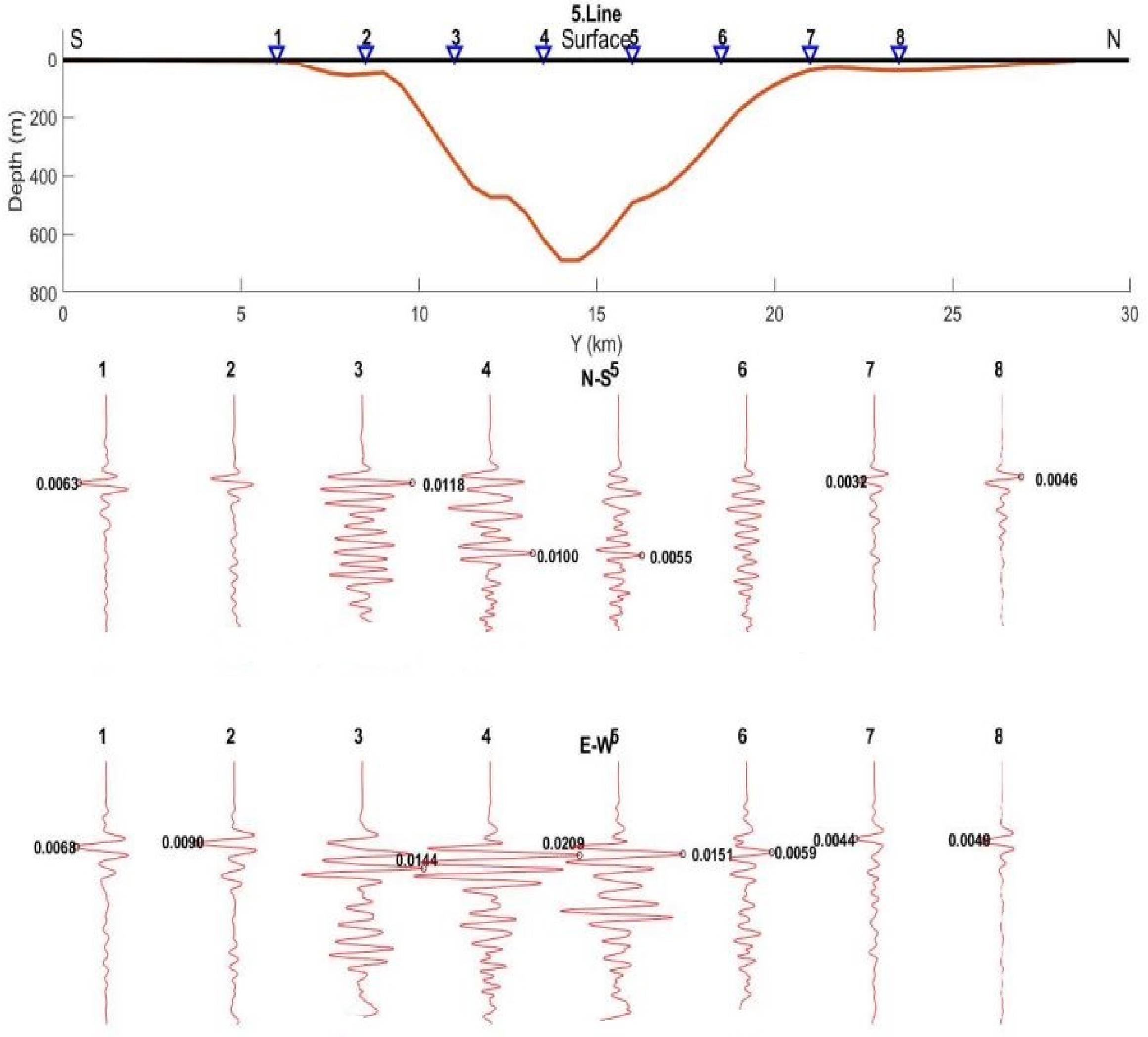

Figure 5.41. The generated velocity time histories of 18.09.2015 Mw 3.7 using Mindavelli model with basin bandpass filtered at 0.3-1 Hz (unit of cm/s).

Table 5.4. Simulation results of 18.09.2015 Mw 3.7 among the lines using the Mindevalli velocity model without basin.

Mindevalli without Basin Model					
PGVmax(cm/s)					
0.3-0.6 Hz			**0.3-1Hz**		
EW	**NS**	**UD**	**EW**	**NS**	**UD**
0.012	0.015	0.011	0.048	0.053	0.029

Table 5.5. Simulation results of 18.09.2015 Mw 3.7 among the lines using the Mindevalli velocity model with basin.

Mindevalli with Basin Model					
PGVmax(cm/s)					
0.3-0.6 Hz			0.3-1Hz		
EW	NS	UD	EW	NS	UD
0.015	0.028	0.015	0.045	0.091	0.024

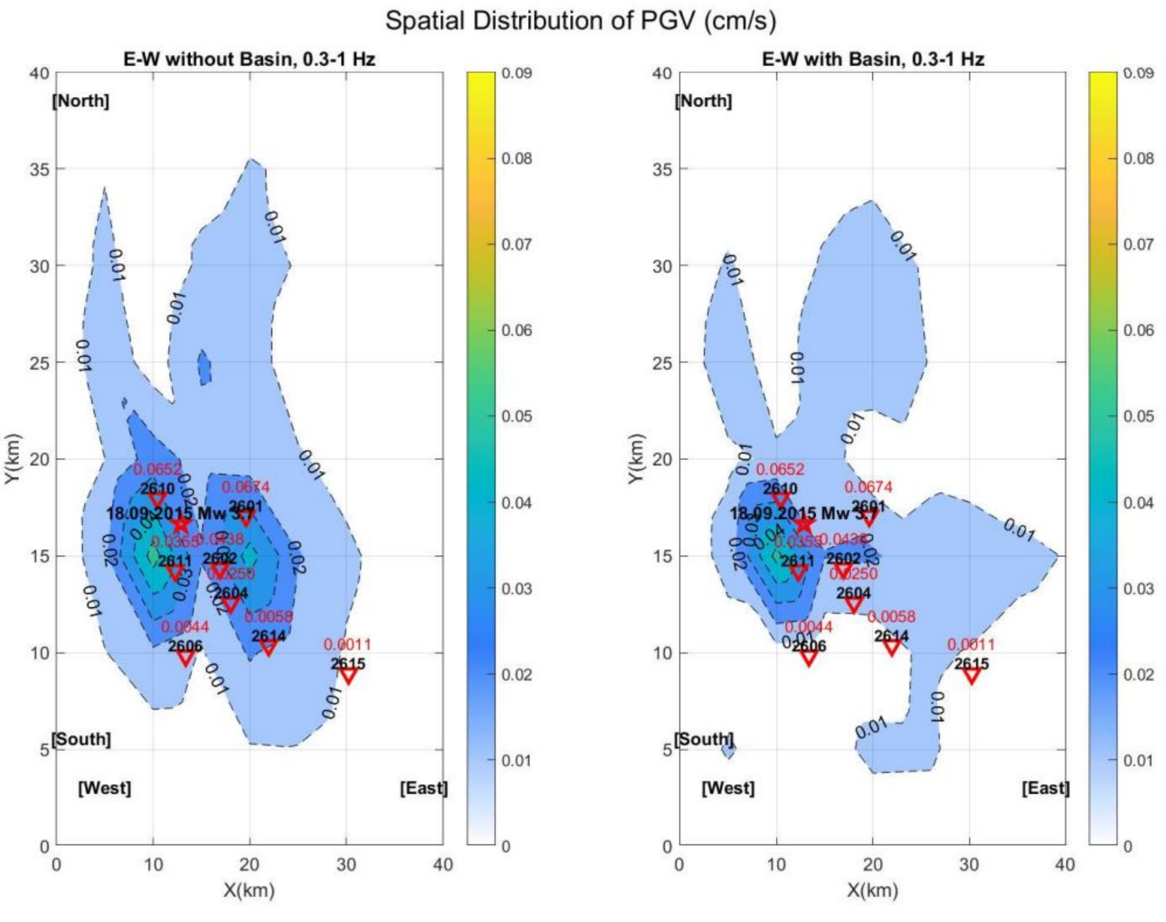

Figure 5.42. Spatial Distribution of PGV (cm/s) for two Models at frequency ranges of 0.3-1 Hz in EW (18.09.2015 Mw 3.7). Left Figure demonstrates the PGV distribution using flat velocity structure, right Figure displays the PGV distribution using velocity structure added basin on top.

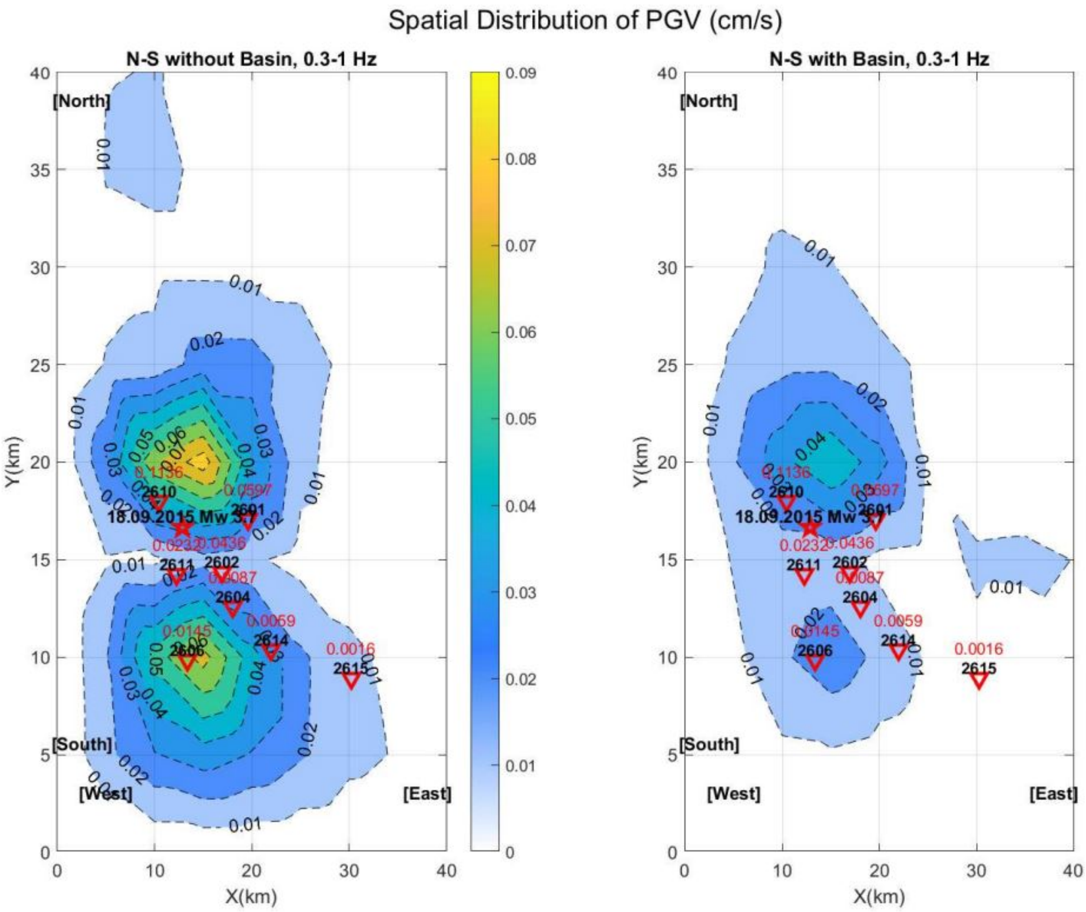

Figure 5.43. Spatial Distribution of PGV (cm/s) for two Models at frequency ranges of 0.3-1 Hz in NS (18.09.2015 Mw 3.7). Left Figure demonstrates the PGV distribution using flat velocity structure, right Figure displays the PGV distribution using velocity structure added basin on top.

The simulation results of both seismic events generally indicate that the amplitude of North-South components is greater than the East-West components in the two models except for the Up-down components due to the directivity effect. The model with a basin has a higher up-down motion component than the model without a basin at frequency ranges of 0.3 and 1 Hz. Notably, the model with a basin has low PGV values compared to another model without a basin. However, the basin's center has a higher PGV value than the flat layered model in the E-W direction. The simulation of seismic motions using the flat layer model describes that the source usually dominates the motion due to the source radiation.

In the 17.01.2015 Mw 4.3 earthquake simulation using a velocity model without the basin, the maximum PGV value is shown in the first and second lines in the model's northernmost. On the other hand, the maximum PGV value appears in the middle of the fourth and fifth lines in the model with the basin. It was systematically observed that the PGV value increased in all lines from south to north. However, max PGV values were generally encountered in each center basin. Another point is that the waveform of velocity time series without basin (1. Model) is very similar to each other in the same line. The basin structure produced the secondary waves after the S arrivals, whereas the flat layer model generated waves with single pulse. These secondary waves with long periods, varying from 2 to 4 s, can be seen in the simulation conducted using the basin model. The depth basin may trigger these secondary waves in the basin's center.

Moreover, the spatial distribution of PGV was drawn in MATLAB by interpolating scattered PGV values over the spatial area for the whole investigated field. When performing this process, the PGV ranges widely in two directions. It is not easy to represent the PGV distribution in the same color scale because of the discrepancy of PGV in two directions . The source effect dominates the characteristics of synthetic motions with the basin model in EW. The PGV of synthetic motion with basin shows a little difference closed the basin for east-west direction. It seems like the basin geometry.

5.3. Blind Simulation for the 1956 Mw 6.5 Eskişehir

The Eskişehir region is prone to destructive earthquakes, as observed in 1956. Considering the seismicity of that field, 20.02.1956 Mw 6.5 is unexpected, the largest event to struck Eskişehir in the instrumental period. The 1956 Mw 6.5 earthquake resulted in damages from moderate to heavy to about 3000 buildings (Öcal, 1959). Except for the damage distribution, the strong ground motion recordings of that seismic event are unavailable. The source features of this earthquake have been the subject of numerous studies (Öcal (1959); Canıtez and Üçer (1967); Seyitoğlu et al. (2015); Tanircan et al. (2020)). However, the geological investigation of the recent study conducted by Seyitoğlu et al. (2015) is consistent with the focal mechanism suggested by Canıtez and Üçer (1967), as aforementioned chapter 3.2. In order to predict the intensity measure of this event, the blind simulation is performed using the finite difference method of Pitarka (1999), utilizing staggered grids with nonuniform spacing in 3D Elastic Media with two velocity structure models, as mentioned previous chapter. Such simulation is called the blind simulation due to the shortage of recordings belonging to the 20.02.1956 Mw 6.5 earthquake.Although the epicenter and the focal mechanism of this event are ambiguous, the blind simulation is a practical way to estimate adverse effects of possible seismic events ,greater than Mw 6.5, on the Eskişehir region.

Tanircan et al. (2020) performed the high-frequency simulation of the 20.02.1956 Mw 6.5 earthquake using a stochastic finite fault method that relied on a dynamic corner frequency. They also demonstrate the spatial distribution of PGA, PGV, and 5% damped elastic Sa at 0.2 s 1 s for engineering bedrock conditions. In the following stage, they modified PGA and SA values with an empirical site amplification model at 48 points with V_{S30} values. In addition, they have compared the simulation results with GMPE. Apart from these, they systematically compiled the source parameters of the 1956 Mw 6.5 earthquake by comparing other researchers' prior studies and findings. This study, conducted by Tanircan et al. (2020), guided this blind simulation, especially construction of source parameters.

The source model of the 1956 Mw 6.5 earthquake is defined as a point source. The source parameter is described in Table 5.6. Another parameter used in the simulation is the substructure model. The velocity models are the same as the structure used in the previous simulation.

Table 5.6. Source parameters of 1956 Mw 6.5 earthquake.

Seismic Event	**Mw**	**Strike (°)**	**Dip (°)**	**Rake (°)**	**Depth (km)**	**Rise Time (s)**	**Mo (dyne*cm)**
20.02.1956	6.5	284	34	-172	14	0.8	4.47*10^25

Moreover, the simulation results in terms of PGV and Sa at distinct periods have been compared with two GMPEs models developed for Turkey, which may not be an effective way to estimate near-field seismic motion as well as basin effects. The predictive models were employed by considering average shear wave velocity up to 30 m of 280m/s and 1300 m/s. The former V_{S30} is regarded as the mean V_{S30} of the basin center. The latter V_{S30} represents the minimum shear wave velocity used in the simulation. The results were superimposed with respect to Rjb distance as below. In addition to these, The spatial distribution of PGV is shown in Figure for two velocity models using virtual station located each 5 km distance. Considering the building stocks of Eskişehir in 1956, the damage distribution of the 1956 Mw 6.5 earthquake may not reflect the effect of the depth basin structure on large-scale buildings. For that reason, the blind simulation plays a crucial role in predicting intensity measures, especially long periods.

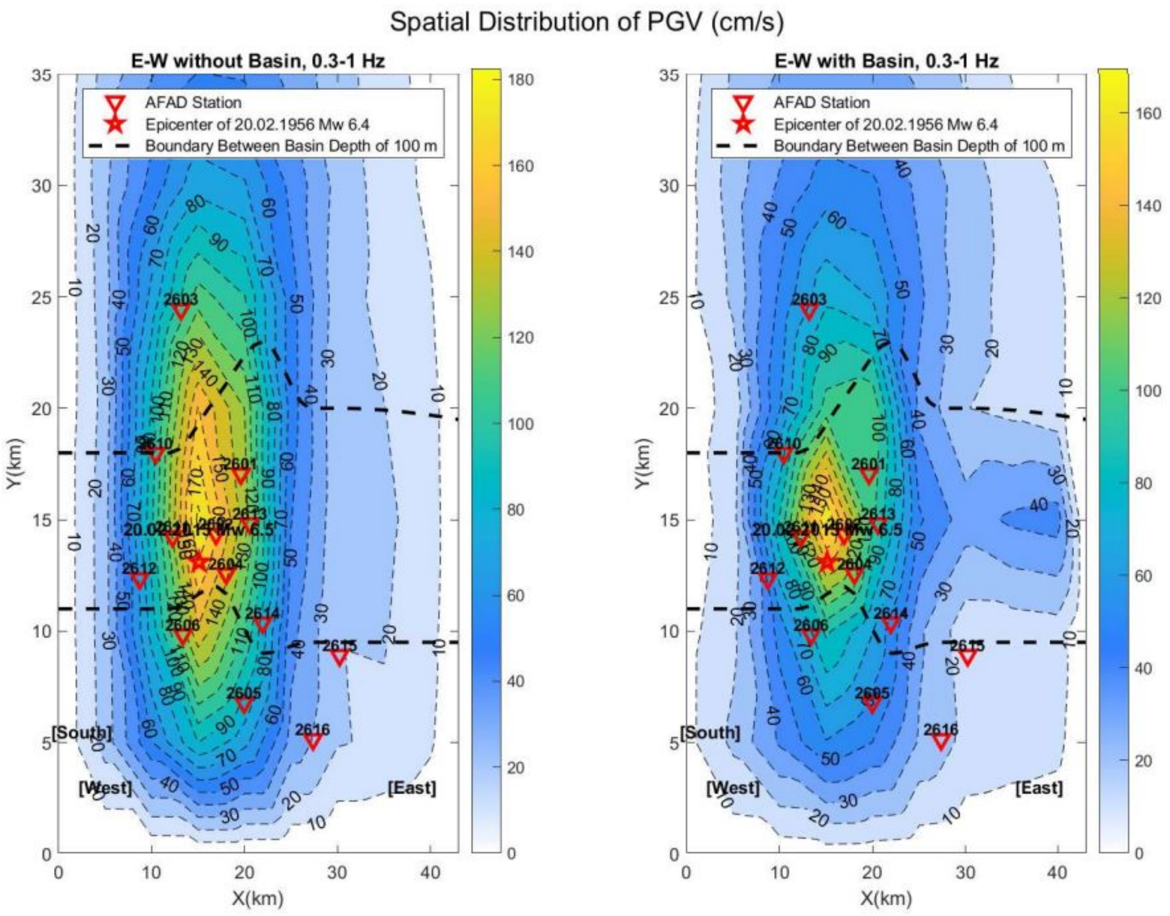

Figure 5.44. Spatial Distribution of PGV (cm/s) for two Models at frequency ranges of 0.3-1 Hz in EW (20.02.1956 Mw 6.5). Left Figure exhibits the PGV distribution using flat velocity structure, right Figure reveals the PGV distribution using velocity structure added basin on top.

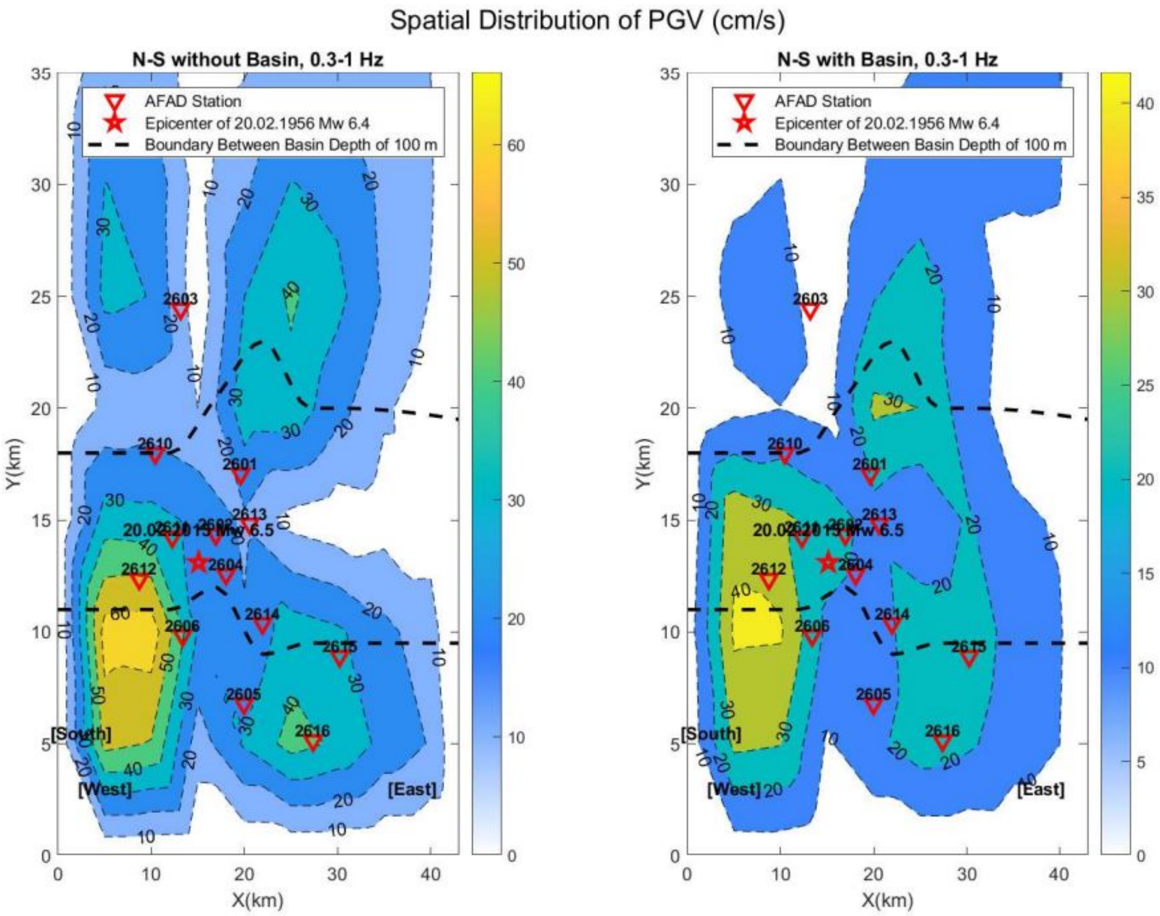

Figure 5.45. Spatial Distribution of PGV (cm/s) for two Models at frequency ranges of 0.3-1 Hz in NS (20.02.1956 Mw 6.5). Left Figure exhibits the PGV distribution using flat velocity structure, right Figure reveals the PGV distribution using velocity structure added basin on top.

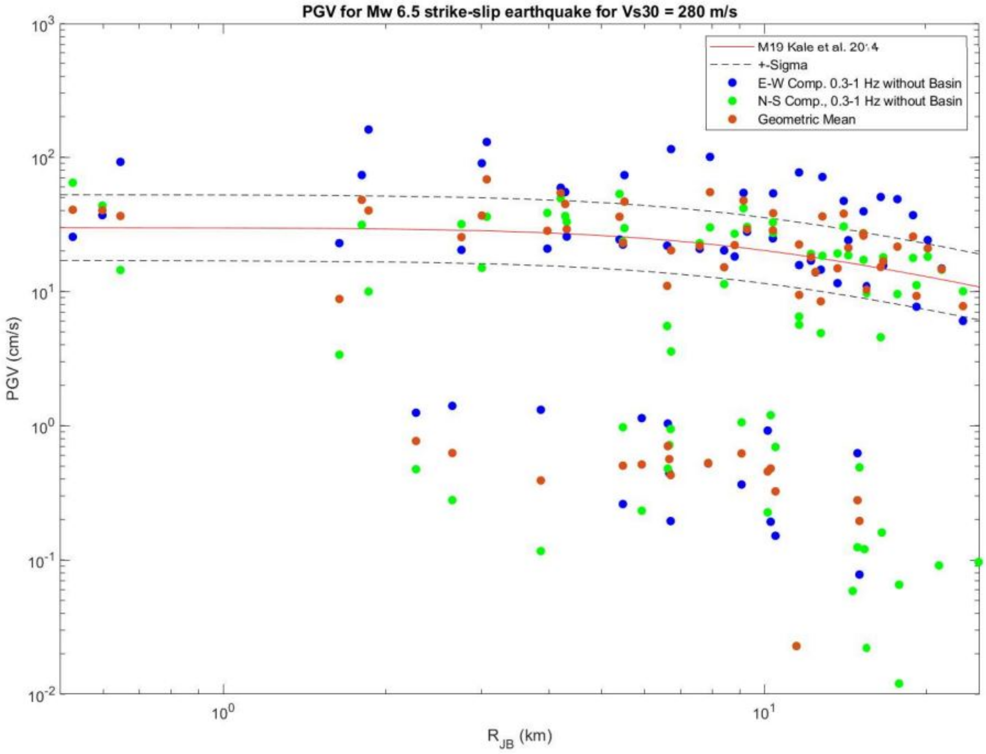

Figure 5.46. Numerical simulation results without basin vs GMPEs by Kale et al. (2015).

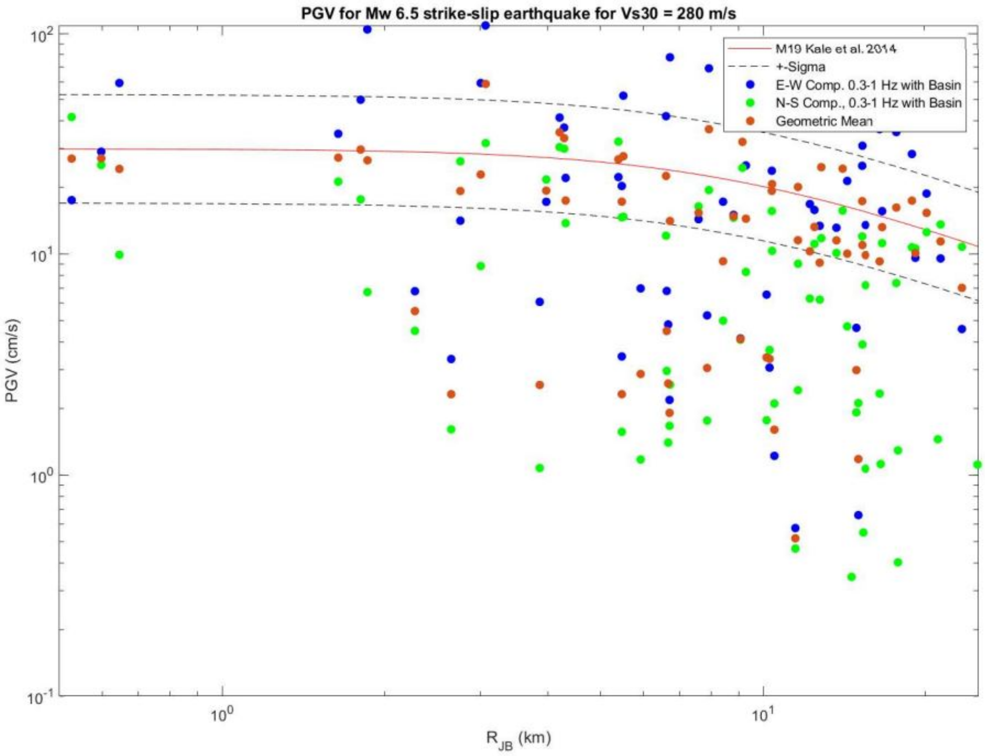

Figure 5.47. Numerical simulation results with basin vs GMPEs by Kale et al. (2015).

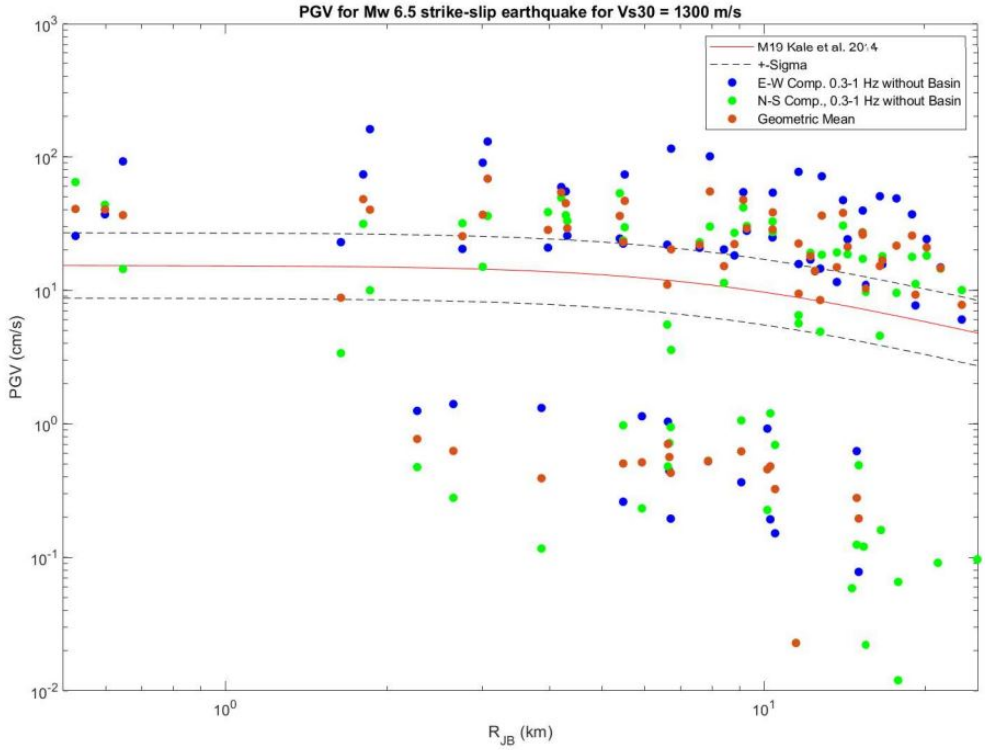

Figure 5.48. Numerical simulation results without basin vs GMPEs by Kale et al. (2015).

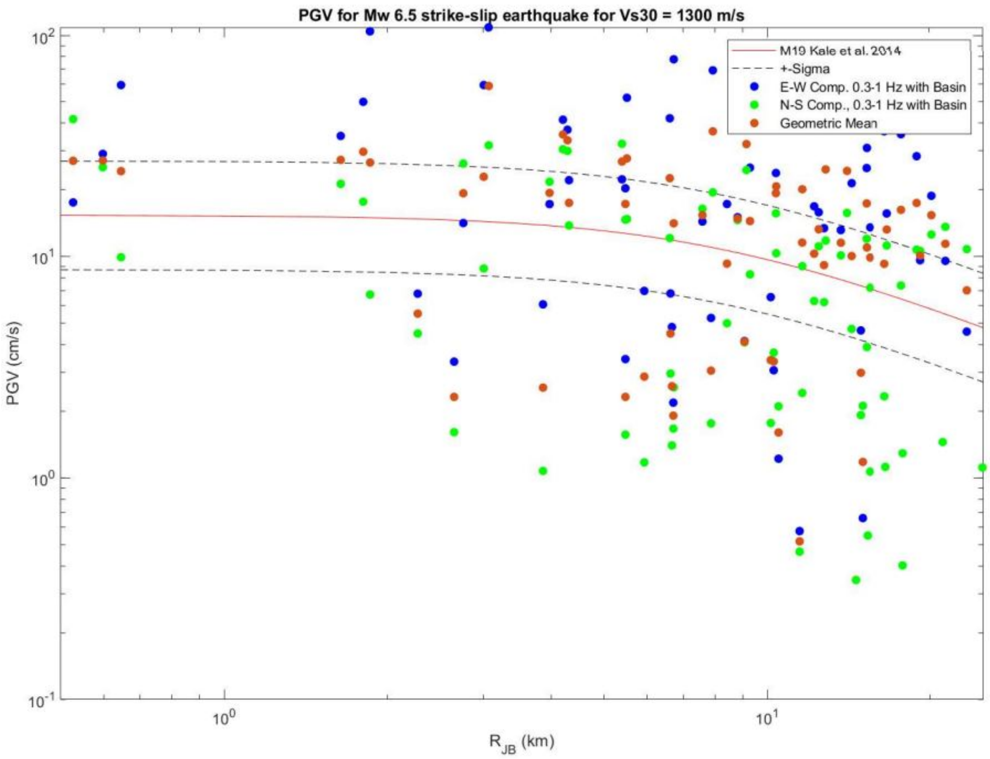

Figure 5.49. Numerical simulation results with basin vs GMPEs by Kale et al. (2015).

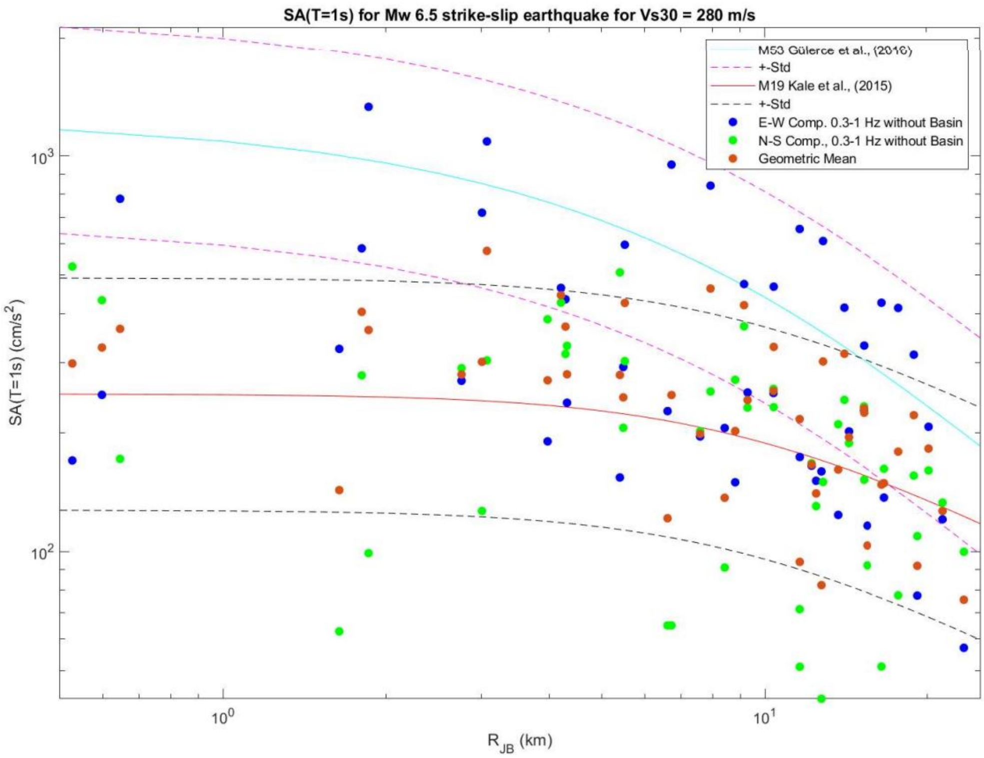

Figure 5.50. Numerical simulation results without basin vs GMPEs by Kale et al. (2015) and Gülerce et al. (2016).

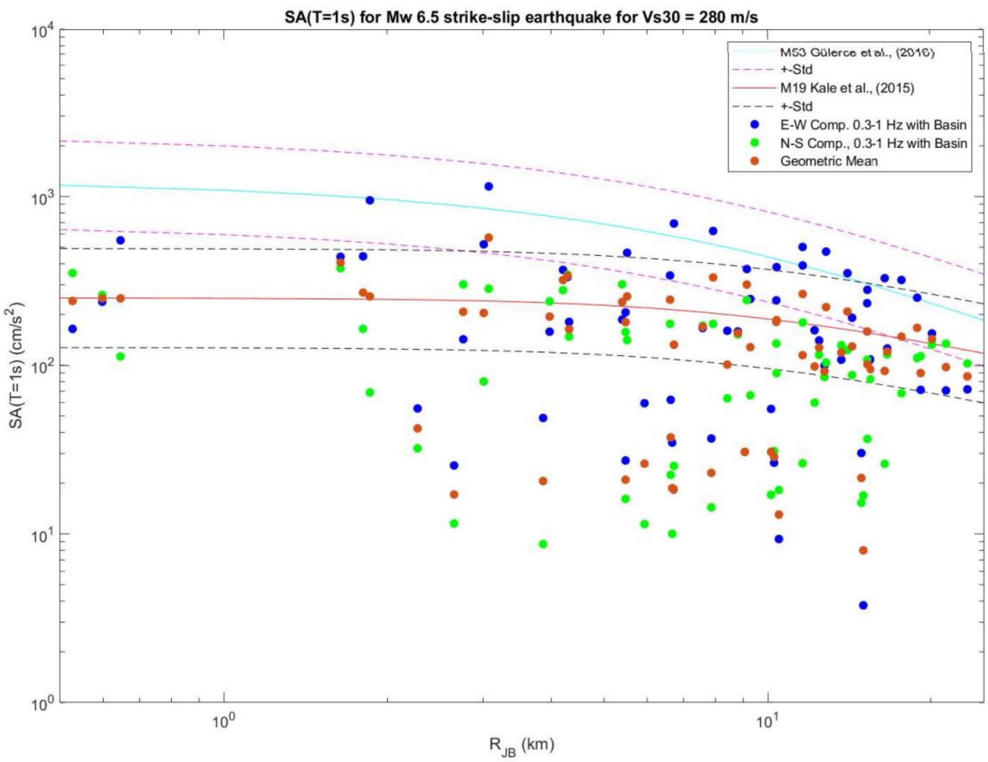

Figure 5.51. Numerical simulation results with basin vs GMPEs by Kale et al. (2015) and Gülerce et al. (2016).

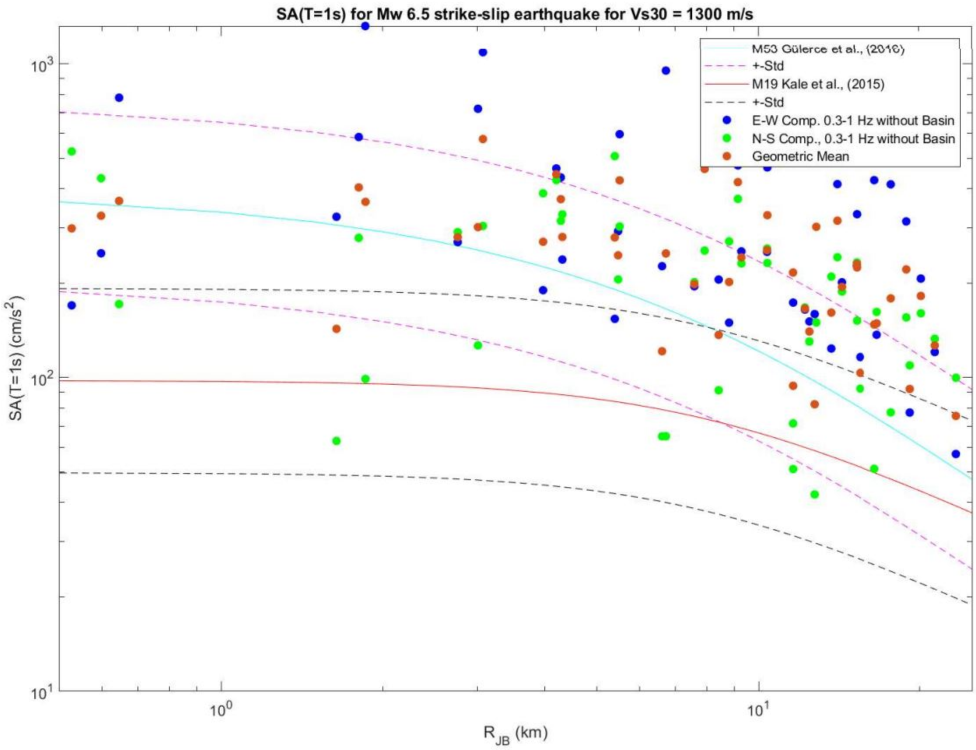

Figure 5.52. Numerical simulation results without basin vs GMPEs by Kale et al. (2015) and Gülerce et al. (2016).

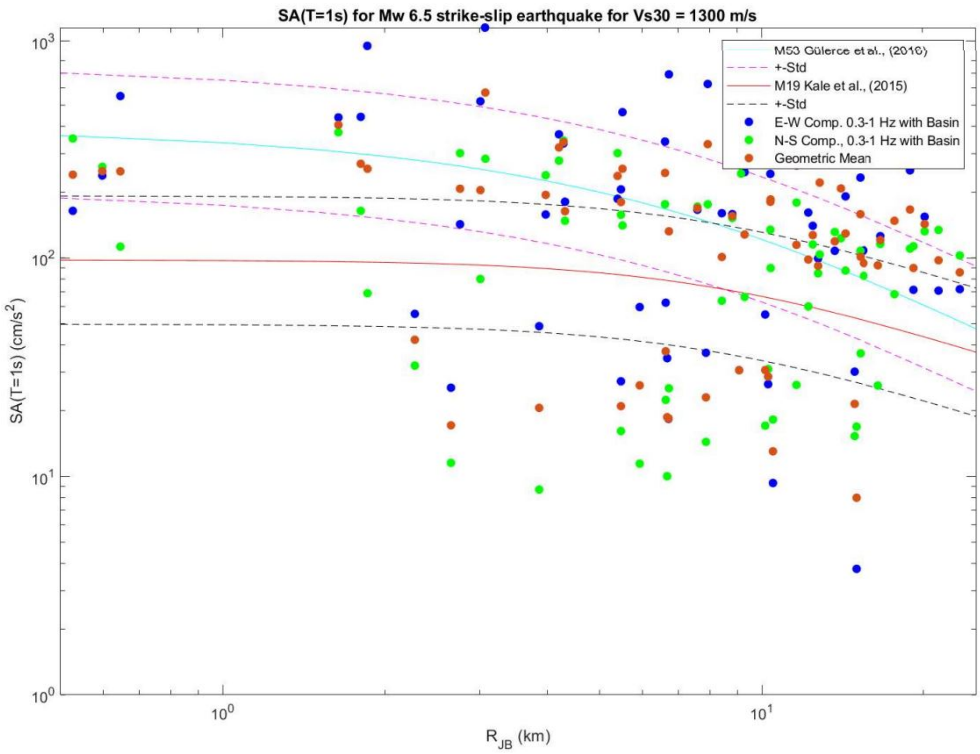

Figure 5.53. Numerical simulation results with basin vs GMPEs by Kale et al. (2015) and Gülerce et al. (2016).

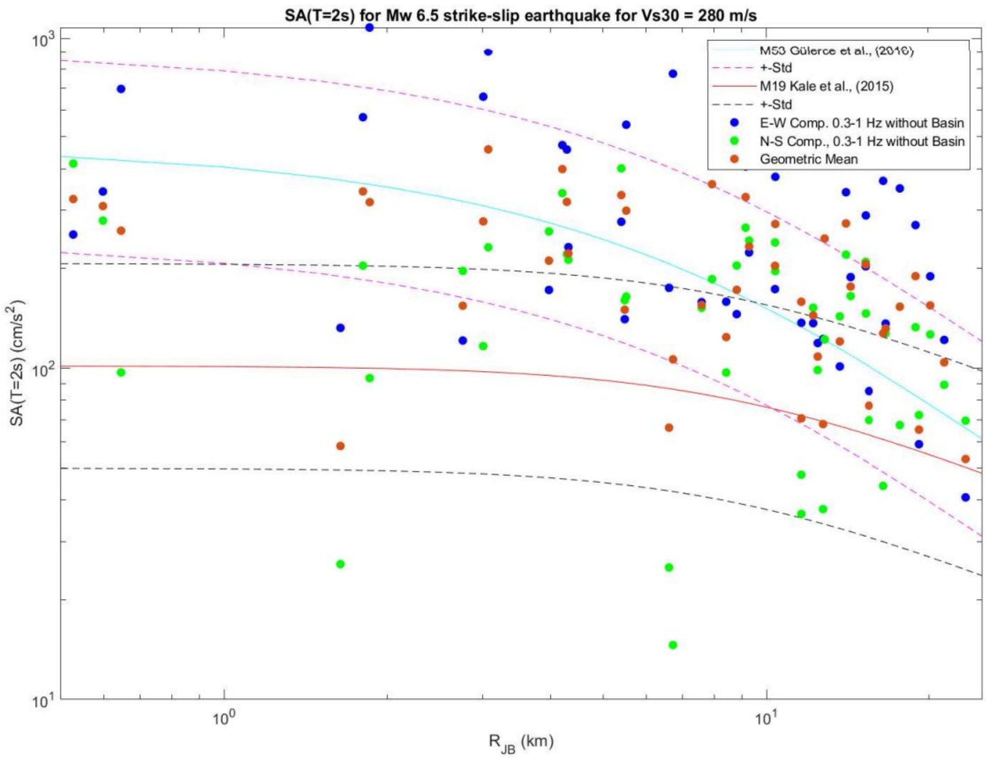

Figure 5.54. Numerical simulation results without basin vs GMPEs by Kale et al. (2015) and Gülerce et al. (2016).

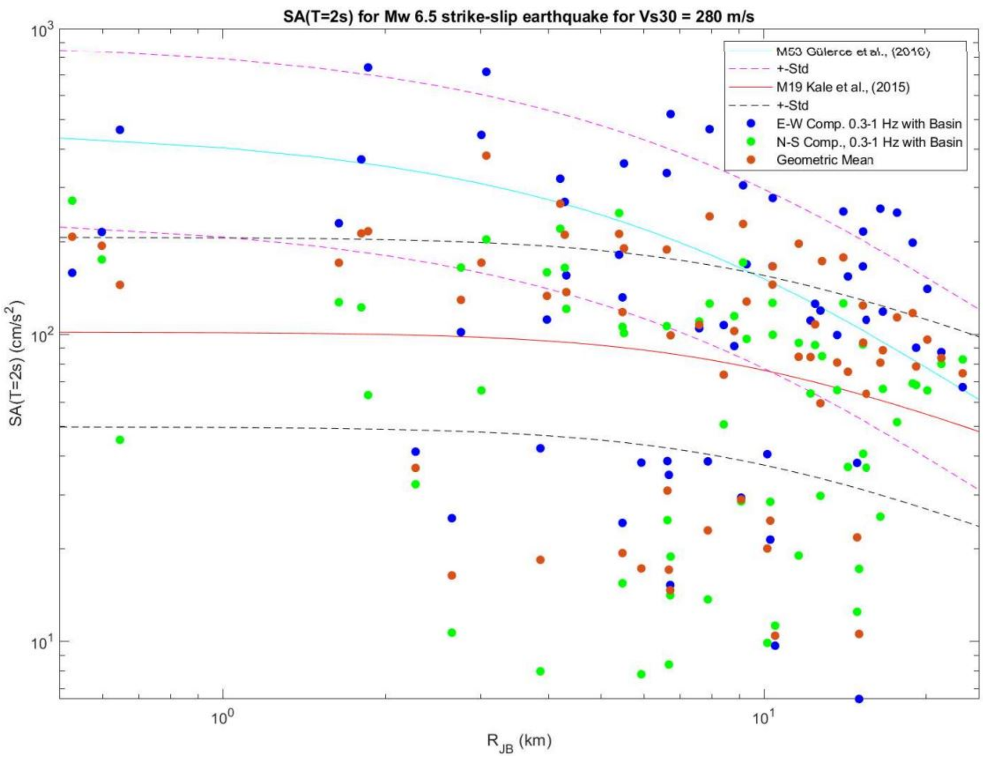

Figure 5.55. Numerical simulation results with basin vs GMPEs by Kale et al. (2015) and Gülerce et al. (2016).

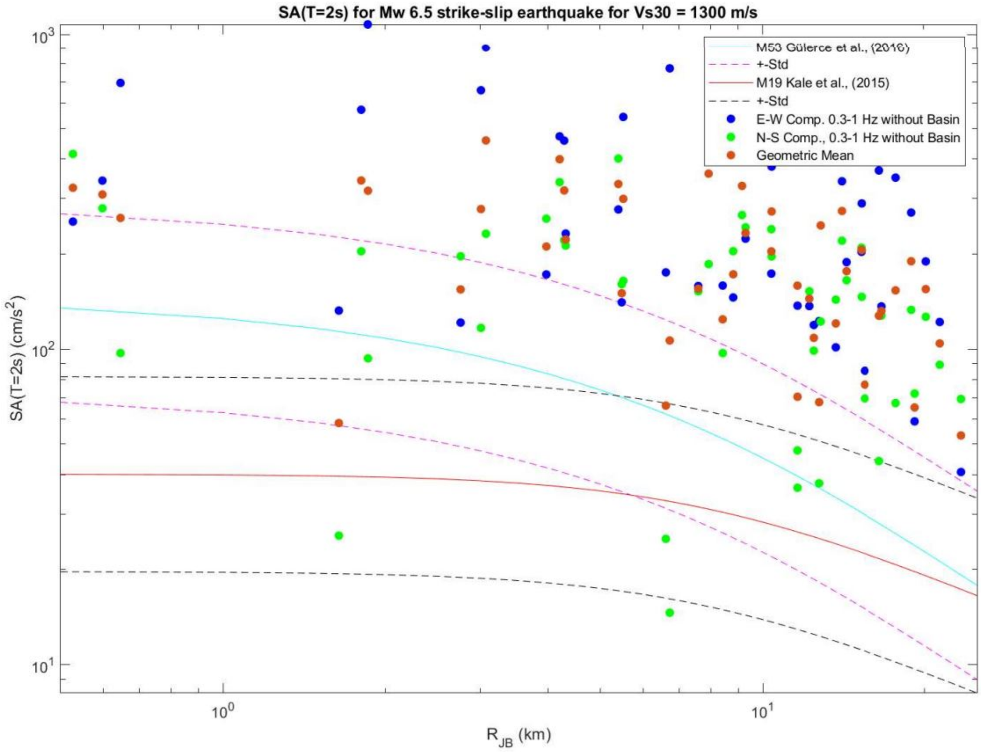

Figure 5.56. Numerical simulation results without basin vs GMPEs by Kale et al. (2015) and Gülerce et al. (2016).

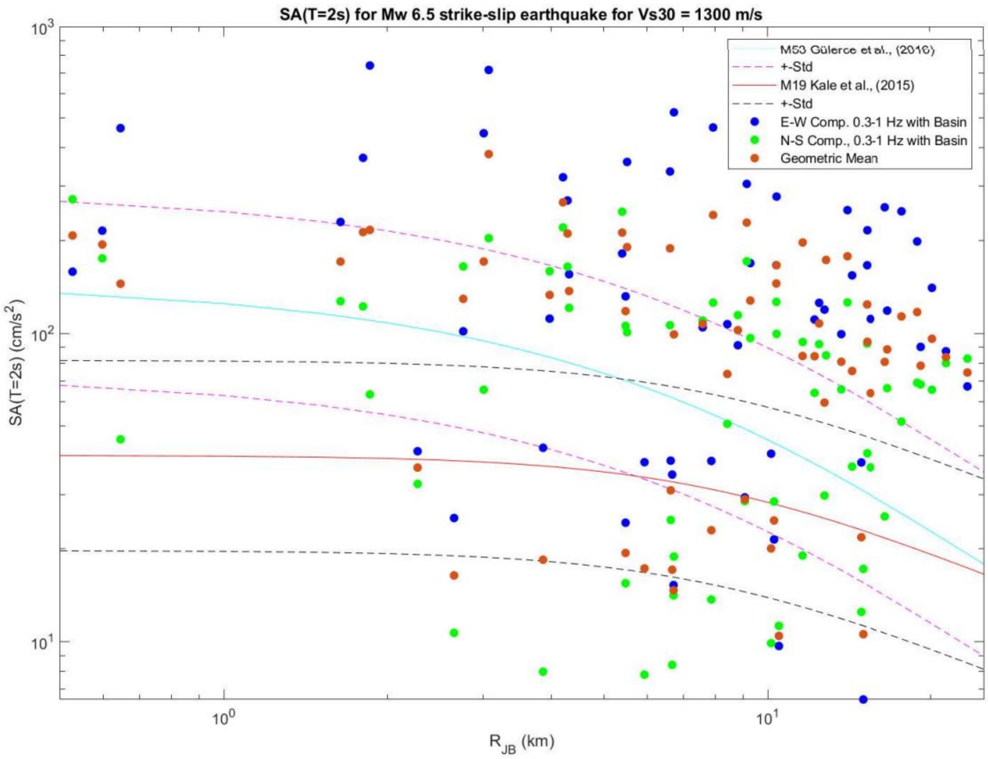

Figure 5.57. Numerical simulation results with basin vs GMPEs by Kale et al. (2015) and Gülerce et al. (2016).

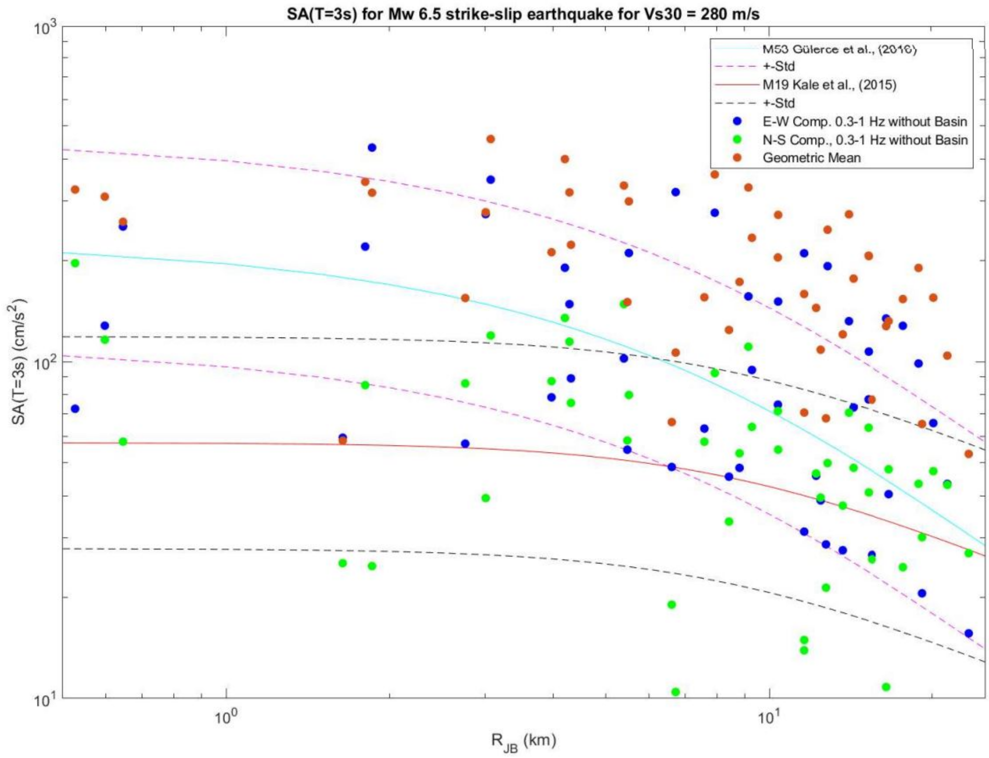

Figure 5.58. Numerical simulation results without basin vs GMPEs by Kale et al. (2015) and Gülerce et al. (2016).

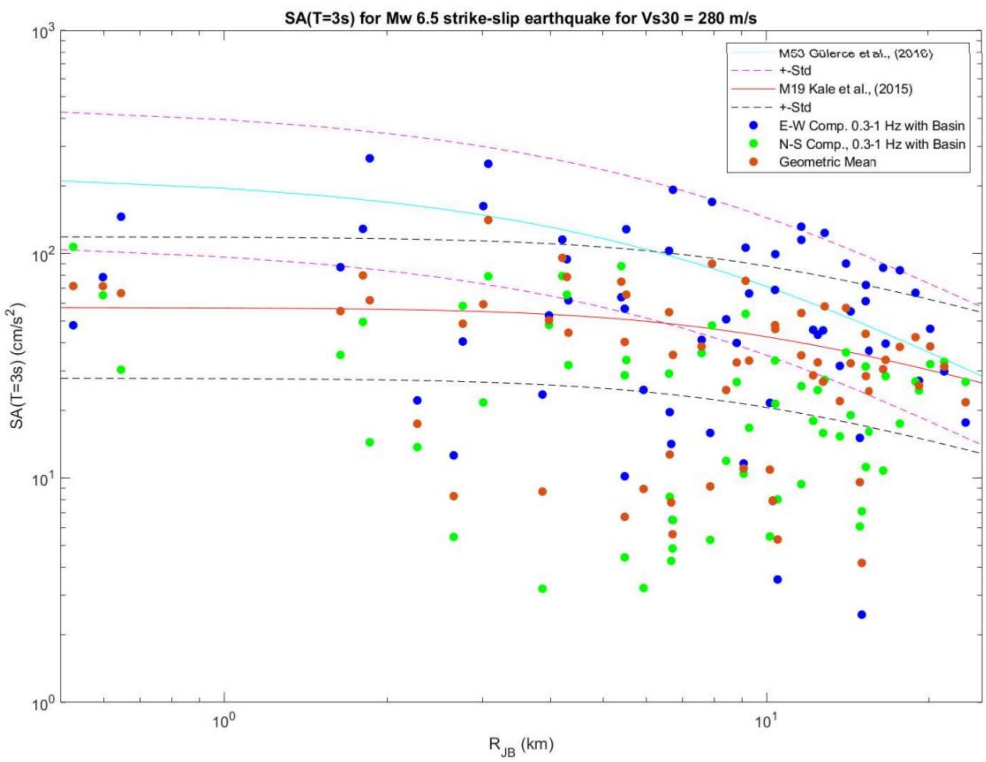

Figure 5.59. Numerical simulation results with basin vs GMPEs by Kale et al. (2015) and Gülerce et al. (2016).

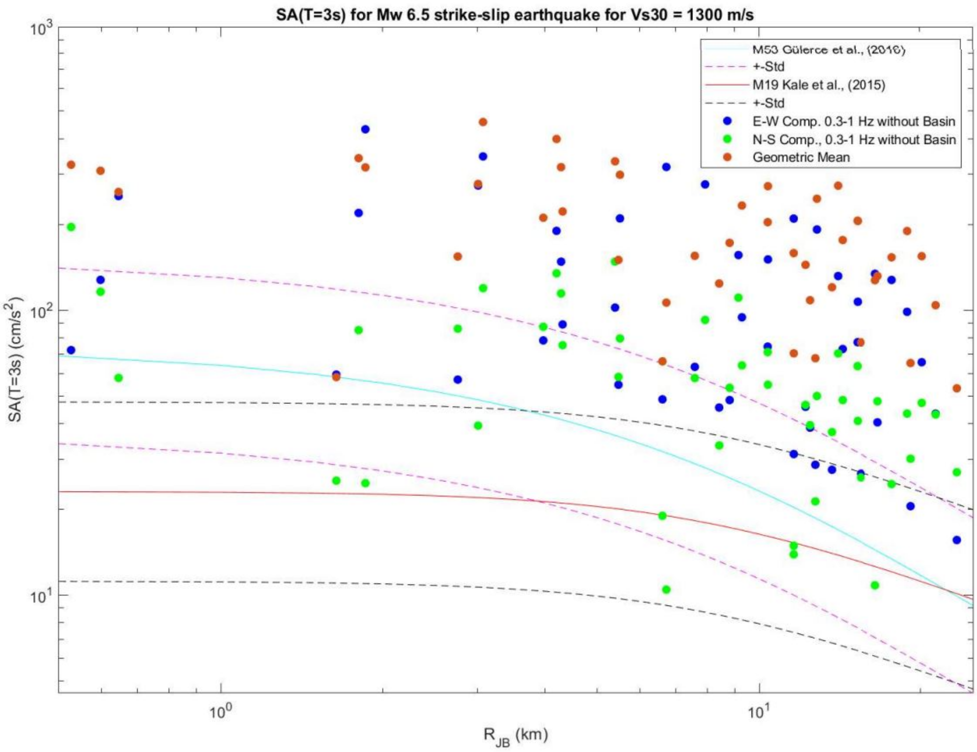

Figure 5.60. Numerical simulation results without basin vs GMPEs by Kale et al. (2015) and Gülerce et al. (2016).

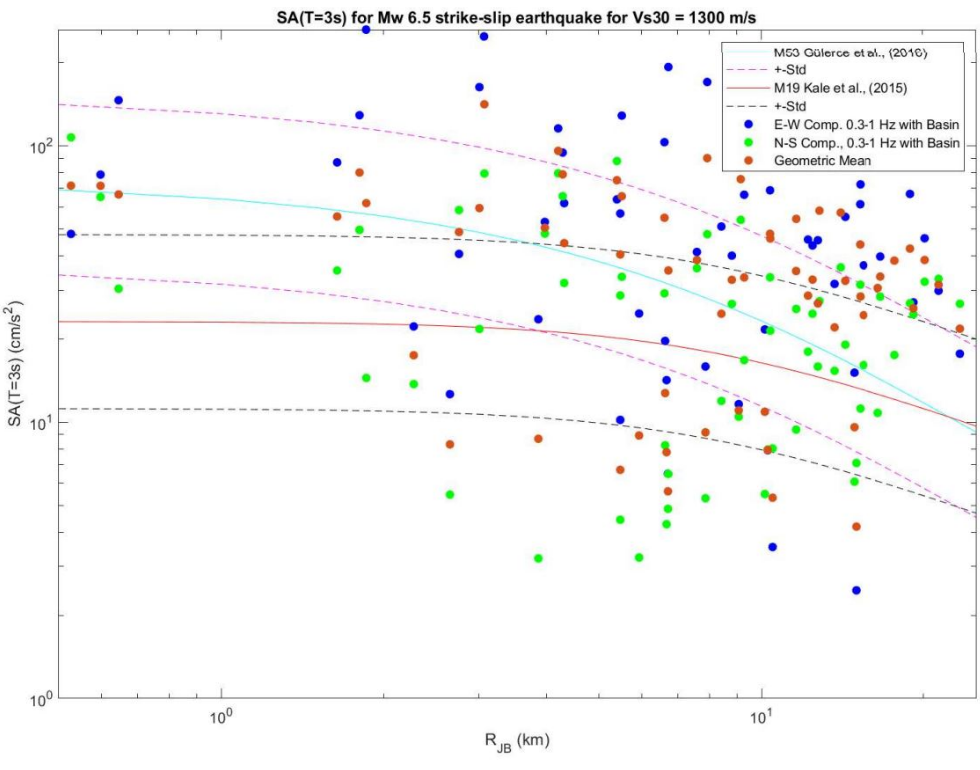

Figure 5.61. Numerical simulation results with basin vs GMPEs by Kale et al. (2015) and Gülerce et al. (2016).

The generated seismic movement of the 1956 Mw 6.5 event using the method of Pitarka (1999) has been compared with both GMPEs models suggested by Kale et al. (2015) and Gülerce et al. (2016). For the predictive models, two Vs 30 were assumed to represent the average shear wave velocity of the basin and shear wave velocity utilized in the simulation, 280 m/s, and 1300 m/s respectively. The result indicates that the PGV value acquired from the quantitative simulation is far beyond the estimation of the attenuation relation using V_{S30} of 1300 m/s. PGV utilizing the finite difference method is consistent within a value of plus or minus standard deviation with the median of predictive models with V_{S30} 280 m/s.

In general, the inconsistency between GMPEs models and simulation results increases with the rising of the fundamental period and V_{S30}. The maximum contradiction is shown in V_{S30} of 1300 m/s and the predominant period of 3s.

The predictive model proposed by Gülerce et al. (2016) demonstrates well agreement with simulation results, V_{S30} of 280 m/s and T=1s. This attenuation relationship estimates Sa at different periods above the simulation results, using V_{S30} equal to 280 m/s.

6. CONCLUSION AND DISCUSSION

This study focuses on long period ground motion modelling in Eskişehir basin with a 3-D substructure model, which was constructed using a horizontally layered velocity structure and a horizontally layered velocity structure with a basin geometry added on top. As an initial step to investigate the characteristic features of the strong ground motion in the basin, recordings of the 2011 Simav earthquake (Mw 5.9) was studied. Particle motions at five stations were drawn to seek for availability of the retrograde motions. Significant duration and envelop delay times were computed for each recording. Recorded PGA, long period SAs and Sd were compared with GMPEs. It has been observed that basin-center stations have longer duration compared to those of farther stations. As expected, basin stations have larger delay times. In other words, lengthening of the ground motion mainly occurs at low frequencies due to very low attenuation. However, no systematic changes between the group delay of basin-edge and basin-center stations were observed with limited data. As for the comparison of the predictive model, GMPEs provided by Kale et al. (2015) and Gülerce et al. (2016) have underestimated spectral accelerations at long period at basin stations. The GMPEs were insufficient in predicting the near-ground motions, basin effects at long periods, and wave propagation. When the waves propagate in the basin, it is trapped, and the reverberation occurs.

The numerical simulation without basin using the finite difference method at low frequency shows good matching with the 17.01.2015 Mw 4.3 earthquake in EW direction in frequency range between 0.3 and 1 Hz. The velocity model added 3D basin geometry on top has improved the wave forms in NS. However, there were challenges in producing time series to be in agreement with recorded seismograms in the NS direction. One of the underlying reasons for incompatibility in the NS direction may arise from the narrow width of the basin model in NS. This span, varying from 7 km to 14 km corresponding to depth of 100 m, may not allow generating the waves with 5.2 km wavelength. Outcomes indicate that the velocity structure is more complex than the model utilized in the simulation. Moreover, the spatial variability might be beyond predicted value. The discrepancy between synthetics and real data may stem from the velocity contrast and representation of the basin with a single layer. Further field investigations might be helpful to improve the velocity structure model.

Finally, the blind simulation of the 1956 Mw 6.5 earthquake was performed and synthetics are compared with the two predictive models developed/modified for Turkey. PGV in long period range is as high as 150 cm/s in EW direction in the basin. In contrary to simulation without basin model, simulation with basin structures produces higher PGV values in the east. Majority of the geometric mean of simulated PGVs predictions are in line mean + 1 standard deviation of predictions with V_{S30}=1300 m/s. Simulated spectral accelerations at 1s spectral period are comparable with mean and mean + 1 standard deviation of prediction models by Gülerce et al. (2016).In general, the deviation from estimated ground intensity measure increases with the high V_{S30} and long periods for two GMMs. The simulation outcomes using basin model are usually consistent with GMMs with V_{S30} 280 m/s.

As for the future works, we will attempt to improve the compatibility of synthetic waves with observed data by utilizing abundant experimental velocity structure models, which should be consistent with site surveys in terms of stratigraphic and geometrical conditions. Moreover, we will change the point source model with the finite fault model. Thus, the source effect is taken into account more realistic.

REFERENCES

Abrahamson, N. A. and D. Sykora, 1993, "Variations of ground motions across individual sites", paper presented at the *the DOE Natural Phenomena Hazards Mitigation Conference*, pp.192-198.

Anderson, J., P. Bodin, J. Brune, J. Prince, S. Singh, R. Quaas and M. Onate, 1986, "Strong ground motion from the Michoacan, Mexico, earthquake", *American Association for the Advancement of Science*, Vol. 233, No. 4768, pp. 1043-1049.

Arias, Arturo, 1970, "Measure of Earthquake Intensity", *Massachusetts Inst. of Tech., Cambridge. Univ. of Chile, Santiago de Chile* (Tech. Rep.).

Barka, A., and R. Reilinger, 1997, "Active tectonics of the Eastern Mediterranean region: deduced from GPS, neotectonic and seismicity data".

Boore, D. M., 2003, "Phase derivatives and simulation of strong ground motions", *Bulletin of the Seismological Society of America*, Vol. 93, No.3, pp. 1132-1143.

Bozorgnia, Y. and V. V. Bertero, *Earthquake engineering: from engineering seismology to performance-based engineering*, CRC press, 2004.

Canıtez, N and B. Üçer, 1967, "A catalogue of focal mechanism diagrams for Turkey and adjoining areas", *Istanbul Technical University Arz. Fizigi Enstitusu*, Vol. 25.

Di Michele, F., J. May, D. Pera, V. Kastelic, M. Carafa, C. Smerzini and P. Marcati, 2022, "Spectral element numerical simulation of the 2009 L'Aquila earthquake on a detailed reconstructed domain", *Oxford University Press*, Vol. 230, No.1, pp. 29-49.

Dobry, R., I. M. Idriss and E. Ng, 1978, "Duration characteristics of horizontal components of strong-motion earthquake records", *Bulletin of the Seismological Society of America*, Vol. 68, No. 5, pp. 1487-1520.

Emre, Ö., T. Y. Duman, S. Özalp, F. Şaroğlu, Ş. Olgun, H. Elmacı and T. Çan, 2018, "Active fault database of Turkey", *Bulletin of Earthquake Engineering*, Vol. 16, No. 8, pp. 3229-3275.

Goto, H., and S. Sawada, 2004, "Numerical simulation of strong ground motion on Adapazari basin during the 1999 Kocaeli, Turkey, earthquake", paper presented at the *3th World conference on earthquake engineering* Paper No.720, Vancouver, BC, Canada, .

Graves, R. W., 1996, "Simulating seismic wave propagation in 3D elastic media using staggered-grid finite differences", *Bulletin of the seismological society of America*, Vol. 86, No. 4, pp. 1091-1106.

Gülerce, Z., B. Akbaş, A. A. Özacar, E. Sopacı, F. M. Önder, B. Uzel and B. Unutmaz, 2022, "Predictive performance of current ground motion models for recorded strong motions in 2020 Samos Earthquake", *Soil Dynamics and Earthquake Engineering*, Vol. 152, pp. 107053.

Gülerce, Z., B. Kargoığlu and N. A. Abrahamson, 2016, "Turkey-adjusted NGA-W1 horizontal ground motion prediction models", *Earthquake Spectra*, Vol. 32, No. 1, pp. 75-100.

Hartzell, S., S. Harmsen, R. A. Williams, D. Carver, A. Frankel, G. Choy and C. M. Wentworth, 2006, "Modeling and validation of a 3D velocity structure for the Santa Clara Valley, California, for seismic-wave simulations", *Bulletin of the Seismological Society of America*, Vol. 96, No. 5, pp. 1851-1881.

Hasal, M. E., R. Iyisan and H. Yamanaka, 2018, “Basin edge effect on seismic ground response: a parametric study for Duzce basin case, Turkey”, *Arabian Journal for Science and Engineering*, Vol. 43, No. 4, pp. 2069-2081.

Hatayama, K., K. Matsunami, T. Iwata and K. Irikura, 1995, “Basin-induced Love waves in the eastern part of the Osaka basin”, *Journal of Physics of the Earth*, Vol. 43, No. 2, pp. 131-155.

Igel, H., *Computational seismology: a practical introduction*, Oxford University Press, 2017.

Iyisan, R. and H. Khanbabazadeh, 2013, “A numerical study on the basin edge effect on soil amplification”, *Bulletin of Earthquake Engineering*, Vol. 11, No. 5, pp. 1305-1323.

Joyner, W. B. and D. M. Boore, 1981, “Peak horizontal acceleration and velocity from strong-motion records including records from the 1979 Imperial Valley, California, earthquake”, *Bulletin of the seismological Society of America*, Vol. 71, No. 6, pp. 2011-2038.

Kale, Ö., S. Akkar, A. Ansari and H. Hamzehloo, 2015, “A ground-motion predictive model for Iran and Turkey for horizontal PGA, PGV, and 5% damped response spectrum: Investigation of possible regional effects”, *Bulletin of the Seismological Society of America*, Vol. 105, No. 2A, pp. 963-980.

Koçyiğit, A. and A. Özacar, 2003, “Extensional neotectonic regime through the NE edge of the outer Isparta Angle, SW Turkey: new field and seismic data”, *Turkish Journal of Earth Sciences*, Vol. 12, No. 1, pp. 67-90.

Koketsu, K., K. Hatayama, T. Furumura, Y. Ikegami and S. Akiyama, 2005, “Damaging long-period ground motions from the 2003 Mw 8.3 Tokachi-oki, Japan earthquake”, *Seismological Research Letters*, Vol. 76, No. 1, pp. 67-73.

Koketsu, K., and H. Miyake, 2008, “A seismological overview of long-period ground motion”, *Journal of Seismology*, Vol. 12, No. 2, pp. 133-143.

Kudo, K., and M. Sakaue, 1984, “Oil-sloshing in the huge tanks at Niigata due to the Nihonkai-Chubu earthquake of 1983”, *Bulletin of the Earthquake Research Institute-University of Tokyo*, Vol. 59, pp. 361-382.

Makra, K., E. Rovithis, E. Riga, D. Raptakis and K. Pitilakis, 2021, “Amplification features and observed damages in İzmir (Turkey) due to 2020 Samos (Aegean Sea) earthquake: identifying basin effects and design requirements”, *Bulletin of Earthquake Engineering*, Vol. 19, No. 12, pp. 4773-4804.

MATLAB, 2021, “A9.10.0.1851785 (R2021a)”, The MathWorks Inc, Natick, Massachusetts.

Maufroy, E., E. Chaljub, F. Hollender, J. Kristek, P. Moczo, P. Klin and P. Y. Bard, 2015, “Earthquake ground motion in the Mygdonian basin, Greece: The E2VP verification and validation of 3D numerical simulation up to 4 Hz”, *Bulletin of the Seismological Society of America*, Vol. 105, No. 3, pp. 1398-1418.

McKenzie, D., 1972, “Active tectonics of the Mediterranean region”, *Geophysical Journal International*, Vol. 30, No. 2, pp. 109-185.

Meza-Fajardo, K. C., H. Aochi and A. S. Papageorgiou, 2021, “Comparative analysis of Rayleigh and Love waves detected propagating in the Nobi and Kanto basins during the 2004-, 2007-Chuetsu and 2011 Tohoku earthquakes”, *Soil Dynamics and Earthquake Engineering*, Vol. 143, pp. 106606.

Mindevalli, O. Y. and B. J. Mitchell, 1972, “Crustal structure and possible anisotropy in Turkey from seismic surface wave dispersion”, *Geophysical Journal International*, Vol. 98, No. 1, pp. 93-106.

Moczo, P., J. Kristek and M. Gális, *The finite-difference modelling of earthquake motions: Waves and ruptures*, Cambridge University Press, 2014.

Nakamura, Y., 1989, "A method for dynamic characteristics estimation of subsurface using microtremor on the ground surface", *Railway Technical Research Institute, Quarterly Reports*, Vol. 30, No. 1.

Ocakoğlu, F., 2007, "A re-evaluation of the Eskişehir Fault Zone as a recent extensional structure in NW Turkey", *Journal of Asian Earth Sciences*, Vol. 31, No. 2, pp. 91-103.

Öcal, N., 1959, "Eskisehir Depremi Makro ve Mikrosismik Gozlemleri", *Seismology Institute Publication, Istanbul Technical University, Istanbul.*

Özalaybey, S., E. Zor, S. Ergintav and M. C. Tapırdamaz, 2011, "Investigation of 3-D basin structures in the Izmit Bay area (Turkey) by single-station microtremor and gravimetric methods", *Geophysical Journal International*, Vol. 186, No. 2, pp. 883-894.

Özel, O., E. Yalcinkaya, G. Birgoren, M. Tün, E. Pekkan, O. Kaplan, 2020, "Kabuk Depremleri Nedeniyle Oluşan Kuvvetli Yer Hareketinin Tahmini için Jeolojik Yapıların Modellemesi Ortak Araştırması", *TUBITAK 1001 Project, Projct Code: 116Y524.*

Özmen, B., 2000, "İzmit Körfezi Depremi'nin Hasar Durumu:(Rakamsal Verilerle)", *Türkiye Deprem Vakfı.*

Pitarka, A., 1999, "3D elastic finite-difference modeling of seismic motion using staggered grids with nonuniform spacing", *Bulletin of the Seismological Society of America*, Vol. 89, No. 1, pp. 54-68.

Pitarka, A., A. Al-Amri, M. E. Pasyanos, A. J. Rodgers and R. J. Mellors, 2015, "Long-Period Ground Motion in the Arabian Gulf from Earthquakes in the Zagros Mountains Thrust Belt", *Pure and Applied Geophysics*, Vol. 172, No. 10, pp. 2517-2532.

Pitarka, A., R. Graves and P. Somerville, 2004, "Validation of a 3D velocity model of the Puget Sound region based on modeling ground motion from the 28 February 2001 Nisqually earthquake", *Pure and Applied Geophysics*, Vol. 94, No. 5, pp. 1670-1689.

Sandıkkaya, M. A. and S. Akkar, 2017, "Cumulative absolute velocity, Arias intensity and significant duration predictive models from a pan-European strong-motion dataset", *Bulletin of Earthquake Engineering*, Vol. 15, No. 5, pp. 1881-1898.

Şaroğlu, F., Ö. Emre and A. Boray, 1987, "Türkiye'nin diri fayları ve depremsellikleri", *MTA. Rap*, Vol. 394.

Sawada, S., K. Irikura, K. Kudo, H. Okada and T. Sasatani, 1998, "Phase characteristics on site amplification of layered ground with irregular interface", *Bulletin of Earthquake Engineering*, pp. 1009-1013.

Seyitoğlu, G., G. B. Ecevitoğlu, B. Kaypak, Y. Güney, M. Tün, K. Esat and G. G. Uyar AlDaş, 2015, "Determining the main strand of the Eskisehir strike-slip fault zone using subsidiary structures and seismicity: a hypothesis tested by seismic reflection studies", *Scientific Technical Research Council Turkey-Tubitak*.

Sucuoğlu, H., S. Akkar, *Basic Earthquake Engineering*, Springer, 2014.

Tanircan, G., 2012, "İstanbul için 3 boyutlu hız modeli ile yer hareketi simülasyonu", *Gazi Üniversitesi Mühendislik Mimarlık Fakültesi Dergisi*, Vol. 27, No. 1.

Tanircan, G., H. Miyake, O. Özel, H. Yamanaka, K. Chimoto, S. Tsuno, N. Takai and O. Kaplan, 2020, "Strong Ground Motion Simulation of the 1956 (Mw 6.5) Eskisehir, Turkey Earthquake", paper presented at the *Proceedings of the 17th World Conference on Earthquake Engineering*, Sendai.

Telford, W. M., W. Telford, L. Geldart and R. E. Sheriff, *Applied geophysics*, Cambridge university press, 1990.

Trifunac, M. D. and A. G. Brady, 1975, "A study on the duration of strong earthquake ground motion", *Bulletin of the Seismological Society of America*, Vol. 65, No. 3, pp. 581-626.

Tün, M., E. Pekkan, O. Özel and Y. Guney, 2016, "An investigation into the bedrock depth in the Eskisehir Quaternary Basin (Turkey) using the microtremor method", *Geophysical Journal International*, Vol. 207, No. 1, pp. 589-607.

Yamanaka, H., Ö. T. Özmen, K. Chimoto, M. A. Alkan, M. Tün, E. Pekkan, O. Özel, D. Polat and M. Nurlu, 2018, "Exploration of S-wave velocity profiles at strong motion stations in Eskisehir, Turkey, using microtremor phase velocity and S-wave amplification", *Journal of Seismology*, Vol. 22, No. 5, pp. 1127-1137.